

# **Hyperbranched Polymers as Virus Binding Inhibitors**

Inaugural-Dissertation

to obtain the academic degree

Doctor rerum naturalium (Dr. rer. nat.)

submitted to the Department of Biology, Chemistry, Pharmacy  
of Freie Universität Berlin

by

**Matthias Wallert**

née Müller

Berlin, November 2020



The following project was carried out within the research groups of Dr. Stephan Block and Prof. Dr. Rainer Haag from **January 2017** until **November 2020** at the Institute of Chemistry and Biochemistry of the Freie Universität Berlin.

1. Reviewer: Dr. Stephan Block, Freie Universität Berlin

2. Reviewer: Prof. Dr. Rainer Haag, Freie Universität Berlin

Day of defense: 7<sup>th</sup> December 2020

## Acknowledgements

First of all, I would like to thank Dr. Stephan Block for giving me the opportunity to be the first doctoral student in his just founded research group. I really liked to see and be part of the development of this interdisciplinary group, which is fruitful growing. Thanks for the financial and scientific support over the last years. Moreover, Prof. Dr. Rainer Haag is gratefully acknowledged for letting me be part of his international, dynamic group and for co-refereeing this thesis. I really enjoyed to work in between the polymer and biophysical world.

For my stay in Vancouver at the UBC, I would like to thank Prof. Dr. Jayachandran N. Kizhakkedathu for giving me the opportunity to work in his lab and helping me in all matters for that time. I thank Anilkumar Parambath for a very good supervision and guidance in Canada, which led to a fast progress in the first weeks of my doctoral student time.

The Block group members, Yannic Kerkhoff, Katharina G. Hugentobler, Stefanie Wedepohl, Johann Plaschke, Helen Wildenauer, Kim Silberreis, and Lisa Glinzig, are kindly acknowledged for a really nice atmosphere, helpfulness, scientific discussions and small coffee or lunch breaks.

I would like to thank the Mensa lunch group for daily social gathering, interesting, and funny conversations. Since the Mensa group is really dynamic and a lot of people are part of this group, I will not mention particular names. Now in pandemic times I miss these social breaks and realize how crucial the shared time was.

The group leaders of the multivalency subgroup, Katharina Achazi, Sumati Bhatia and Daniel Lauster, are thanked for support over the last years. Especially, I have to thank Sumati Bhatia for introducing me to functionalization procedures in the beginning of my doctoral time.

Thank you very much to all technicians of the Haag group, namely Cathleen Hudziak, Elisa Quaas, Anja Stößel, Daniel Kutifa, Marleen Selent, Andrea Schulz, and Katharina Goltsche. All of you were really kind and helpful when I had a question or a concern. Especially I thank Cathleen for performing a lot of GPC measurements and pleasant chats in between. Wiebke Fischer and Eike Ziegler are grateful acknowledged for answering many questions about bureaucracy and other university issues.

Further, I would like to acknowledge the BioSupraMol team for providing fast analysis like elemental analysis and NMR.

Kindly acknowledged is Pamela Winchester for proofreading this thesis.

Many people I have to thank for providing me a pleasant time at the university in and outside from the university. I cannot name all of them particular, therefore I mention



some representatives: Felix Reißbeck, Anna Hermann, Mathias Dimde, Michael Tully, Isabelle Heing-Becker, Boonya Thongrom, Magda Ferraro, Ehsan Mohammadifar, and Chuanxiong Nie....

I have to thank my family and friends for supporting me for the whole period. The support from the very beginning from my father Horst Müller, my mother Susanne Vollmers and my stepdad Sven Vollmers enabled me to study. Without you I have not been able to experience the multicultural scientific world. Also, thanks to my “chemistry uncle” Jan-Robert Schwark for his curiosity of my current state and also for providing advices if needed during my whole studies.

Last but not least I have to thank my own small family, my wife Patricia Wallert, for her support in busy times, her patience, and being there for me in every situation. My daughter Ebba Wallert for little nice and funny distractions at day and night, I love to come home and being greeted with a happy smile.

# Table of Contents

<b>Introduction .....</b>	<b>1</b>
<b>1 Fundamentals .....</b>	<b>2</b>
<b>1.1 Multivalency .....</b>	<b>2</b>
1.1.1 Multivalency principle .....	3
<b>1.2 Viruses.....</b>	<b>4</b>
1.2.1 Influenza Virus.....	5
1.2.2 Multivalent interaction – HA / NA balance .....	8
1.2.3 Monovalent drugs against influenza .....	9
<b>1.3 Polymers as multivalent scaffold .....</b>	<b>10</b>
1.3.1 Polymer architectures.....	12
<b>1.4 Mucus .....</b>	<b>15</b>
1.4.1 Mucin glycoprotein .....	17
1.4.2 Barrier function of mucus .....	19
<b>1.5 Multivalent virus binding inhibitors .....</b>	<b>20</b>
1.5.1 Mucin-inspired virus binding inhibitors .....	21
<b>1.6 Analytical methods for testing virus binding .....</b>	<b>22</b>
1.6.1 Distinctions and limitations of the methods.....	29
<b>2 Scientific goals .....</b>	<b>31</b>
<b>3 Publications.....</b>	<b>34</b>
<b>3.1 Mobility-Based Quantification of Multivalent Virus-Receptor Interactions: New Insights Into Influenza A Virus Binding Mode .....</b>	<b>34</b>
<b>3.2 Automated solvent-free polymerization of hyperbranched polyglycerol with tailored molecular weight by online torque detection .....</b>	<b>57</b>
<b>3.3 Mucin-inspired, High Molecular Weight Virus Binding Inhibitors Show Biphasic Binding Behavior to Influenza A Viruses.....</b>	<b>88</b>
<b>4 Summary and conclusion .....</b>	<b>124</b>
<b>5 Outlook.....</b>	<b>127</b>
<b>6 Zusammenfassung.....</b>	<b>128</b>
<b>7 References .....</b>	<b>131</b>
<b>8 List of abbreviations .....</b>	<b>142</b>
<b>9 List of publications, manuscripts and conferences .....</b>	<b>143</b>
<b>10 Curriculum vitae .....</b>	<b>145</b>

## Introduction

Arising of new viruses is uncertain and therefore an unpredictable human danger. Zika,<sup>[1]</sup> influenza A virus (IAV),<sup>[2]</sup> and corona virus<sup>[3]</sup> illustrate how fast pandemics can appear. Therefore, it is important to develop antiviral drugs or vaccinations<sup>[4]</sup> to prevent viral infection. Unfortunately, both approaches are time-consuming.<sup>[5]</sup> Further, antiviral drugs and vaccinations are often effective just for a certain period until the targeted virus mutates, which may lead to ineffective vaccines<sup>[6]</sup> or resistance against the antiviral drug.<sup>[7-8]</sup> Therefore, alternative ways to prevent and treat virus infection are required.

A new strategy of antiviral drugs is to block viral proteins, which are involved in the cell attachment, by so-called binding inhibitors.<sup>[9]</sup> The advantage of this approach is that the first step of infection (i.e., binding to the cell membrane) is prevented. Thus, viruses cannot enter the host cell. Interactions of single virus proteins with cell membrane receptors (binding entities, e.g., sialic acid structures) are very weak. Therefore, viruses require the formation of multiple interactions in parallel (i.e., multivalent interaction) for firm attachment to cell membranes.<sup>[10]</sup> Accordingly, binding inhibitors have to be designed as well in a multivalent fashion like cell surfaces to ensure sufficient strong binding to viral proteins. Here the problem arises that on one hand, many parameters (e.g., architecture, size, and ligand density) can be varied but the impact of these parameters on the binding efficiency is typically unknown. On the other hand, methods are lacking to investigate the influence of binding inhibitors on the multivalent binding process because until now no method exists that is able to quantify the binding strength of multivalent virus-receptor interactions under equilibrium conditions.

Nature evolved against viral infection an efficient protection barrier, called mucus, which is able to prevent virus binding to cell surfaces.<sup>[11]</sup> The key players of mucus are mucins, huge, highly branched glycoproteins, which are responsible for mucus properties like viscoelasticity and the interaction with infectious agents.<sup>[12]</sup> Due to the presentation of multiple ligands, e.g., sialic acids (similar to cell surface receptors) mucins interact with viral binding proteins and are able to trap these viruses.<sup>[13-14]</sup> This effective method to prevent viral attachment is not virus specific but rather an approach for a broad spectrum of viruses.<sup>[15]</sup>

In this work, the mentioned problems are addressed by the combination of macromolecular chemistry (synthesis and functionalization of polymeric scaffolds, which serve as binding inhibitors) and biophysical methods to investigate the influence of

multivalent binding inhibitors on viral binding. The design of the multivalent binding inhibitors is inspired by mucins.

## **1 Fundamentals**

### **1.1 Multivalency**

The use of multivalency occurs ubiquitously in nature and is an important type of interaction in biological systems.<sup>[10]</sup> In multivalent-binding multiple ligands of one species bind non-covalently to multiple receptors on another species simultaneously.<sup>[16]</sup> The resulting overall binding can be much stronger than the sum of the corresponding monovalent interactions.<sup>[16]</sup> The binding strength of monovalent interactions is called affinity, while the strength of multivalent interactions is stated as avidity. One well-known example where multivalency applies in nature is the burr. The burdock plant presents several small hooks that adhere to fur from animals. This principle was copied by the development of Velcro®, which we use in daily life. Small hooks on a surface entangle with little loops on another surface. One entanglement alone is very weak but the high amount of entanglements enhances the interaction to a strong connection. There are many examples of multivalent interactions in nature, some of them lead to inspired products. Furthermore, some products possess similar multivalent action principles such as DNA strands and zippers (Figure 1).

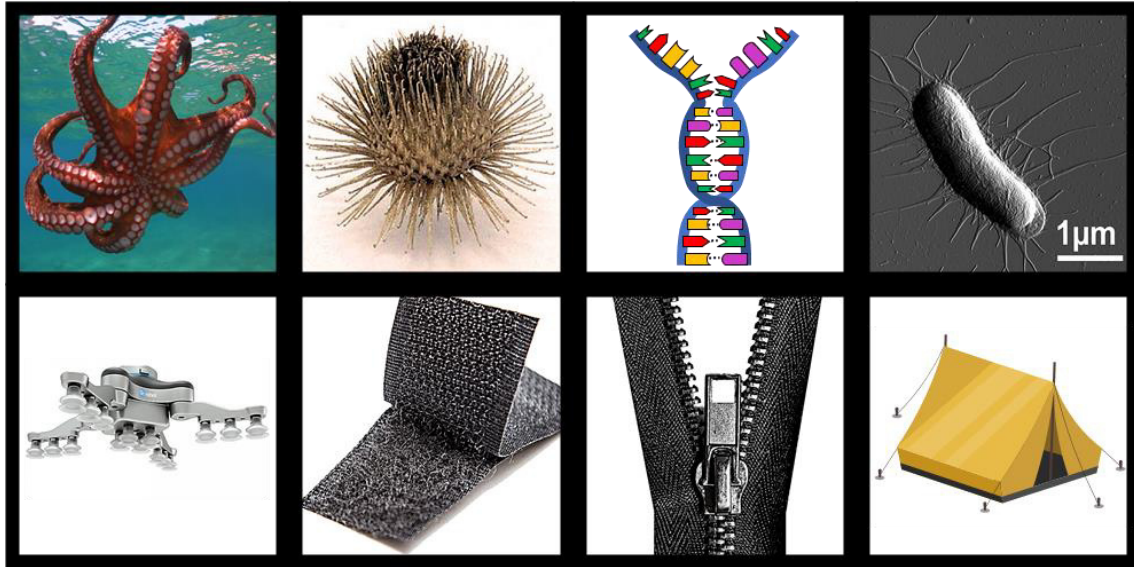


**Figure 1.** Occurrence of multivalency in nature and inspired products or items with similar action principles. Octopus and inspired robot arm with suction cups, burdock, and the inspired Velcron®, DNA strand and similar zipper principle, bacteria, and tent usage multiple anchor points. Adapted with permission from ref.<sup>[17-18]</sup>. Copyright 2012 Klinth et al. PLoS ONE. Copyright 2012 WILEY-VCH Verlag GmbH & Co. KGaA, Weinheim. Copyright 2020 OnRobot GmbH.

### 1.1.1 Multivalency principle

In order to understand the process of multivalent binding the thermodynamics of the process has to be investigated. The free energy ( $\Delta G$ ) of a system determines if a binding process will be performed or not. In case of a negative free energy a process (here binding) occurs spontaneously. The free energy of association ( $\Delta G_N^{multi}$ ) results from a multivalent interaction of  $N$  ligands and  $N$  receptors on two separate entities in an  $N$ th-order and is composed of enthalpic ( $\Delta H_N^{multi}$ ) and entropic ( $\Delta S_N^{multi}$ ) components (Equation 1).<sup>[10]</sup>

$$\Delta G_N^{multi} = \Delta H_N^{multi} - T\Delta S_N^{multi} \quad (\text{Equation 1.})$$

Multivalent scaffolds are able to enhance binding enthalpically due to the fact that the first ligand binds to a receptor and increases the local concentration of ligands, which triggers binding to other receptors with greater enthalpy (more favorable).<sup>[10, 19]</sup> A multivalent scaffold can also have negative effects on the enthalpy, for instance, scaffolds with unfavorable ligand density or orientation. The first ligand binds to a receptor and

other ligands interact less favorable due to interference with the first ligand or the scaffold has to bend to achieve successful binding of further ligands to neighboring receptors.<sup>[10]</sup> The entropy component ( $\Delta S_N^{multi}$ ) in Equation 1 contains the translational, rotational, and conformational entropy. Here also the scaffold of multivalent system as a great influence. Very flexible scaffolds with a low number of ligands fail due to entropic reasons.<sup>[20-21]</sup> In aqueous solution a major reason for increasing entropy is the release of oriented water from the binding target (e.g., the virus).<sup>[22-23]</sup> Hence, the larger size of multivalent scaffolds is able to displace more water molecules by formation of hydrophobic and electrostatic interaction making binding more favorable in comparison to small monomeric binders.<sup>[22]</sup>

Furthermore, the collectively binding prevents the dissociation independent even though individual transient unbinding events occur.<sup>[19]</sup> Hence, the rebinding possibility of unbound ligands is higher because the scaffold forces the ligand to stay in place.<sup>[24]</sup>

## 1.2 Viruses

All viruses have in common that they need a host to multiply. Hence, the initial step of a viral infection is binding to the plasma cell membrane of a host cell. Most single virus-receptor interaction are weak (i.e., equilibrium dissociation constant  $k_D$  in low mM range).<sup>[25]</sup> Therefore, viruses form multiple interactions to achieve a sufficient strong attachment to the cell surface.<sup>[10]</sup> Viruses leverage multivalency to enhance their weak monovalent binding interactions. Successful proliferation of viruses requires more than just the attachment. After attachment the virus have to enter the host cell.<sup>[26]</sup> Inside the cell, the genomes of the virus have to be released by uncoating in a pH-controlled process.<sup>[27]</sup> Then, the viral genome has to enter the nucleus of the cell, where transcription and replication happens.<sup>[26]</sup> Finally, assembly and release of progeny viruses (new formed viruses) have to happen in multi-step process.<sup>[28]</sup> A viral infection involves all mentioned steps and is called infection cycle (Figure 2). All steps in the infection cycles have to be accomplished to achieve a successful infection with a resulting proliferation. Hence, antiviral drugs targeting certain steps of the infection cycle and try to interfere the process. For example, one type of antiviral drugs is a binding inhibitor, which try to prevent the attachment or the release of viruses by binding to membrane proteins of the virus.

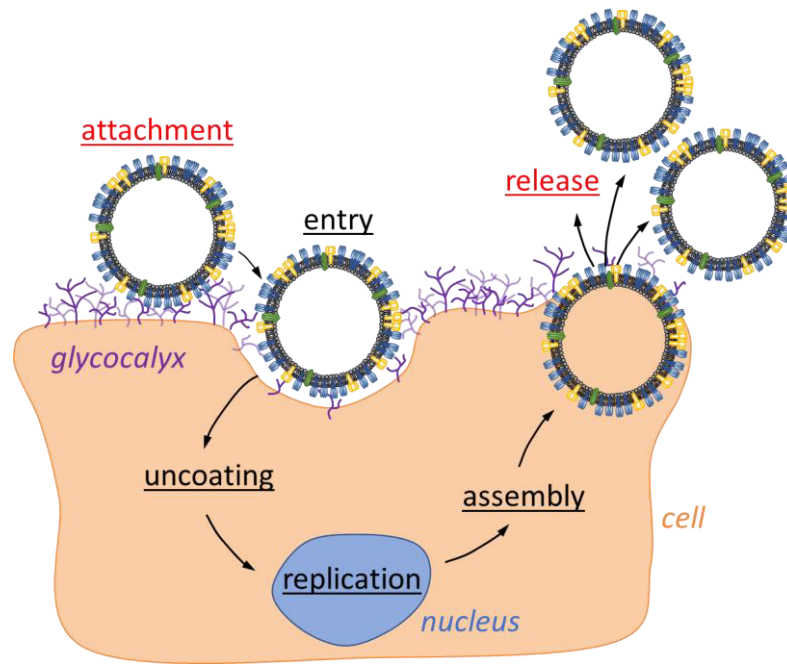


**Figure 2.** Infection cycle of viruses with main actions: Attachment, entry, uncoating, replication, assembly, and the release of new generated viruses.

### 1.2.1 Influenza Virus

This work focuses on influenza viruses because it is estimated that seasonal flu causes 300,000 to 650,000 influenza-associated respiratory deaths worldwide annually.<sup>[29]</sup> Further, the most fatal pandemic in 1918 with 40 to 50 million deaths as well as many other pandemics resulted from influenza viruses.<sup>[30-31]</sup> The most recent influenza pandemic occurred 2009.<sup>[2]</sup> Until now there is no general antiviral drug available. Hence, with better knowledge of influenza virus behavior, new approaches to prevent infection can be developed.

Influenza viruses belong to the family of *Orthomyxoviridae* and can be divided into three main types: influenza A, B, and C.<sup>[32]</sup> Among these three, influenza A is the most relevant since it is responsible for all known major influenza epidemics and pandemics.<sup>[33]</sup> Therefore, influenza type A is studied in this work.

Influenza A viruses (IAVs) are pleomorphic.<sup>[34]</sup> While lab-cultured viruses are usually spherical ( $d \sim 100$  nm), freshly isolated viruses from patients are generally elongated.<sup>[34-36]</sup> The outer membrane of the virus, also known as envelop, is equipped with the membrane proteins hemagglutinin (HA) and neuraminidase (NA), in addition M2 ion channel proteins are also placed in the membrane. The structure of the HA complex consists out of three HA proteins, which are responsible to bind sialylated receptors at the cell surface. The tetrameric NA complex is responsible to cleave sialic

acids in order to enable the escape of progeny viruses (newly formed viruses) from the host cell. The whole envelope is stabilized by the M1 protein, which is located below the membrane. In the inner part of IAVs are eight single-stranded negative-sense RNAs embedded that carry the genetic information for replication of new viruses (Figure 3).<sup>[37]</sup>

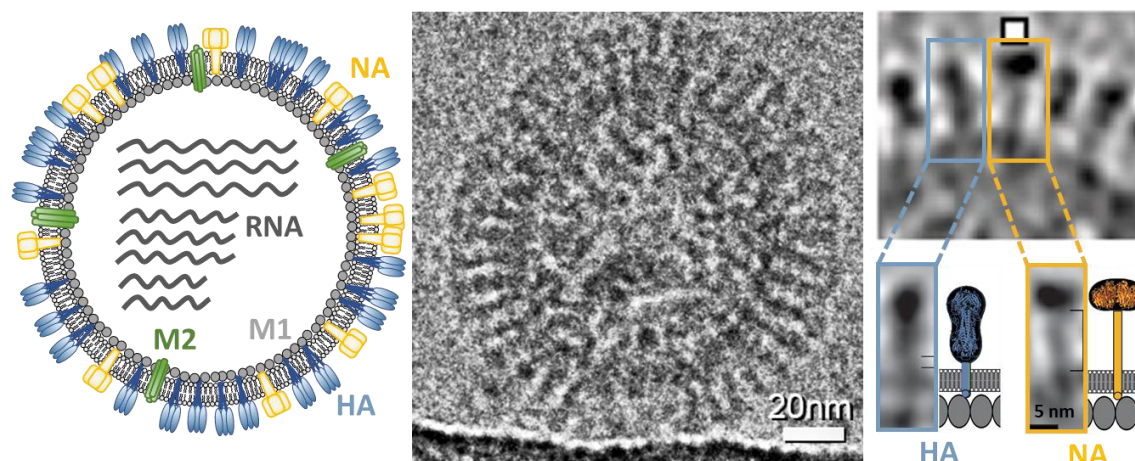


**Figure 3.** Structure of Influenza A virus with its components hemagglutinin (HA), neuraminidase (NA), ion channel proteins M2 located in the envelope and the stabilizing protein M1 below the membrane. The negative-sense single-stranded RNA is embedded in the virus (left). Cryo-electron microscopy picture of an influenza A virus (middle). Zoomed cryo-electron measurement of the membrane proteins HA and NA in a viral membrane (right). Modified with permission of ref.<sup>[38]</sup>. Copyright (2006) National Academy of Sciences.

This thesis focuses on the binding of viruses and since HA trimers and NA tetramers are the main actors in the binding process (attachment and detachment), they will be described here in more detail. Harris et al. quantified the number of HA and NA proteins of IAV X31 via cryo-electron tomography, which resulted in ~300 HA trimers and ~50 NA tetramers per virus.<sup>[38]</sup> The surface of IAVs is packed closely, with one HA trimer or NA tetramer occupying 120 nm<sup>2</sup>. Furthermore, they investigated cluster of NAs within the envelop.<sup>[38]</sup>

IAVs can be differentiated in subtypes based on the membrane proteins HA and NA. Known are eighteen types of HA and eleven of NA.<sup>[39-40]</sup> Humans are mostly susceptible to three HA (H1 to H3) and two NA (N1 and N2) until now.<sup>[33]</sup> Due to the high mutation of influenza viruses also other HA or NA subtypes could adapt to humans in future.<sup>[2]</sup> Antigenic drift is a continuous process and describes small changes in the genes of IAVs that could lead to different susceptibility properties due to changes in the membrane proteins HA and NA.<sup>[41-42]</sup> Another type of mutation is called antigenic shift, which can arise from genetic reassortment (e.g.. mixing genes from avian and human



viruses) in a intermediate host for instance pigs (Figure 4).<sup>[33]</sup> This major change happens rarely but its pandemic potential is high. Examples are the Asian flu (1957; H2N2), Hong Kong flu (1968, H3N2), and the swine flu (2009, H1N1).<sup>[2]</sup>

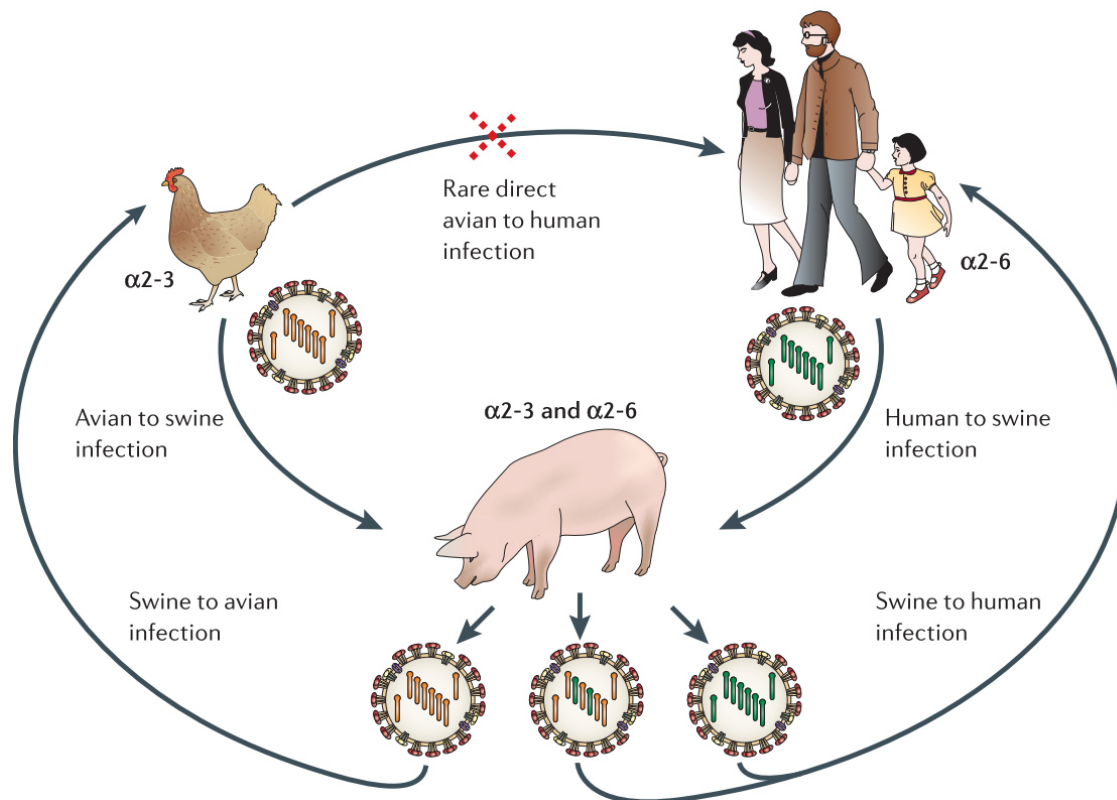


**Figure 4.** Mutations of influenza viruses by antigen-shift can occur by mixing of avian and human genes in an intermediate host, e.g., a pig during the reassortment. Antigen-shifts lead to a major change in the virus infection potential and can cause the arise of a pandemic. Reprinted with permission from ref.<sup>[33]</sup>. Copyright 2006, Springer Nature.

The different HA types bind with a high specificity to certain hosts. A conventional interpretation is that human influenza viruses show preferred binding to  $\alpha$ -2,6-linked sialic acids, whereas avian influenza viruses prefer  $\alpha$ -2,3-linked sialic acids.<sup>[43]</sup> This interpretation resulted from the location of the sialylated receptors. The upper human airways (trachea and bronchi) express mainly  $\alpha$ -2,6-linked sialic acids, which explains preferred human infection by easier accessibility to these receptor moieties.<sup>[44]</sup> Nevertheless, the lower human airways (non-ciliated bronchial cells and the junction between bronchiole and alveolus) express also  $\alpha$ -2,3-linked sialic acids and are susceptible to avian influenza viruses but they are harder to reach. According to Zanin et

al., this is an oversimplification since there are numerous  $\alpha$ -2,3-linked and  $\alpha$ -2,6-linked sialic acids in the glycocalyx with different length, topology, and complexity.<sup>[12]</sup>

### 1.2.2 Multivalent interaction – HA / NA balance

The interaction of a single sialic acid-containing receptor to HA within intact IAVs is weak ( $\alpha$ (2,3)-sialyllactose  $k_D = 3.5$  mM and  $\alpha$ (2,6)-sialyllactose  $k_D = 2.7$  mM).<sup>[45]</sup> Therefore, multiple bonds have to be formed to accomplish an attachment to the cell surface.<sup>[10]</sup> While HA is responsible to form bonds to sialic acid on target cells, NA is responsible to cleave sialic acids.<sup>[46]</sup> The cleavage feature of IAVs is important to release progeny viruses from the host cell,<sup>[47]</sup> prevent their aggregation,<sup>[48]</sup> and enables the virus to penetrate the mucus barrier of cells that also present sialic acid moieties to trap viruses.<sup>[12, 37, 49]</sup> The interplay of the HA binding properties and the NA cleaving properties is called HA/NA balance and is essential to fulfill the whole infection cycle.<sup>[46]</sup> Without an optimal interplay of receptor binding and cleavage proliferation of viruses would fail.<sup>[46]</sup> For better understanding two examples are given in the following, which explain the extreme cases. A combination of strong binding HA and weak cleaving NA protein would fail to penetrate the mucus and would not be able to release the host cell. A combination of strongly cleaving NA and weakly binding HA would not infect cells due to inability of efficient attachment. Richard et al. showed that a IAV strain with deficient NA was still able to replicate due to the low affinity of HA for SA binding.<sup>[50]</sup>

Nowadays, researchers investigate NA's contribution during the binding process to sialic acids.<sup>[32, 51]</sup> The analysis of the x-ray structure of sialic acid and NA revealed a second binding site on NA, which does not cleave sialic acids in contrast to the enzymatically active binding site of NA.<sup>[52]</sup> Recent computational studies indicate that sialic acid shows two times faster binding to the second binding site compared to the active binding site.<sup>[53]</sup> Zhu et al. supports the idea of NA binding contribution by investigation of much higher equilibrium dissociation constants between sialosides and NA ( $k_D \sim \mu\text{M}$ ) compared to sialosides and HA ( $k_D \sim \text{mM}$ ).<sup>[54]</sup>

A lot of studies point out that NA is involved in the attachment to cells and show the importance of the HA/NA balance.<sup>[37, 53-55]</sup> Nevertheless, the true contribution of NA in the attachment process and the interplay between HA and NA is still not well understood. Further, the importance of multivalency during attachment and release is still under debate in many studies most probably due to insufficient methods to unravel the multivalent interaction (see Section 1.6).

Parameters that influence the HA/NA balance are different subtype combinations, host receptor specificity, and stalk length of HA and NA.<sup>[46]</sup> Most probably specific subtype combinations (e.g., H3N2, H1N1) have been developed since their HA/NA balance enabled to infect hosts more efficiently than others.

### **1.2.3 Monovalent drugs against influenza**

Currently, most antiviral drugs against influenza are highly specific small molecules that block membrane proteins to prevent infection.<sup>[56]</sup> They can be divided into two major classes, namely, M2 channel protein blocker and neuraminidase inhibitor.<sup>[56]</sup> Amantadine and rimantadine bind to the M2 proton channels, which is important in the process of uncoating, assembly, and budding.<sup>[57]</sup> Commercial monomeric neuraminidase inhibitors are, e.g., zanamivir, peramivir, oseltamivir, and laninamivir.<sup>[58]</sup> However, the weak point for the attempt of using small specific molecules as antiviral drugs is that influenza viruses mutate continuously due to antigenic drift. Just small mutational changes at the membrane protein can cause less specific binding, which may result in a drastically decrease in binding efficiency. Due to this reason rapid resistance emerged, in particular to amantadine, rimantadine, and oseltamivir.<sup>[59-60]</sup>

As it was shown for viruses, multivalent binding enables to generate sufficient strong binding even if a single interaction is weak. Therefore, the use of a multivalent scaffold with several attached binding moieties could enhance the efficiency of binding inhibitors such as virus binding to the host cell (Figure 5). Further, the backbone of the multivalent binding inhibitor could also shield the virus, which would support the binding inhibition process.

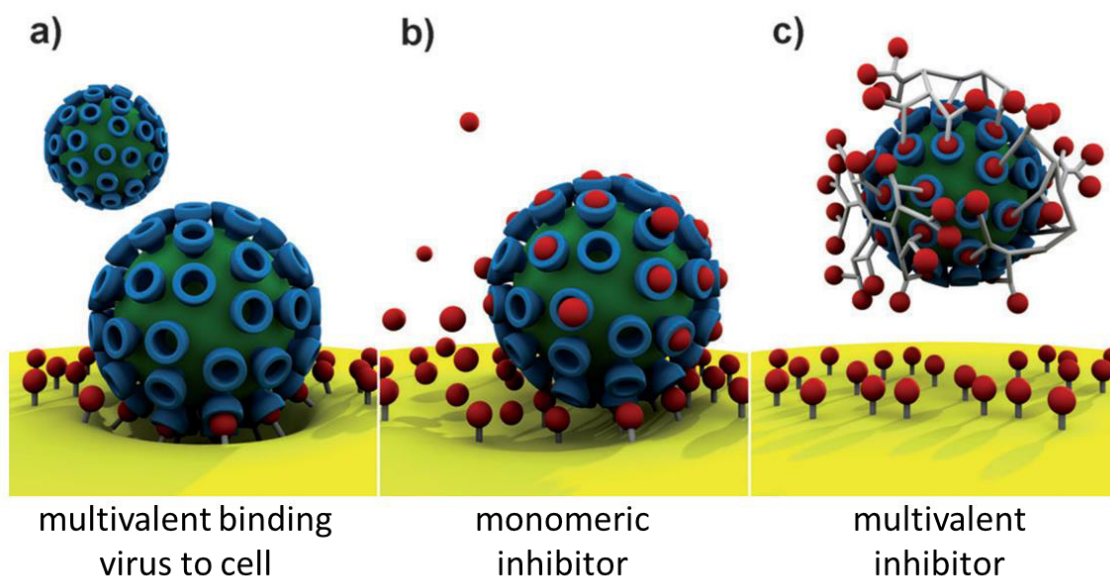


**Figure 5.** Multivalent binding of a virus to the cell surface. (a) The virus attaches to the cell surface, which is the first step of infection. (b) Monovalent binding inhibitors block some viral binding protein and decrease the avidity of the virus to the cell surface. (c) Multivalent binding inhibitors prevent virus binding to the surface by efficient binding to the viral protein and additional steric shielding of the polymer scaffold. Reprinted with permission from ref.<sup>[17]</sup>. Copyright 2012 WILEY-VCH Verlag GmbH & Co. KGaA, Weinheim.

### 1.3 Polymers as multivalent scaffold

The use of multivalency is a common approach to enhance binding.<sup>[19]</sup> Many features influences the binding efficiency of multivalent systems, for instance, the type and number of ligands (valency), their orientation, density and spacing between ligands.<sup>[10,61]</sup> In addition, the scaffold properties like size, flexibility, and shape play an important role.<sup>[62-63]</sup> Due to huge variety of adaption possibilities synthetic multivalent systems have a great potential to become tailor-made for a dedicated application such as the inhibition of IAVs.

With the use of polymeric scaffolds, a systematic probing of ligand valency, density, linker length, orientation, flexibility, etc., can be performed. The focus of this chapter will be on polymer architectures, which can be used as multivalent scaffolds (Figure 6).

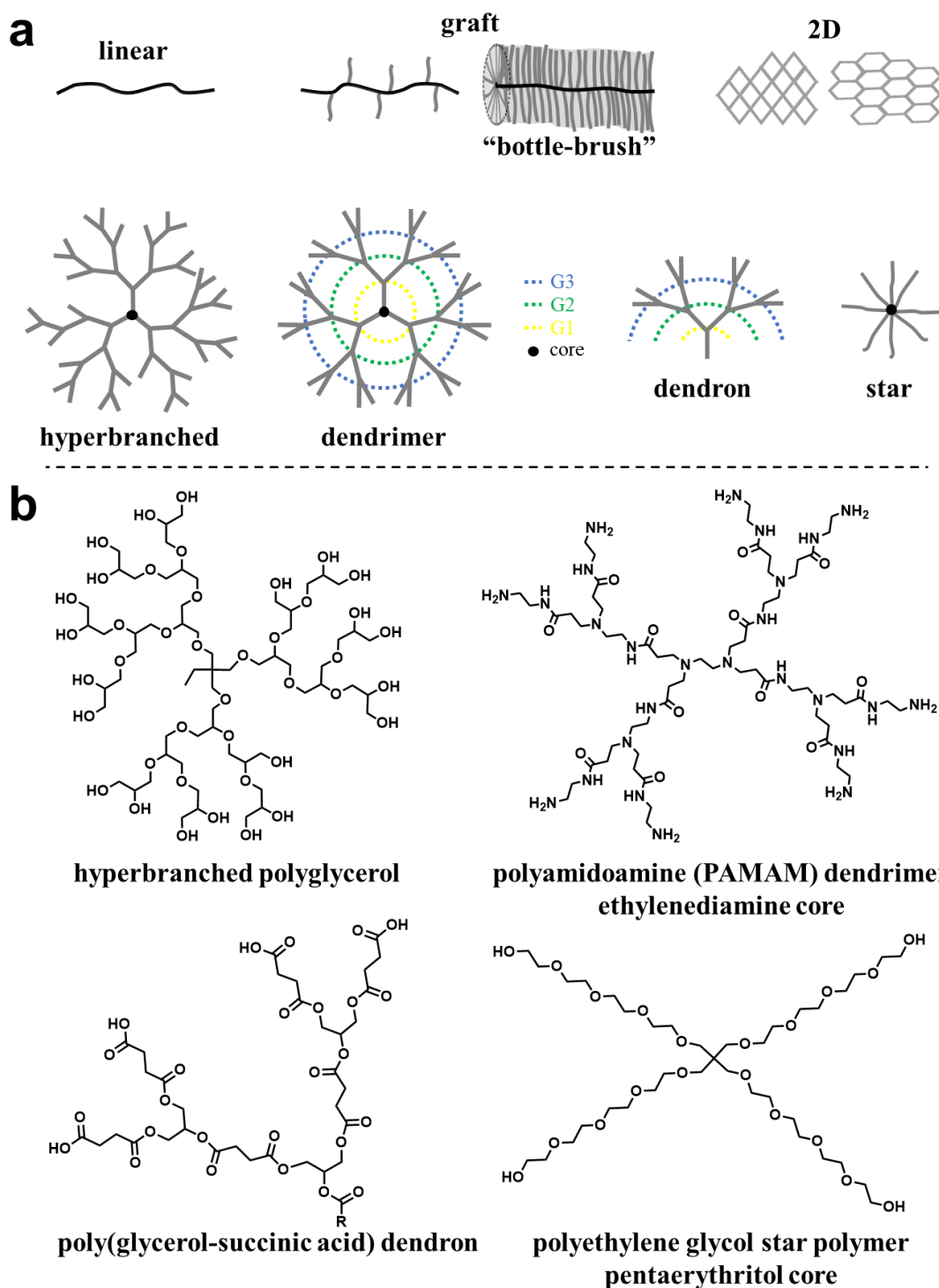


**Figure 6.** Different types of polymer architectures for possible multivalent scaffolds. G stands for the generation and defines the number of branching points in case of dendrimers and dendrons (a). Common polymer examples for different polymer architectures (b).

The schematic presentation of polymer architectures is simplified to show a clear overview of the differences in polymeric architectures. In reality the shape of polymers

depend on many factors like solvent, temperature, polymer concentration, applied shear-stress, etc.<sup>[64-65]</sup>

### 1.3.1 Polymer architectures

**Linear polymers** – Linear polymers are obtained by conventional polymerizations, where an initiator starts the propagation of monomers in one direction until the chain gets terminated. The resulting polymers have two end groups. It has to be taken into account that the end groups can be shielded by the polymer backbone since the conformation of the linear polymer is random.<sup>[66]</sup> Glick et al. probed linear bivalent virus inhibitors and investigated no enhancement in comparison of the monomeric binding site.<sup>[20-21]</sup> Even though the inner monomers are functionalized to obtain a multivalent scaffold, it is not sure if the ligands are exposed. On the other hand, the flexible property of linear polymers is advantageous because the scaffolds can adapt their shape to the target.<sup>[63]</sup> Linear stiff scaffolds can be prepared from coiled peptides, where fine-tuned ligand presentation is possible.<sup>[67-68]</sup>

**Graft polymers** – Graft polymers have a linear backbone with attached side chains. They can be prepared using three different approaches namely grafting-to, grafting-from and grafting-through.<sup>[69]</sup> In the grafting-to method prefabricated polymeric grafts are attached to the backbone.<sup>[70]</sup> The grafting-from approach uses reactive moieties on the backbone to grow polymer chains away from the backbone.<sup>[71]</sup> Grafting-through is the polymerization of polymeric monomers, also called macromonomers, which lead to highly grafted architectures.<sup>[72]</sup> The density of grafting defines the degree of chain extension of the grafts. At low-grafting densities, pendant polymer chains collapse to more globular morphology, which is stated as mushroom shape.<sup>[73]</sup> In contrast, high grafting densities lead to elongated chains, which are packed tightly.<sup>[73]</sup> This phenomenon has to be considered in case of using grafted architectures as multivalent scaffolds since the end groups of the pendant polymers are not exposed in low grafted polymers. Fully grafted polymers, where each repeating unit has an attached side chain, are defined as bottle-brush polymers.<sup>[69]</sup> The high grafting density results in unique properties for instance no entanglement like linear block copolymers and self-assembly to stiff cylindrical structures sized up to several hundred nanometers.<sup>[74]</sup>

**Dendrimers and dendrons** – Dendrimers are perfectly branched polymers (degree of branching 100%), which possess a core from which the branching emanates in several directions.<sup>[75]</sup> If the branching just occurs to one direction, dendrons are created. Dendrons can be converted to dendrimers by linking dendrons to a core molecule. Both architectures have in common that they are prepared stepwise and reach with this approach high control, which leads to monodisperse systems. Due to the stepwise fashion, the dendrimer and dendron synthesis is costly and time-consuming. Each new branching point, going from the core to the periphery, is defined as generation. The first branching point at the core is generation one (G1), the second on top of that is generation two (G2), etc.<sup>[75]</sup> Dendrimers or dendrons with higher generations have more end groups. Due to the defined structure all end groups are on the exterior, which is an advantageous for designing binding inhibitors due to easy availability<sup>[19]</sup> and capability of high ligand density functionalizations.<sup>[76]</sup> The most used dendrimer scaffold is poly amidoamine (PAMAM). Advanced dendrimer chemistry was performed to design dendrimers with different orthogonal functional groups at one dendrimer, which enables us to design controlled multivalent systems with heterogeneous ligands at the exterior (Figure 7).<sup>[77]</sup> This method can be important since the binding affinity is also influenced by patterns of binding sites.<sup>[16]</sup> Further, dendrimers with different dendron faces were developed, which enable heterogenous ligand presentation with local high density of the same ligands (Figure 7).<sup>[78-79]</sup> This approach could be of interest if binding targets possess different receptor clusters.<sup>[80]</sup>

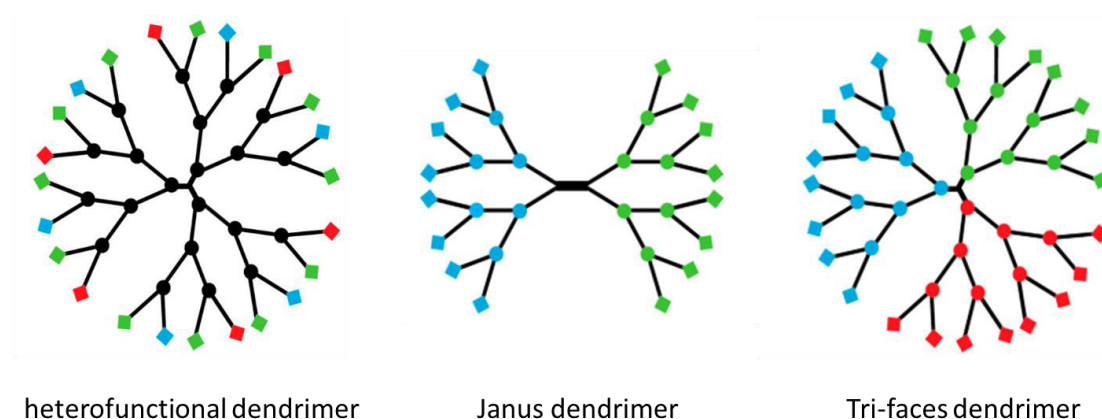


**Figure 7.** Advanced dendrimer structures. Different dendrons are assembled to a core resulting in heterofunctional dendrimer, Janus dendrimer and Tri-face dendrimer. Modified with permission from ref.<sup>[80]</sup>. Copyright 2012 MDPI

**Hyperbranched polymers** – Hyperbranched polymers are polymerized with branching monomers. Every reacted monomer ( $AB_x$ ) creates two or more possibilities to propagate. Most common are  $AB_2$  monomers,<sup>[81-82]</sup> which expose two new possible propagation sides.  $AB_3$  or  $AB_4$  monomers are rarely used.<sup>[83-84]</sup> The branching is not perfect with this polymerization approach, for instance, hyperbranched polyglycerol has a usual degree of branching about ~ 60 %.<sup>[85]</sup> The main advantage is that the polymerization is done in one-pot-synthesis, which is convenient, fast, and inexpensive and making it also suitable for larger-scale applications.<sup>[86]</sup> Even though the degree of branching is lower compared to dendrimers, the properties are similar. Both architectures show excellent solubility, low solution viscosity, and high number of terminal end group functionalization.<sup>[86-87]</sup> Due to the ease in functionalization of the terminal end groups at the periphery, hyperbranched polymers are often used to design multivalent binding inhibitors.<sup>[88-89]</sup>

**Star-polymers** – Star-shaped polymers can be prepared in two different approaches. First, the “core-first” approach, where a multifunctional core is used to initiate propagation of the arms.<sup>[90]</sup> Second, the “arm-first” approach connects prefabricated linear polymers to a core molecule.<sup>[90]</sup> The chosen core molecule predefines the number of the resulting arm at one core molecule. Mostly the “arm-first” approach is used. Extensively studied are controlled radical polymers techniques like reversible addition-fragmentation chain-transfer (RAFT) and atom transfer radical polymerization (ATRP) polymerization.<sup>[91-93]</sup> In the recent years, just a few examples of “core-first” star polymers are published, mainly using polyethylene glycol as arms.<sup>[94-95]</sup> Common, numbers of star polymer arms are 3 to 8.<sup>[90]</sup> Nevertheless, dendrimers can also be used as core molecule. Lam et al. used a PAMAM G1 and G2 dendrimer as core and grow 16 and 32 arms out of L-lysine by N-carboxyanhydride (NCA) polymerization on it.<sup>[96]</sup>

**2D polymers** – This polymer architecture is a relative new field in polymer chemistry.<sup>[97]</sup> These 2D polymers fulfill the definition of Staudinger about macromolecules, which states that small molecules (repeating units) are covalently linked with each other.<sup>[98-99]</sup> The sheet-like architecture provides a high surface area, which is advantageous for binding interaction in biological systems. The synthesis of 2D polymers differs from usual approaches, because the monomers have to be placed in order before they are covalently linked.<sup>[99]</sup> Required for the synthesis is that the monomers do not react spontaneously rather start to polymerize after inducing an external stimulus like light. The



assembling of the monomers are done within the layers of a stacked monomer crystal or they are assembled on the water surface (Langmuir-Blodgett approach) before an external stimulus initiate the reaction.<sup>[99]</sup>

**Hybrid architectures** – Various types of polymer architectures are presented, but there are far more possibilities by the combination of different types of polymer architectures (Figure 8). Doycheva et al. created a multi-arm star polymer consisting of a hPG core with PEG arms.<sup>[100]</sup> Wilms et al. synthesized a linear amphiphilic block copolymer where hPG was grafted on the hydrophilic part to increase the hydrophilicity.<sup>[101]</sup> Reuters et al. tested different polymer architectures as scaffold for virus binding inhibition also dendronized linear polymer scaffolds.<sup>[102]</sup> Therefore, polymer chemists have a crucial toolbox for designing multivalent scaffolds with various architectures, which is powerful for tailoring binding inhibitors for specific applications.

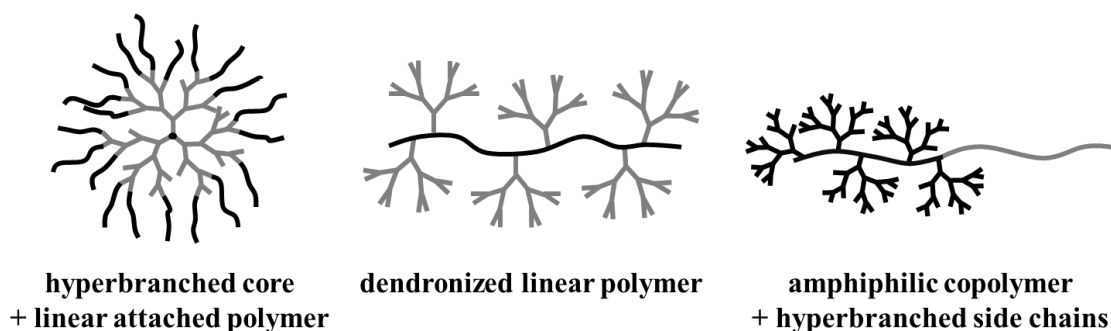


**Figure 8.** Examples for the combination of different polymer architecture types, here called hybrid polymer architectures

## 1.4 Mucus

Mucus is a sticky coating of all wet epithelia and is almost ubiquitously present in all biological systems.<sup>[103]</sup> Mucus layers fulfill several functions, for instance, as lubricate for passages of food or excrement, as maintenance of hydration, as barrier for pathogen and as semipermeable layer for exchange gases and nutrients (Figure 9).<sup>[103]</sup>

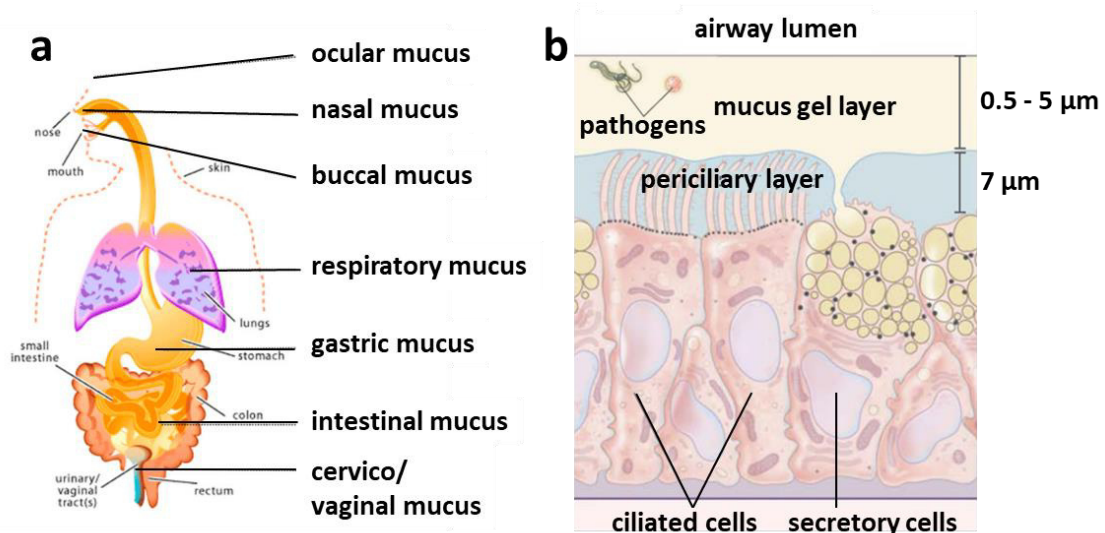


**Figure 9.** Occurrence of mucus in the human body (a). Schema of bronchial epithelia cells consisting out of ciliated cell (aim mucus transport) and goblet cells, which secrete up to  $1\ \mu\text{m}$  big mucus granules (yellow) and proteins (black). Above the cells a mucus layer is located that prevent pathogen penetration (b). Adapted with permission from ref.<sup>[103-104]</sup>. Copyright 2016 MDPI. Copyright Massachusetts Medical Society.

The thickness of the mucus layer varies within the human body. On the eye<sup>[105]</sup> and in the trachea<sup>[106]</sup> it is 2 to  $10\ \mu\text{m}$ , in the stomach<sup>[107]</sup>  $\sim 150\ \mu\text{m}$  and the thickest mucus layers appear in the colon<sup>[108]</sup> up to  $800\ \mu\text{m}$ . The certain thickness is adjusted by the rate of secretion and the rate of degradation and shedding.<sup>[109]</sup> Thus, the mucus layer is replaced by freshly secreted mucus from goblet cells within the epithelial tissue. Each day around 10 L of mucus is produced and secreted in the gastrointestinal tract.<sup>[110]</sup>

This work focuses on the respiratory tract because this is the target of many viral infections. The mucus layer is able to trap viruses and prevent that they reach and infect the cells underneath. Trapped pathogens are cleared within the mucus and are transported up and out of the lungs by cilia movement to get swallowed or spit out. The  $6 - 7\ \mu\text{m}$  long cilia are beating 12 to 15 times per second,<sup>[111]</sup> which results in a velocity of the mucus layer of  $\sim 100\ \mu\text{m/s}$  clearing the lung within minutes to hours.<sup>[109]</sup> The shear thinning behavior of mucus is for the clearance an important property, because by applying shear stress, e.g., by the cilia beats reduces the viscosity of the mucus and helps to move the mucus layer (Figure 10). In diseases, hyper-secretion or dehydration can occur. The clearance is supported by coughing, which also reduces the viscosity of the mucus due to high shear rates.

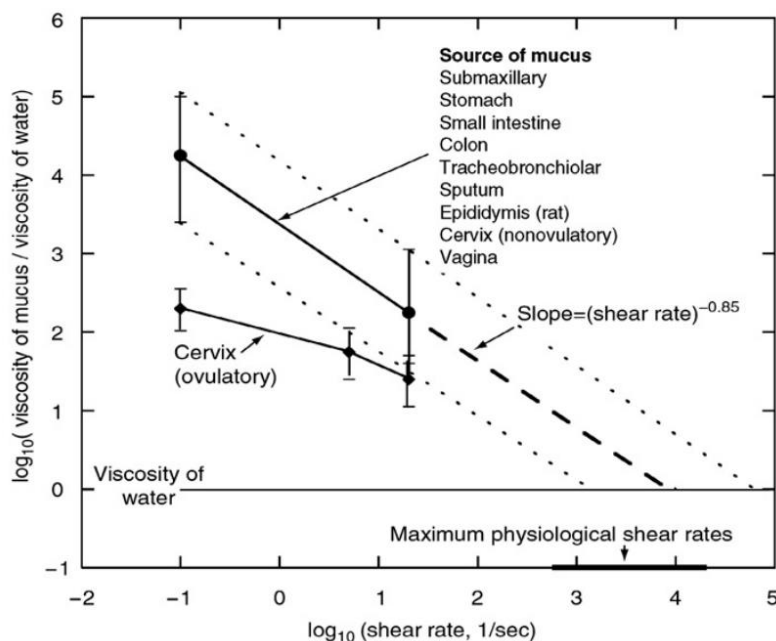


**Figure 10.** Shear thinning behavior of several types of mucus. The viscosity decreases strong with increasing shear rates. Reproduced with permission from ref.<sup>[109]</sup>. Copyright 2008 Elsevier B.V.

Mucus is a hydrogel and is mainly composed out of water (90 – 95 wt.%). Furthermore, mucus contains 2 – 5 wt.% high molecular weight glycol proteins called mucins, which have major influence on mucus properties, e.g., viscoelasticity, and pathogen binding. Minor components are lipids (1 – 2 wt.%), salts (up to 1 wt.%), DNA (0.02 wt.%). The present DNA as well as residues of actin; proteins originate from cellular debris of epithelial cells.<sup>[112]</sup>

#### 1.4.1 Mucin glycoprotein

Mucins are fibrous glycoproteins in the size of 0.5 to 20 MDa.<sup>[113]</sup> The linear backbone is out of a protein sequence with up to 6000 amino acids and is called PTS region due to the high amount of proline, threonine, and serine residues.<sup>[114]</sup> On the protein backbone are N- and O-glycosylated oligosaccharides with 5 – 15 sugar monomers attached. Most abundant sugars are N-acetylgalactosamine, N-acetylglucosamine, fucose, galactose, and sialic acid (N-acetylneuraminic acid).<sup>[113]</sup> Due to the high glycosylation the sugars ratio comprise 80 wt.% of the mucin.<sup>[115]</sup> The high glycosylation is also responsible for the extended fibrous morphology. Kramer et al. investigated synthetic mucins with different glycosylation and proven via atomic force microscopy (AFM) the trend of enhanced extension with a higher degree of glycolization.<sup>[116]</sup> Additionally, the high

amount of terminal sialic acid and sulfate moieties creates a negatively charged surface, which supports the elongated morphology of mucins by charge repulsion.<sup>[112]</sup>

At the C and the N terminus of the PTS region a high amount of cysteines are present, which enables mucins to di- or multimerize by disulfide bond-linking to chains with sizes up to several microns. Sheehan et al. investigated the multimerization of more than 16 linked MUC5AC monomers.<sup>[117]</sup> Brayshaw et al. visualized via AFM the cleavage of mucin to its subunits or smaller multimers by reduction of in-chain disulfide bond using dithiothreitol (DTT).<sup>[118]</sup> A schematic drawing of the mucin structure and the multimerization of is shown in Figure 11. Further, the disulfide-linking also leads to crosslinking of multimers resulting in a network with a wide mesh size.

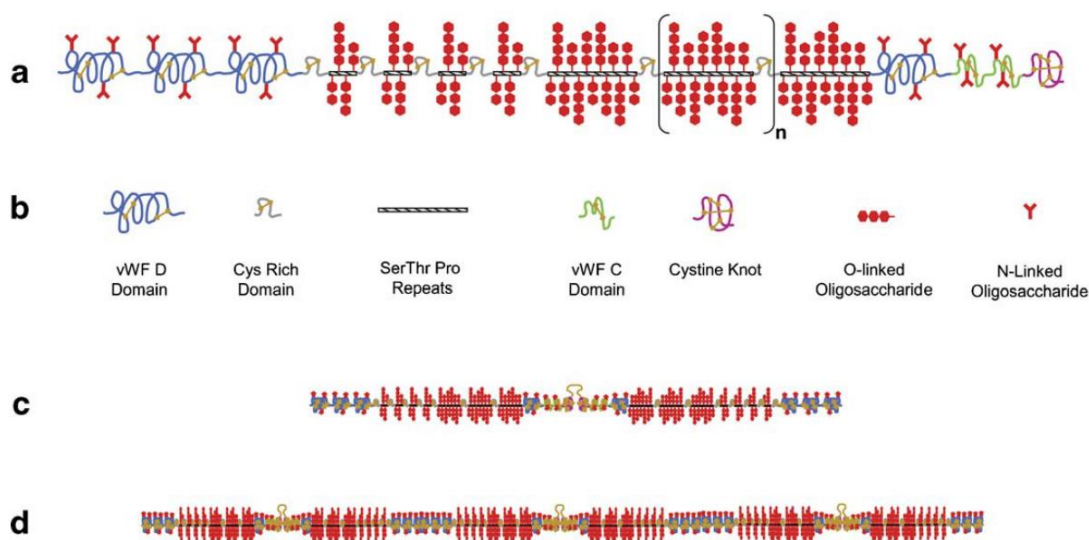


**Figure 11.** Schematic drawing of the pig gastric mucin monomer and its multimerization. (a) Pig gastric mucin monomer with highly glycosylated PTS region and cysteine rich terminal flanks is a secreted gel-forming mucin. (b) Legend for the different domains of the mucin structure. (c) Mucin dimer is connected via disulfide bonds. (d) Multimerization of mucin monomers form chains up to  $\mu\text{m}$  ranges. Reprinted with permission from ref.<sup>[113]</sup>. Copyright 2005 Published by Elsevier Ltd.

In human, 19 different designated mucin genes are identified,<sup>[113]</sup> which can be divided into three subfamilies. First, secreted gel-forming mucins build a hydrogel layer on top of epithelial cells, e.g., MUC5B or MUC5AC in the respiratory tract. Second, cell-surface mucins are attached at the cell membrane and form the glycocalyx. Third, secreted non-gel-forming mucins, which are not able to multimerize or crosslink due to the lack of cysteine rich regions.<sup>[11]</sup> Nevertheless, mucin research is still ongoing because the characterization is due to the high molecular weight, multimerization, aggregation, and

high degree of glycosylation not trivial. An example for the complex analysis of the respiratory mucins MUC5B and MUC5AC is shown in ref.<sup>[119]</sup>.

#### 1.4.2 Barrier function of mucus

This thesis investigates multivalent binding interaction of viruses. Hence, the protection function of mucus against infectious agents is of high interest, therefore it is addressed here in more detail. Mucus is able to control the permeability of objects selectively (Figure 12). Nutrients, water, gases, proteins, and antibodies can diffuse through the mucus layer, while most infectious agents get trapped.<sup>[120]</sup> The filtering principle is not only physical driven by the mesh size of mucus (20 – 200 nm).<sup>[121]</sup> Lieleg et al. suggested that the filtering specificity of mucus is mainly controlled by electrostatic interactions since the diffusion of particles can be regulated by changing the pH value or the salt concentration.<sup>[122]</sup>

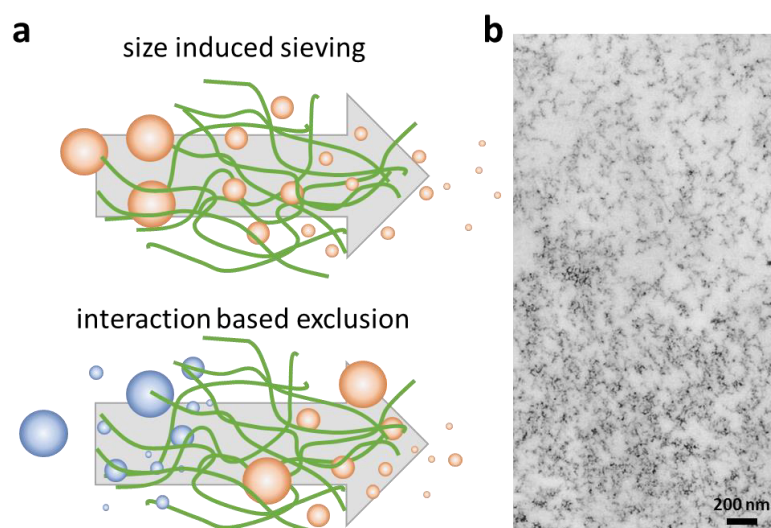


**Figure 12.** Scheme of mucus and the ability of selective filtration by size and interaction (a). Fixed human cervical mucus imaged with transmission electron microscopy. (b). Local mucin density varies and the mesh size ranges from 10 to 200 nm. Reproduced from ref.<sup>[121]</sup>. Copyright 2001 The Biophysical Society. Published by Elsevier Inc.

Olmstedt et al. investigated the diffusion of macromolecules and virus-like particles (VLPs) in human cervical mucus using fluorescent recovery after photobleaching (FRAP).<sup>[121]</sup> The results show 100 to 1000 times lower diffusion of herpes simplex virus (HSV) VLPs ( $d = 180$  nm) in presence of mucus compared to diffusion in PBS. The same effect was observed with polystyrene microspheres ( $d = 59$  nm – 1000nm), which suggests that the deceleration is not only caused by the mesh spacing

rather than the formation of multiple low-affinity bonds. Surprisingly, the authors also measured that VLPs of the human papilloma virus ( $d = 55$  nm) and norovirus ( $d = 38$  nm) diffuse unhindered in mucus. Another study shows as well diffusion retardation and lower infection of influenza viruses ( $d = 100$  nm) in presence of mucins.<sup>[15]</sup>

Furthermore, other low-affinity bonds like hydrophobic interaction or hydrogen bonding take place and also contribute to the biochemical adhesion.<sup>[103]</sup> A detailed study that determines the contribution of each interaction type, which take part in mucin-pathogen binding is until now not fully investigated.

## 1.5 Multivalent virus binding inhibitors

The principle design of multivalent virus binding inhibitors inspired by mucins was introduced by the group of Whitesides.<sup>[10]</sup> With this innovative approach many researchers get inspired and are still developing multivalent virus-binding inhibitors. The common feature of all here mentioned virus-binding inhibitors and natural mucins are that they present multiple sialic acids that interact with viruses in a multivalent fashion. The interplay of multiple weak interactions between the binding inhibitor and the virus results in much higher binding affinities<sup>[17]</sup> compared to a monovalent binding of sialic acid to HA ( $k_D \sim 2$  mM).<sup>[123]</sup> This is the reason for the effectiveness of multivalent virus binding inhibitors.

First virus-binding inhibitors from the group of Whitesides were based on acrylamide or acrylic acid, which was copolymerized each with sialic acid bearing monomers. Resulting linear polymers achieved molecular weights up to  $M_w = 145$  kDa and possessed pendant sialic acid moieties, which enabled the interaction to HA of IAVs.<sup>[124]</sup> The influence of the inhibitor size were studied after preparation of narrow molecular weight fractions of the inhibitor and revealed that higher molecular weights were more potent in virus inhibition.<sup>[62]</sup> From a polymer point of view natural mucins are linear polymers with densely grafted sugar side chains and can be designated as bottle-brush architecture. Reuter et al. studied different architectures of virus-binding inhibitors that are closer to the architecture of mucins.<sup>[102]</sup> Linear polyethyleneimine (PEI) and dendritic polyamidoamine (PAMAM) were combined to design dendrimers, comb-branched polymers, linear polymers, with dendritic grafting. The study concluded that specific variation of the dendritic polymer architecture enhances the inhibitor efficiency towards viruses. Linear-dendron architectures showed better inhibition compared to spherical dendrimer architectures due to higher flexibility and larger size.<sup>[102]</sup> Though the

mentioned binding inhibitors are very potent in virus inhibition, all of them possess the same disadvantage, namely, low biocompatibility due to positively charged polymer backbones. Excellent biocompatibility is, however, of paramount importance for an application of synthesized virus-binding inhibitors. One attempt is to use polyglycerol as scaffold, which is highly biocompatible<sup>[125-126]</sup> and can be synthesized linear, hyperbranched and as dendritic architecture. Bhatia et al. investigated the virus inhibition behavior of 10 kDa linear polyglycerol (LPG), 10 kDa, and 500 kDa hPG with different degrees of sialylation.<sup>[89]</sup> These inhibitors showed that the inhibition constant was not trivial related to the density of the sialic acids, rather an optimal density existed at which the lowest inhibition constant can be achieved. For 500 kDa LPG an optimal inhibition efficiency was observed at approximately 20% sialylation. Further, Bhatia showed that flexible nanogels (250 nm determined by DLS) as virus binding inhibitors were more efficient than rigid nanogels due to adaption in shape onto the virus surface by multivalent interaction.<sup>[63]</sup> The flexible nanogel (consists of LPG and hPG) and more rigid nanogel (consists of hPG) were prepared by nanoprecipitation.

### **1.5.1 Mucin-inspired virus binding inhibitors**

In order to enhance the virus-binding inhibitor performance, current studies try to mimic mucins since they possess a high virus-binding efficiency. However, the complex structure of mucins and their high molecular weights (MDa range) are difficult to reproduce artificially and reaches the limits of today's used techniques. Therefore, the approach of current research is to synthesize mucin-inspired-binding virus inhibitors by introducing certain features of mucins like functionalization, size, structure, architecture, and shape.

Liu et al. synthesized an alternating copolymer out of methyl vinyl ether and maleic anhydride, which was post-functionalized with pendent sialic acids.<sup>[127]</sup> The resulting mucin-inspired virus-binding inhibitors (up to  $M_w$ : 180 kDa) showed a good cell viability and is able to inhibit different IAV strains. However, this attempt is rather insufficient in case of size, structure, and architecture. A promising mucin-inspired approach is the use of ring-opening metathesis polymerization of norbornene macromonomers with terminal sialyllactose, which results in a brush polymer architecture.<sup>[128]</sup> Using the third generation Grubbs catalyst virus inhibitors with molecular weights up to 684 kDa were reached. Except for the smaller size compared to mucins and the uniform functionalization, most of the mucin features were incorporated in the design of this binding inhibitor. In another study, similar macromonomers without

sialyllactose were polymerized using the same technique resulted in polymers in MDa range with dispersities of 1.01 to 1.07.<sup>[72]</sup> Chen et al. created mucin-inspired bottle-brush architectures using self-assembly of sugar-decorated polymers with lipid tails and single-walled carbon nanotubes (SWNTs).<sup>[129]</sup> The virus inhibition performance was not tested and due to the SWNT the inhibitor tended to sediment.

The last examples focused on secreted mucins as model structures. The following will show briefly some binding inhibitors, which are inspired by membrane-bound mucins. In the first example, lipid-bearing initiators were used to start the polymerization of methyl vinyl ketone leading to one lipid end group. The sugars were introduced afterwards. The lipid end group at the polymer backbone can also be used to anchor the mucin mimetics in cell membranes. With this approach membrane bound mucins can be mimicked. Rabuka et al. incorporated these lipid end-functionalized glycopolymers in supported lipid bilayers (SLB) to create artificial cell membranes with tethered mucin-inspired structures.<sup>[130]</sup> Kramer et al. also decorated cell surfaces with mucin mimetics made by N-carboxyanhydride (NCA) polymerization of N-acetylgalactosamine NCAs.<sup>[116]</sup> Afterwards, these constructs could be linked to site-specific unnatural amino acids in membrane proteins.

A completely different approach was introduced by Cohen et al., where mucin-inspired polymers were anchored with lipid end groups in the viral membrane.<sup>[131]</sup> Due to the lipid anchor the mucin-inspired polymer is kept at the viral membrane and shields the virus in a mucin like in nano environment. The drawback of this innovative method is that the compound was not able to differentiate between viral and cellular membranes.

As shown many attempts were made to synthesize mucin-inspired virus-binding inhibitors. Nevertheless, there was no biocompatible binding inhibitor, which was in the size of natural mucins. Former studies indicated that high molecular weights enhanced the virus binding efficiency.<sup>[62, 102]</sup> Vonnemann et al. indicated that optimal binding inhibition is achieved if the inhibitors were one third of the virus size (e.g.,  $d_{IAV} \sim 100$  nm). As size seems to be an important factor, the development of MDa-sized mucin-inspired binding inhibitors is of high interest.

## **1.6 Analytical methods for testing virus binding**

In order to study viral-binding analytical methods are required. Due to the dynamic binding process and the contribution of multiple-binding interactions the investigation of virus binding and the quantification of the binding strength is challenging. Therefore,



various assays have been developed in the last decades. Common methods for investigation of virus binding are briefly introduced. Distinctions and limitations of the presented methods are in Chapter 1.6.1.

**Hemagglutination inhibition (HAI) assay** – This is the most common method to determine binding inhibition of viruses.<sup>[132]</sup> It is fast, inexpensive, and can be performed with usual lab equipment. Hirst et al. investigated the phenomenon that allantoic fluid from IAV infected chick embryos triggers agglutination of red blood cells.<sup>[133-134]</sup> By the addition of virus binding inhibitors the agglutination can be prevented. The lowest inhibitor concentration, at which no agglutination occurs is defined as (HAI assay-derived) inhibition constant  $k_i$  (Figure 13).<sup>[135]</sup> The impact of the red blood cell species on the binding process is higher due to the expression of different sialic acid receptors and therefore the source e.g., avian, human, horse) has to be stated.<sup>[136]</sup> The reproducibility in different labs can be challenging but Zacour et al. showed that the HAI assay was highly reproducible if the conditions and materials were standardized.<sup>[137]</sup>

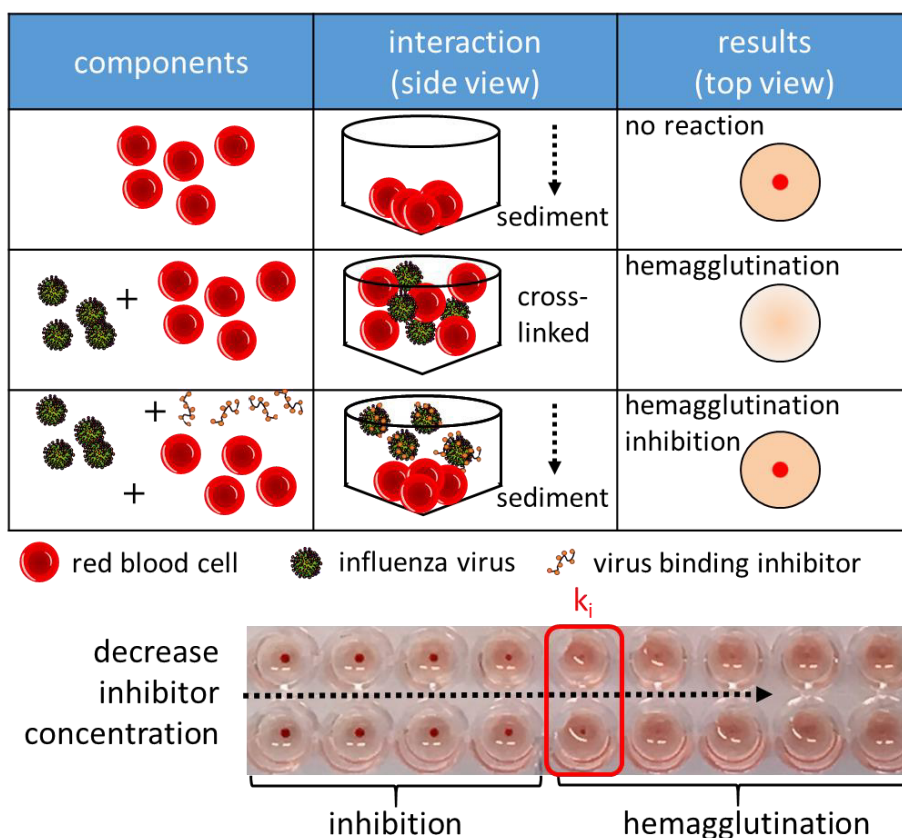


**Figure 13.** The principal function and read out of hemagglutination inhibition (HAI) assay. Sedimentation of red blood cells in V-shaped wells led to a red dot, while no sedimentation was an indicator for IAV crosslinking. IAV-induced crosslinking of red blood cells can be prevented by virus binding inhibitors.

**Glycan micro array** – Glycan micro arrays are a powerful tool for high-throughput investigations of receptor-ligand binding. In one experiment it is possible to probe hundreds of receptors.<sup>[138]</sup> In this technology, many separated small areas are functionalized with the desired receptors. Most linking approaches are covalent (Figure 14), other approaches use biotin streptavidin linking or electrostatic interactions using a poly-L-lysine derivatized surface.<sup>[139]</sup> The read out of the micro array was mostly done by fluorescent emission of the fluorescently labeled probe, e.g., viruses and points out the amount of bound probe. Further it is also possible to investigate each functionalized area by matrix-assisted laser desorption ionization time-of-flight (MALDI -TOF) mass spectrometer after the binding experiment.<sup>[139]</sup> MALDI-TOF enables to measure the mass of receptor-bound probes, which is useful to identify the binding entities.

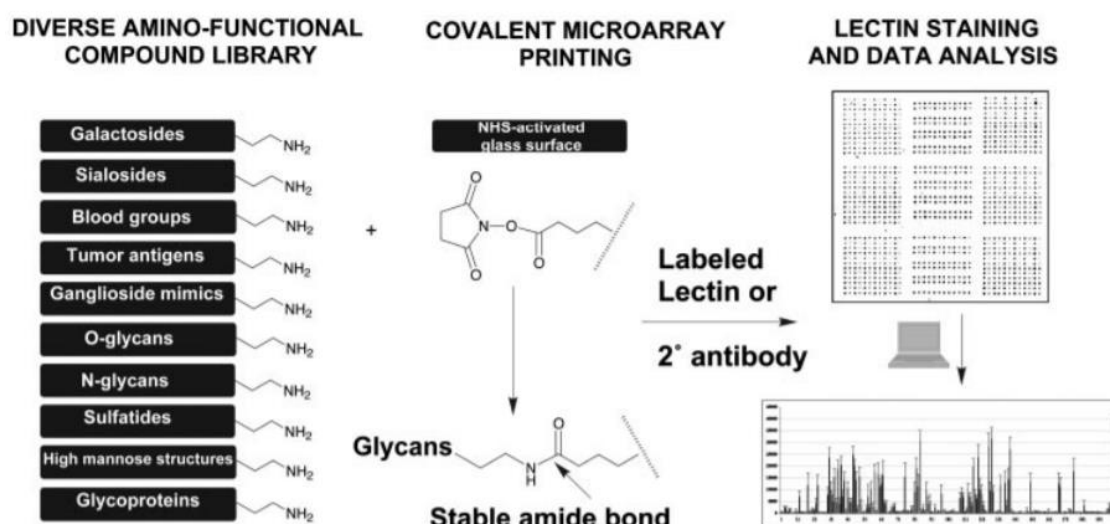


**Figure 14.** Example for covalent tethered glycan receptors onto an amino-reactive microarray surface and read out using image analysis. Reprinted with permission from ref.<sup>[138]</sup>. Copyright (2004) National Academy of Sciences.

Glycan micro arrays are efficient in probing specific interactions for instance the preferential binding of IAVs to glycans with  $\alpha$ -2,3-linked or  $\alpha$ -2,6-linked sialic acids.<sup>[33]</sup> Peng et al. probed different IAV strains and investigated an increased binding to sialoside receptors with elongated branches due to the fact that these are able to bind to two binding pockets of HA simultaneously.<sup>[140]</sup>

The binding of multivalent mucin mimetics to viruses was also investigated in micro arrays. Sialic acid- or sialyllactose-functionalized RAFT polymers were linked via

azide moiety to cyclooctyne-derivatized surfaces to probe multivalent binding to IAVs.<sup>[141-142]</sup>

**Bi-layer interferometry (BLI)** – This label-free, real-time-binding analysis method is used to study dynamic molecular interactions like IAV-receptors binding. Disposable tips of the biosensors possess streptavidin, which can be functionalized with biotinylated receptors.<sup>[143]</sup> White light in the inner tip is reflected at the surface inside the tip (non-functionalized, used as reference) and outside of the tip (functionalized surface, here binding occurs). Binding events to the functionalized surface triggers an increase in optical thickness, which can be detected as wavelength shift compared to the reference surface (Figure 15).<sup>[144]</sup> Non-bound entities in the solution do not influence the optical thickness. Hence, this method can be in principal applied in crude samples.<sup>[144]</sup> The dip-and-read capability of BLI makes this method easy to handle.<sup>[143]</sup> Nevertheless, the resulting wavelength shift does not correspond to a certain property of the bilayers rather depends on various non-trivial properties. Therefore, the interpretation of the wavelength shift can be difficult.

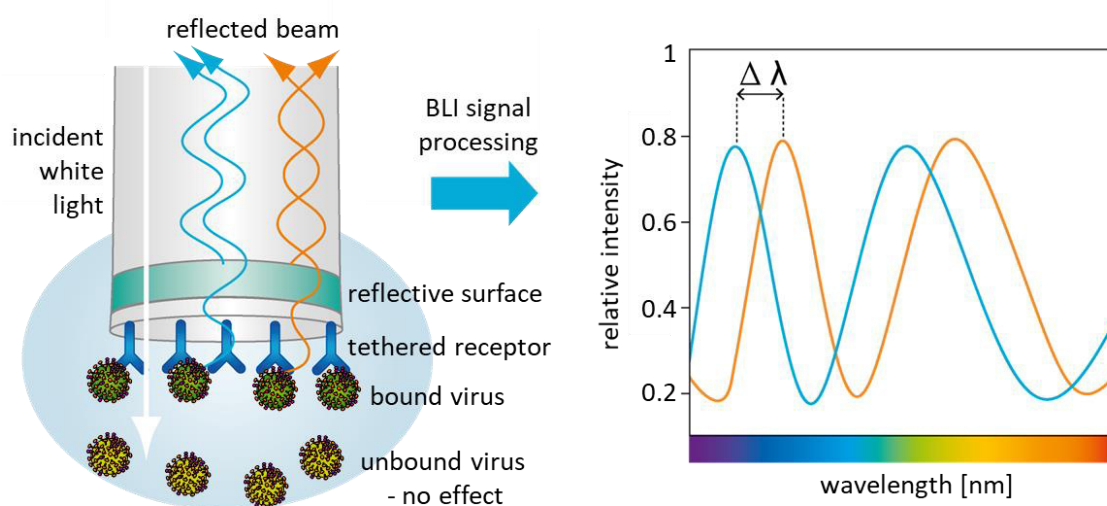


**Figure 15.** Influenza A virus (IAV)-binding measurements using bi-layer interferometer (BLI) with receptor functionalized tip. Binding objects increase the optical thickness, which can be determined by a shift of the wave length. Modified with permission from ref.<sup>[145]</sup>. Copyright 2020 Sartorius AG.

Benton et al. performed BLI measurements of IAVs to receptor analogs containing  $\alpha$ -2,3-linked or  $\alpha$ -2,6-linked sialic acids in absence and presence of NA inhibitor.<sup>[146]</sup> Blocking of the NA enzymatic cleavage led to increased binding. Without NA inhibitor the IAVs cleave sialic acid moieties, which decrease the relative binding to really low relative binding (15 to 0%).<sup>[146]</sup> Researchers claim that the comparison of the relative binding of IAV in absence and presence information about the HA/NA balance could be derived.<sup>[146-147]</sup> However, the fact that it is not possible to use the BLI setup without a NA inhibitor due to the cleavage of sialic acid at the tip, the natural HA/NA balance is drastically interfered and cannot be determined with this setup.

**Atomic force microscopy (AFM)** – AFM is a method, which measures directly the force of the interaction between a tip and a probed target. The tip is placed on the end of a cantilever. A piezoelectric device oscillates the cantilever, which results in a up and down movement of the tip.<sup>[148]</sup> The oscillation distance can be measured accurately by a laser beam, which is reflected on the back of the cantilever and detected by a detector. When the approaching tip gets in contact with the sample the cantilever bends and tip-sample force can be inferred from a measurement of the cantilever's deflection.<sup>[148]</sup> With this information force-distance curves can be recorded.

To probe specific binding interactions, the tip can be functionalized or biological binders can be covalently attached.<sup>[148]</sup> In order to test virus binding, various viruses were attached to the tip.<sup>[149-151]</sup> By approaching and withdrawing the anchored viruses to cell membranes, the binding force of single-binding events can be investigated (Figure 16). From the recorded data attachment-rates, detachment-rates, and the equilibrium binding constant of the interaction can be derived.<sup>[149]</sup> The resulting kinetics corresponds to the unbinding of a non-equilibrium state because the binding and rupture are forced by the cantilever movement. This is important to mention because the kinetics can deviate from the kinetics in equilibrium state. AFM measurements with anchored viruses observed multivalent binding modes to cell membranes. Furthermore, the binding valency was quantified due to the fact that multiple interactions resulted in higher binding forces than single interactions.<sup>[151]</sup> Sieben et al. probed the binding of anchored IAVs to cell membranes and showed a highly dynamic interaction between HA and the cell surface receptors.<sup>[150]</sup>

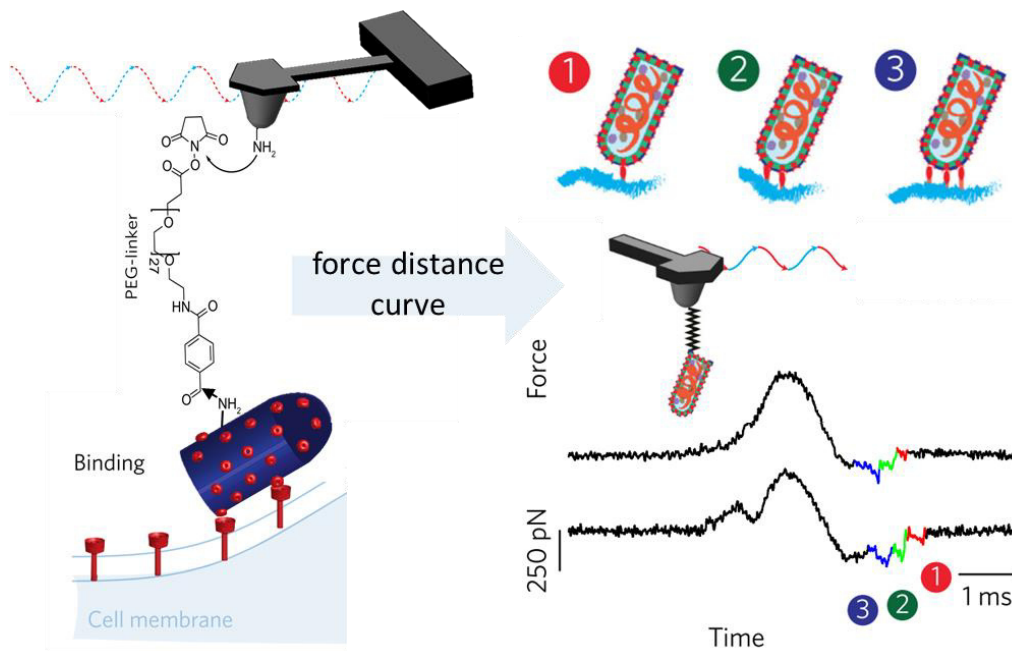


**Figure 16.** Atomic force microscopy measurement with anchored virus on the tip to investigate the interaction to cell surface receptors (left). From the resulting force distance curves, the binding valency can be quantified (right). Adapted with permission from ref.<sup>[151]</sup>. Copyright 2016, Springer Nature.

AFM can also be applied to investigate the binding strength of binding inhibitors. Scherer et al. and Cuellar-Camacho et al. functionalized the tip with sialylated architectures and probed the binding to immobilized IAVs at the surface.<sup>[152-153]</sup> Further, they probed assembled HA and NA monomers individually on a surface and found much stronger binding strength to NA compared to HA.<sup>[152-153]</sup> This shows the potency of the AFM method in probing specific binding processes. However, the obtained information results from non-equilibrium and does not reflect the properties of naturally occurring binding processes, which are in equilibrium. Furthermore, individual binding events are observed, which has to be repeated multiple times to achieve good statistics.

**Total internal reflection fluorescence (TIRF) microscopy** – TIRF microscopy is an optical technique to visualize objects at the interface and was invented by Ambrose in 1956.<sup>[154]</sup> An incident light hits the interface of a glass slide and aqueous sample with an angle greater than the critical angle and gets totally reflected. The total reflection generates an evanescent wave and penetrates ~ 100 nm inside the aqueous sample. Within this depth fluorescently labeled molecules or viruses get excited and can be visualized due to emission of fluorescence. To ensure specific binding the glass slide is functionalized with receptors. The binding of single viruses to the surface can be

visualized. Viruses above the evanescent beam (non-binding viruses) are not visible due to lack of excitation (Figure 17). TIRF microscopy enables direct visualization of single binding viruses and does not rely on indirect parameters like shift in wavelength in BLI, which makes the interpretation of TIRF microscopy measurements more straightforward. A high number of binding events can be observed in parallel, which generates a good statistic for binding and release studies. In contrast to the BLI method, the addition of NA inhibitor to prevent cleavage of sialic acids is not necessary because the used virus concentration in TIRF measurements is much lower and the receptor concentration change due to cleaved sialic acids at the surface can be neglected. This is a great advantage because NA also contributes to the binding. The natural binding process of IAV cannot be investigated if one membrane binding protein is artificially blocked.

Recently researchers coated glass slides with SLBs to mimic plasma membranes in TIRF microscopy. Incorporated receptors within the SLB, e.g., natural or synthetic lipid receptors are still mobile in 2D like in natural cell membrane.<sup>[155-157]</sup> Investigation of receptor clustering effects due to the virus binding or due to cholesterol in the SLB, which enhances the binding avidity of the virus, can be studied with SLB-coated surfaces.<sup>[158]</sup>

Recent studies using TIRF microscopy in combination with SLBs investigated binding strength with different binding systems. Wahlsten et al. probed cell membrane-derived vesicles and their interaction with immobilized chemokines.<sup>[159]</sup> Bally et al. investigated immobilized virus like particles on a SLB, which interact with fluorescently labeled vesicles containing glycosphingolipids.<sup>[160]</sup> Lee et al. tested IAV binding to natural lipid receptors in SLBs.<sup>[161]</sup> These research topics show the current status of the research using TIRF microscopy for measuring the binding strength of ligand-receptor interactions. All have in common that they are able to investigate the attachment-rate and probe survival probabilities. Nevertheless, they were not able to derive the detachment rate out of the survival probabilities because the detachment rates depend on the binding valency, which is not known. However, it was possible to determine the binding valency from the diffusion coefficient of bound liposomes to the SLB using TIRF microscopy.<sup>[162]</sup> Nevertheless, this was just a model system and has not been applied to viruses yet.

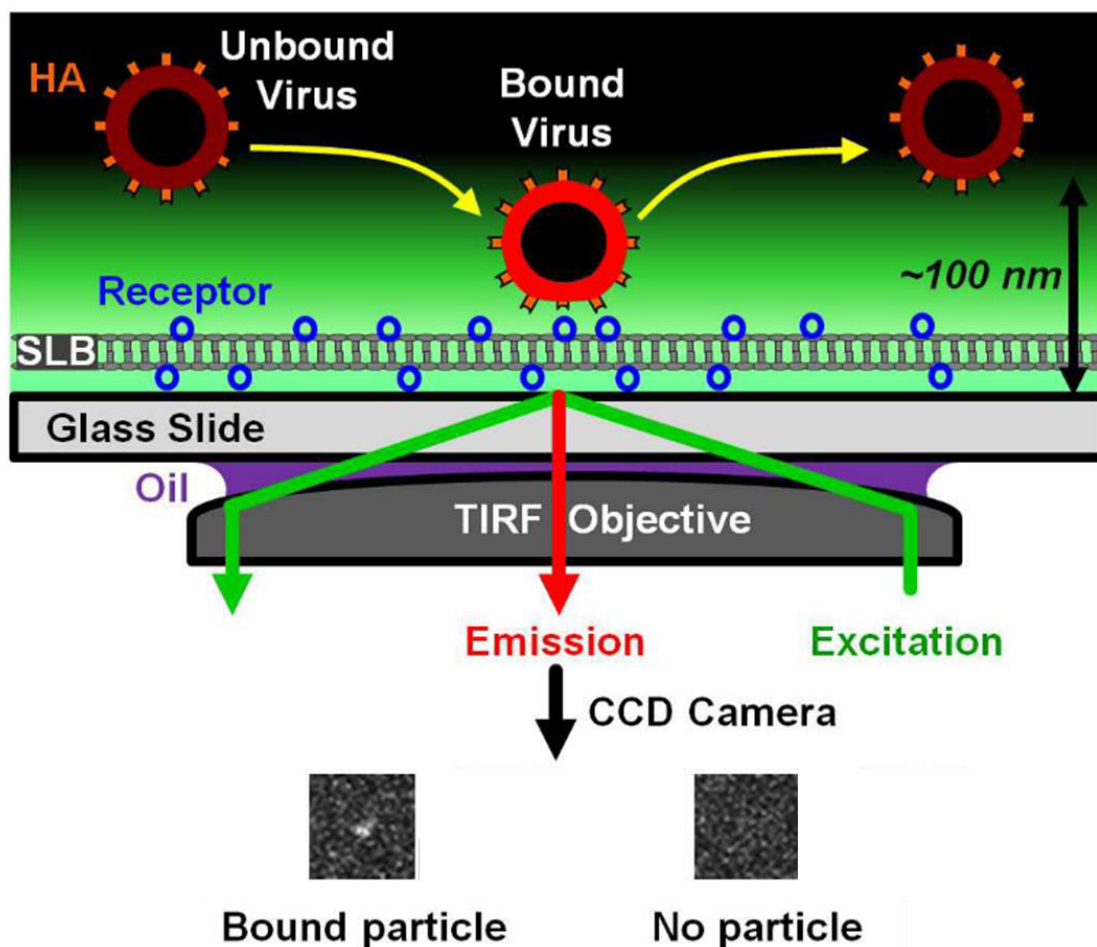


**Figure 17.** Characterization of binding interactions between labeled influenza A viruses (IAVs) and sialic acid receptors using total internal reflection microscopy. Bound fluorescently labeled IAVs at the supported lipid bilayer are excited in the evanescent wave (penetration  $\sim 100$  nm), while non-bound IAVs are not visible due to lack of excitation. Single binding viruses are indicated by a local increase of fluorescent intensity. Besides the number of newly arriving viruses (attachment-rate) and the survival probability, the diffusion of bound viruses at the SLB can be extracted. The residence time can be determined from the length of the virus trajectories but cannot be used to derive the detachment rate for multivalent interactions as the valency distribution is not known. Modified with permission from ref.<sup>[161]</sup>. Copyright 2016 Lee et al. PLoS ONE.

### 1.6.1 Distinctions and limitations of the methods

The described methods can be distinct due to various properties and limitations. For example, methods like HAI assay and glycan micro array are endpoint assay, which provide more or less just a binary read out like binding yes/no. BLI, TIRF, and AFM methods are able to observe dynamic binding processes, which is important due the fact that in nature most binding events are dynamic. Furthermore, TIRF microscopy and AFM are able to investigate single virus binding, which is crucial if certain information like binding valency are wanted. The output of HAI assays, Glycan micro arrays and BLI

corresponds to an average value taken from the entire ensemble, thereby averaging out individual features hidden in single events. All described methods operate under equilibrium conditions, except AFM measurements, due to the applied force no natural binding equilibrium can be adjusted. Additionally, the receptors or targeted glycan structure differ within the methods. Complex structures, for example, the red blood cell receptors in the HAI assay and the cell surfaces are also often used for AFM or glycan micro arrays. These structures are not well defined but are naturally occurring. Well-defined receptors or glycan structures can be investigated with glycan micro arrays, BLI, TIRF, and AFM. Furthermore, direct parameters are observed or measured like single virus motion in TIRF microscopy or the binding force in AFM measurements. The other methods rely on indirect parameter like sedimentation in HAI assay, like the wavelength shift in BLI or the fluorescence intensity in glycan micro arrays.

The overview showed how important the choice of the right method is to investigate the desired effects. Also, the limitations of each method are stated, which is the major driving force for the development of new biophysical methods for the investigation of virus binding.



## 2 Scientific goals

The problem of current antiviral drugs is that these highly specific small molecules are delicate against small mutational changes of the virus (e.g., antigenic drift or antigenic shift), which may reduce the efficiency of these drugs or even resistance against them. The aim of this work is the development and assessment of mucin-inspired virus binding inhibitors, which target viral proteins. The design is inspired by natural mucins, which creates a very efficient barrier against various viruses. The key player in mucus is mucin, huge (MDa range) glycoproteins. The high molecular weight of mucins and previous studies suggest that size is an important factor for efficient virus-binding inhibitors.<sup>[62, 102, 124]</sup> Vonnemann et al. showed that the optimal size of binding inhibitors for spherical viruses is one third of the virus size.<sup>[163]</sup> Therefore the size relation of the used polymer scaffold to the inhibition efficiency can be probed by the synthesis of different molecular weights of hyperbranched polyglycerol.

One aim of this thesis is to investigate the influence of the synthesized mucin-inspired-binding inhibitors on the virus-receptor interaction. Since established methods are not able to determine changes of the virus-receptor interaction under equilibrium conditions, a new analytical method has to be developed. TIRF microscopy can, in principle, be used to build up such an analytical tool for the investigation of virus interactions. For this purpose, SLBs can be used as artificial cell membrane as target for virus binding. Inhibitors are able to interfere these interactions, which should result in a reduced number of binding viruses (attachment rate). Further, diffusion measurements of SLB-bound viruses should allow for deriving the binding valency of virus-receptor interactions at the membrane. The addition of inhibitors should not only influence the attachment rate rather induce a change in valency of the binding. This knowledge would lead to deeper understanding in the mode of action of binding inhibitors.

Due to the high biocompatibility of hyperbranched polyglycerol this polymer is not only a promising candidate for the development of virus-binding inhibitors but also used in tissue engineering, as drug carrier or used against chronic infections.<sup>[164]</sup> All these applications are in the biomedical field and require a use of harmless substances, which involves avoiding residues like toxic solvents. Hence, a solvent-free method is desirable to avoid the possibility of residual solvents. The challenge is to achieve the same or better quality compared to the conventional polymerization of hPG, which involves solvents like tetrahydrofuran (THF) and N-Methyl-2-pyrrolidon (NMP).<sup>[82]</sup> Further, the use of an automated system can be used to increase the reproducibility. The reproducibility and the

maximal batch size of the developed automated solvent-free polymerization has to be verified as well as the resulting hPG properties.

To conclude, the following scientific goals and hypothesis will be addressed in this thesis: (i) hPGs can be synthesized with high size reproducibility in absence of typical solvents (THF and NMP) by automatization of the polymerization process, (ii) the inhibition efficiency of hPG-based IAV binding inhibitors increases as the inhibitor size approaches the size of IAVs (as suggested by Vonnemann et al.). (iii) TIRF allows for determining valency distributions by measurement of the diffusion coefficients of receptor-bound IAVs and thus provides information about the IAV attachment rate, valency, and valency-dependent detachment rate distributions and how these properties are modified upon addition of virus inhibitors.

These hypotheses were addressed in three projects. In the first project the TIRF microscopy-based assay was developed and verified with probing the influence of a monomeric inhibitor (zanamivir) on the virus-receptor interaction of a typical respiratory virus (IAV). In the second project an automated solvent-free method for the synthesis of hPG was established. Online monitoring of the torque value during the polymerization was used to determine indirectly the molecular weight of the polymer in the reactor. The objective of project three was the synthesis of a MDa-sized mucin-inspired virus binding inhibitors and the characterization of their inhibition efficiency against IAVs. In order to check the size impact on the inhibition efficiency, molecular weights bridging of two to three order of magnitudes (10 to 2600 kDa) were synthesized. Hence, reaching the MDa-size range of mucins and hitting the optimal binding inhibitor size for IAVs ( $d_{IAV} \sim 100$  nm;  $d_{hPG2600\text{ kDa}} \sim 30$  nm). All hPGs were functionalized with sialic acid and sulfate groups to ensure binding to IAVs.

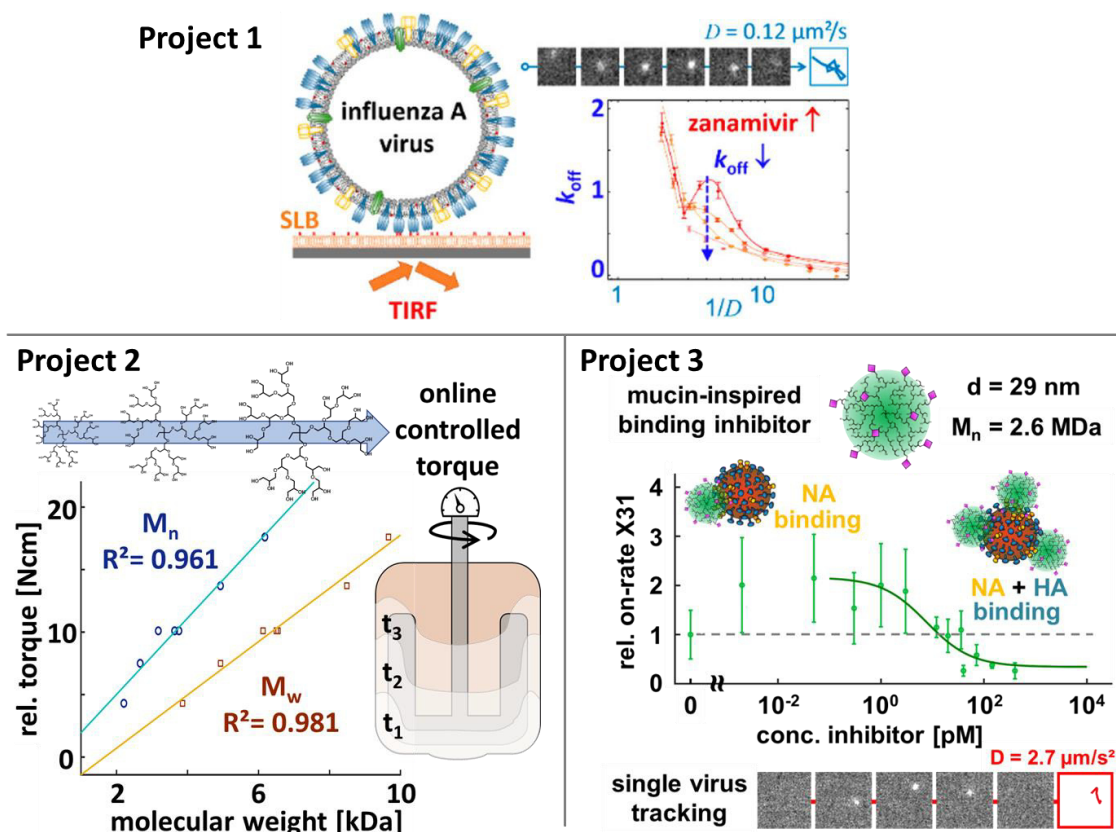


**Figure 18.** Project overview: 1.) IAV binding processes were investigated with an assay using total internal reflection fluorescence (TIRF) microscopy. Using this assay, the binding valency of IAVs could be investigated. 2.) development of an automated solvent-free polymerization of hyperbranched polyglycerol (hPG). Reproducible production of tailored hPG molecular weights by torque value online monitoring. 3.) mucin-inspired binding inhibitors were synthesized. The characterization of the IAV inhibition with TIRF microscopy revealed a biphasic binding behavior. Reprinted with permission from ref. <sup>[165-166]</sup>. Copyright 2019 American Chemical Society. Copyright 2020 Wiley-VCH GmbH.

### 3 Publications

In this chapter all published articles and submitted manuscripts are listed and the contribution of the authors are stated.

#### 3.1 Mobility-Based Quantification of Multivalent Virus-Receptor Interactions: New Insights Into Influenza A Virus Binding Mode

Matthias Müller, Daniel Lauster, Helen H. K. Wildenauer, Andreas Herrmann, Stephan Block, *Nano Letters* **2019**, 19 (3), 1875-1882.

<https://doi.org/10.1021/acs.nanolett.8b04969>

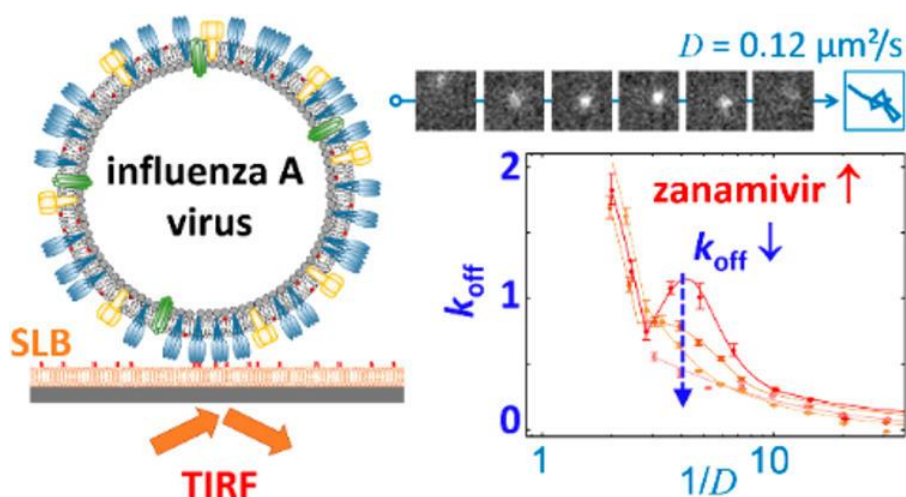


**Figure 19.** TIRF microscopy is used to visualize binding influenza A viruses to receptors in a supported lipid bilayer. Diffusion-derived detachment-rates ( $k_{\text{off}}$ ) are used to unravel the average binding valency ( $1/D$ ). This novel method disclosed an elevated detachment-rate peak, which could be dose dependently decreased with the addition of the neuraminidase inhibitor zanamivir. Reprinted with permission from ref.<sup>[165]</sup>. Copyright 2019 American Chemical Society.

**Author's contribution:** Matthias Wallert (née Müller) performed all experiments, analyzed part of the experimental data, and wrote the manuscript. Daniel Lauster grew and provided IAV viruses. Helen H. K. Wildenauer contributed to TIRF measurements. Andreas Herrmann provided scientific support and contributed to the interpretation of the measurements. Stephan Block supervised the project, designed the method, did deeper analyses of the measurement data, and edited the manuscript.

### 3.2 Automated solvent-free polymerization of hyperbranched polyglycerol with tailored molecular weight by online torque detection

Matthias Wallert, Johann Plaschke, Mathias Dimde, Vahid Ahmadi, Stephan Block, Rainer Haag, *submitted to Macromolecular Materials and Engineering*

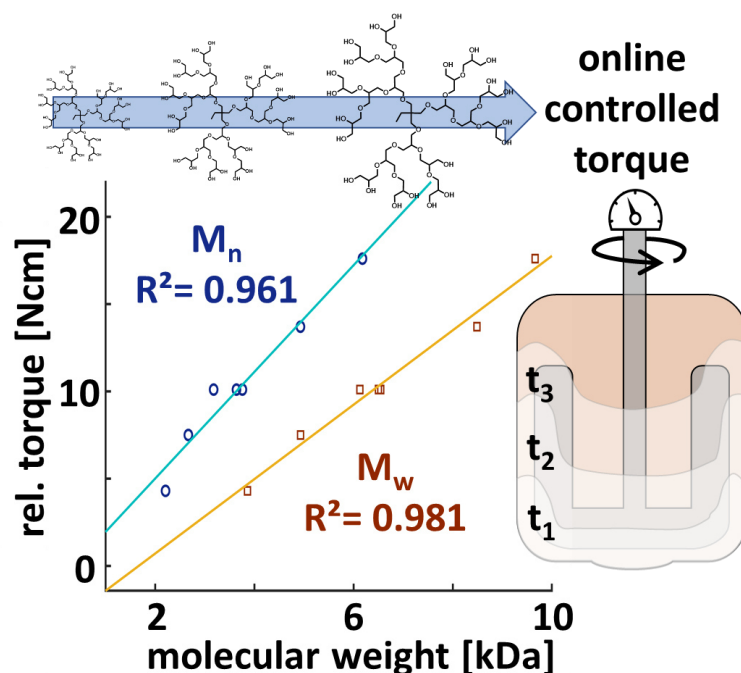


**Figure 20.** Online torque measurements are used to establish an automated method to tailor the molecular weight during the solvent-free polymerization of hyperbranched glycerol.

**Author's contribution:** Matthias Wallert established the method, purified reactants, performed polymerizations, analyzed the data, and wrote manuscript, Johann Plaschke contributed to the polymerization and distillation of glycidol, Mathias Dimde edited the manuscript, supported the reactor work. Vahid Ahmadi recorded all MALDI-TOF measurements. Stephan Block and Rainer Haag provided scientific guidance and proofread the manuscript.

# Automated Solvent-Free Polymerization of Hyperbranched Polyglycerol with Tailored Molecular Weight by Online Torque Detection

Matthias Wallert,<sup>1</sup> Johann Plaschke,<sup>1</sup> Mathias Dimde,<sup>2</sup> Vahid Ahmadi,<sup>2</sup> Stephan Block,<sup>1,\*</sup>  
Rainer Haag<sup>2,\*</sup>

<sup>1</sup>Institute of Chemistry and Biochemistry, Emmy-Noether Group "Bionanointerfaces", Freie Universität Berlin, Arnimallee 22, 14195 Berlin, Germany

<sup>2</sup>Institute of Chemistry and Biochemistry, Macromolecular Chemistry, Freie Universität Berlin, Takustr. 3, 14195 Berlin, Germany

\* Corresponding authors

Rainer Haag, e-mail: haag@zedat.fu-berlin.de

Stephan Block, e-mail: stephan.block@fu-berlin.de

Keywords: Solvent-free, hyperbranched polyglycerols, torque-controlled, automated reactor, online monitoring

## Abstract

Polymerization processes with high reproducibility, traceability and non-toxic compounds are required for biomedical applications. Here an automated solvent-free polymerization of hyperbranched polyglycerol in multiple hundred-gram scale is established. Performed was an anionic ring-opening multibranching (ROMB) polymerization with slow addition of glycidol. The solvent-free approach avoids commonly used toxic solvents during the polymerization and work-up. Due to the automation of the polymerization process a high reproducibility and traceability is accomplished. The used reactor is equipped with an anchor stirrer and stirrer control, which measures the applied torque. A linear correlation of the increasing torque and the degree of polymerization is observed, which can be used to monitor the molecular weight *in situ* during the polymerization. This convenient monitoring can be applied in all reactors with torque detection and fills the gap of online monitoring methods for the molecular weight in bulk polymerizations.

## Introduction

Several studies on polyglycerol (PG) have been investigated within the last two decades with the aim to establish the biocompatible, non-cytotoxic, and water-soluble polymers as an alternative to polymers being approved for therapeutics and diagnostics, such as polyethylene glycol (PEG) and poly (vinyl alcohol) PVA.<sup>[1]</sup> Various synthetic processes of PG have been established in the last couple of years, which have an influence on the polymeric scaffold, its architecture, size, and functionality. All of them, however, require partially toxic solvents such as N,N-dimethylformamide (DMF), N-methyl-2-pyrrolidone (NMP) during polymerization or work-up.

The production and functionalization of hyperbranched polyglycerols (hPGs) have been well established. Anionic ring-opening multibranching (ROMB) polymerization of glycidol is the most frequent method for the preparation of hPG. The deprotonated initiator 1,1,1-trimethylpropane (TMP) enables in combination with a slow monomer addition and a rapid cation exchange equilibrium a good control over the molecular weight, polydispersity index (PDI) as well as the multibranching structure of the hPG.<sup>[2-3]</sup>

Recently, Kizhakkedathu and coworkers developed a two-step polymerization of glycidol to extend the maximum of the molecular weight of hPG up to 9 MDa. Here, a macroinitiator approach in combination with solvent-based ROMB polymerization is used to achieve mega hyperbranched polyglycerols (mega hPGs).<sup>[5]</sup> The type of the used solvent during the polymerization has a major impact on the resulting polymer properties.<sup>[6]</sup> Most approaches are performed in batch processes, however, the hPG synthesis is also studied in a continuous flow microreactor.<sup>[4]</sup>

Furthermore, linear polyglycerol (IPG) can be produced using an acetal-protected glycidol derivate as monomer. Ethoxyethyl glycidyl ether (EEGE) was polymerized and the protective groups were removed by acidic hydrolysis after polymerization, resulting in linear polyglycerols. The linear conjugates are as useful for many biomedical applications.<sup>[7-8]</sup>

Besides variations in architecture and size, the production of biodegradable PGs is of interest. A cationic polymerization of glycidol by citric acid at ambient and solvent-free conditions was established to produce degradable polyglycerol units with a molecular weight of 1-2 kDa in a green chemistry approach.<sup>[9]</sup> Furthermore, one-pot synthesis strategies for biodegradable co-polymers based on polyglycerol and poly caprolactone, polysuccinic acid, or polylactide were developed and tested for biological applications.<sup>[10-13]</sup> These modifications

and variations offer a toolbox of various PG versions for the development of more complex architectures, which are relevant for the transportation and release of active compounds in biomedical applications. Here, stimuli-sensitive groups or cleaving points can be incorporated to degrade the polymer backbone or more complex architectures like PG based: micelles, hydrogels, nano capsules; or core-shell structures, in a controlled way and transport and release the encapsulated therapeutic cargo at the target site.<sup>[14-18]</sup> Furthermore, PG was used as multivalent scaffold for applications like virus binding inhibition<sup>[19-20]</sup> and anti-inflammatory therapy.<sup>[21]</sup> In the cosmetic industry PG is also applied as ingredient or used as precursor for surfactants and emulsifiers.<sup>[22]</sup>

For polymers that are used in the field of biomedicine it is important to develop a product with defined parameters and to have good control over reaction parameters and kinetics. Earlier works by Frey et al. had the goal to study these processes with mechanistic detail.<sup>[2-3, 23]</sup> Laboratory and industrial polymerization processes benefit of online monitoring due to safety aspects for exothermic reactions as well as for providing information on polymer composition and quality.<sup>[24-26]</sup> Various online production methods are still in development to realize a key point of the “Industry 4.0” concept by combining manufacturing processes with networks of machines, products and people driven by software, sensors, and artificial intelligence.<sup>[27]</sup>

Paulus et al. developed a computational software model of the hPG polymerization to describe and control the experimental parameter dependencies.<sup>[28]</sup> However, organic solvents for the polymerization process and/or purification of the crude product were used for all above-mentioned production processes of polyglycerol. Besides automatization and digitalization, sustainability aspects play a crucial role in today’s society. The reduction of organic solvents and the moving away from petrochemical compounds to renewable natural resources increases in the chemical sector and in the field of biopolymers.<sup>[29-31]</sup>

Here, we introduce an automated solvent-free-polymerization of highly biocompatible hPG, which combines and meets the mentioned requirements for a modern polymerization via online control over the reaction parameters and a solvent-free green chemistry approach to produce tailor made polymers in a reproducible manner.



## Results and Discussion

Online monitoring of polymerization parameters is of high interest because it enables to run the process in a safe condition, minimizes production cost by controlling the reaction, provides efficient control of constant quality without batch-to-batch variation, and gives information about the reaction progress within the reactor.<sup>[25]</sup> Important for its useful application is the practicability of the monitoring system. Here a conventional anchor stirrer is used to monitor the torque development during a solvent-free anionic polymerization of hPG. The hypothesis in this study is that monitoring of the torque increase during the polymerization provides information about the actual molecular weight of the polymer in the reactor. To test this hypothesis the polymerization is performed to several torque values. Afterwards, the molecular weight of the resulting polymers is determined. The investigation of the correlation between torque and molecular weight is addressed in this study.

The model system is an anionic ring-opening polymerization of glycidol. TMP is used as a trifunctional starter and is partially deprotonated (~10 % of the OH groups) in a methanolic potassium hydroxide solution. Afterwards, methanol is evaporated under reduced pressure before the solvent-free polymerization starts with slow monomer addition of glycidol (18 g/h). The resulting polymer is a hyperbranched polyglycerol (**Figure 1**).

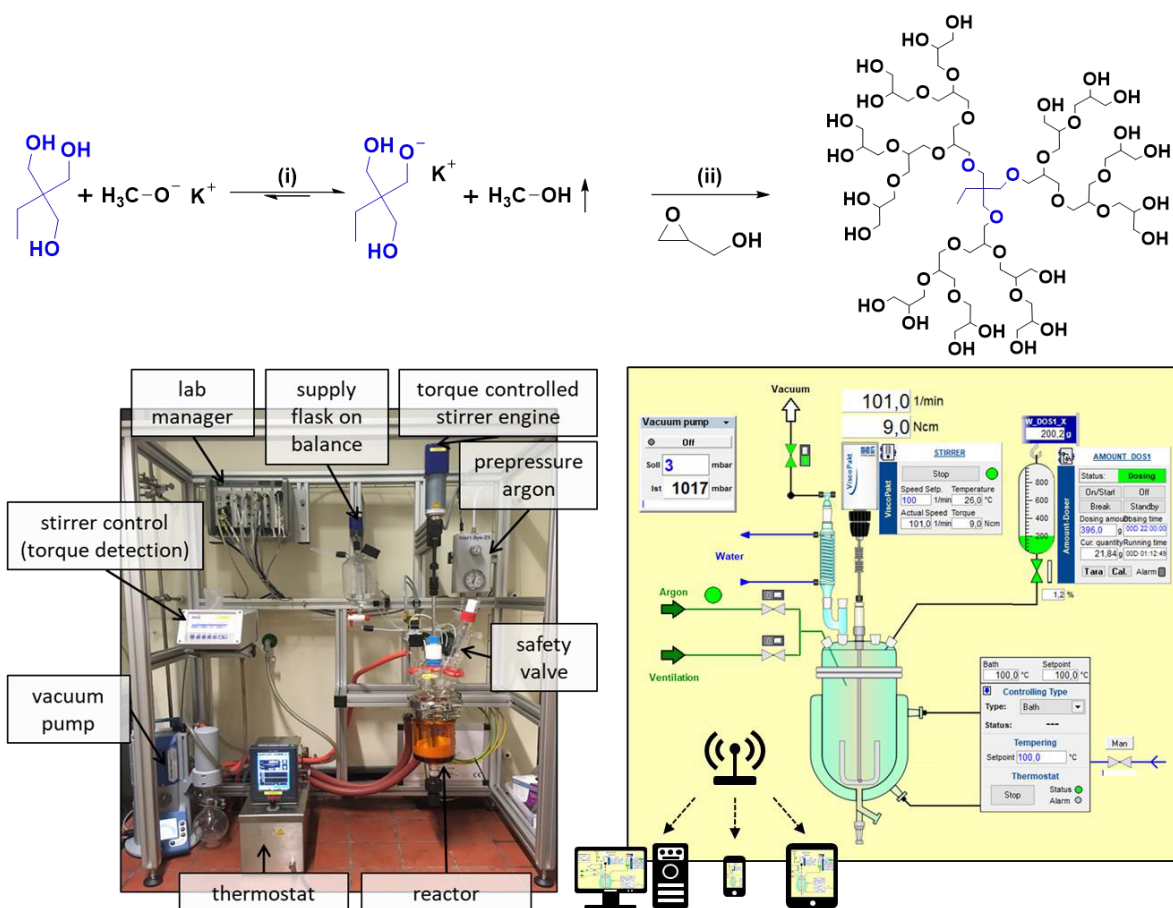


**Figure 1.** Solvent-free polymerization of glycidol in an automated reactor system (LabKit™ HiTec Zang, Herzogenrath, Germany). (i) Partial deprotonation (10 % OH) of the starter TMP with potassium methoxide for 1 h at 55 °C and subsequent evaporation of methanol by slowly decreasing pressure to 3 mbar. (ii) Polymerization of glycidol at 100 °C with slow monomer addition rate 18 g/h. The automatized reactor system is controlled by a computer and process data like temperature, pressure, torque, etc., is recorded. Magnetic valves control the addition of monomer or the flow of argon. All controlled parameters are shown live in the software of HiTec Zang. The system is accessible via an App and enables a wireless remote control using a tablet or mobile phone.

The polymerization is carried out in an automated reactor system to ensure the same process work flow for each experiment, which is essential for the reproducibility. The temperature is controlled via a water-cooling and -heating thermostat (CC-205C with Pilot ONE controller, Huber, Offenburg, Germany) that is pumping oil through the double wall of the reactor. The pressure is controlled via a vacuum membrane pump (PC 3001 Vario pro,

Vacuubrand, Wertheim, Germany). The reactor is additionally equipped with an argon inlet to create an inert atmosphere, which is required for anionic polymerizations to avoid spontaneous termination due to oxygen or water.<sup>[32]</sup> Monomer addition is realized via a supply flask hanging on a load cell (IL-GRADO1000, HiTec Zang, Herzogenrath, Germany). The high accuracy of the dosing can be shown by comparison of the added amount of glycerol per minute, which results in a mean of  $0.30 \text{ g min}^{-1}$  with a standard deviation of  $0.02 \text{ g min}^{-1}$ . The rotation speed of the anchor stirrer is controlled (ViscoPakt®-rheo-27, HiTec Zang, Herzogenrath, Germany) and the applied force (torque) that is needed to achieve a user-set rotation speed is determined. All mentioned parts are connected to the LabManager® (HiTec Zang, Herzogenrath, Germany). Here the commands arrive from a computer and are further translated to actions like open/closing magnetic valves, heating/cooling, adjusting the pressure, or keeping a certain rotation speed. The lab manager collects also all measured parameters like temperature, stirrer speed, torque, and pressure, etc. during the polymerization. Recorded parameter can be observed in time or afterwards. Our focus is on the torque development during polymerization (blue line, **Figure 2a**). The torque value increases as expected with the steady addition of glycidol ( $18 \text{ g h}^{-1}$ ), while all other parameters are kept constant. 2.5 h after the start of the polymerization process a steeper rise of the torque value occurs, which is flattened to the initial ascending slope after additional 2.5 h. An explanation could be adhesion of the polymer on the reactor wall. In the beginning just the bottom of the reactor is covered, after a certain time the increasing polymer mass starts to climb the reactor wall, which is supported by the movement of the anchor stirrer. The steeper rise of the torque value results probably from the higher contact area of the polymer to the reactor wall. At a certain polymer amount, the polymer mass is not able to climb higher and flows to the center of the reactor. In the center the anchor stirrer blades have a smaller contact area, which leads to relative lower required force to stir and the torque increase is mostly due to increasing mass and rises in a linear fashion.

The steeper rise of the torque value is investigated for all polymerizations with fresh distilled glycidol, whereas, at polymerizations with non-distilled glycidol or older distilled glycidol batches, this steeper rise does not appear. Most probably the water residue within the polymer mass decreases its viscosity and hinders it to climb the reactor wall. This hypothesis is supported by the lower measured torque values compared to polymerization

with freshly distilled glycidol. The explanation concludes that the torque trend would change with different reactor or stirrer geometry.

After the addition of monomer is stopped, the reaction condition is kept constant for at least 2 h. During this time the torque value stagnates or shows an increase probably due to the reaction of remaining monomer, which acts as a solvent, until all monomer is consumed. The resulting polymer mass in the reactor appears as highly viscous white mixture. The white color results from dispersed gas bubbles within the viscous polymer mass. The polymerization is quenched by the addition of water and leads to a drastic decrease of the torque value. The torque value after quenching is comparable with the torque value before the polymerization. After the addition of water, the polymer is dissolved and due to the lower viscosity, the trapped gas bubbles are able to escape, which lead to a slightly golden transparent polymer solution.

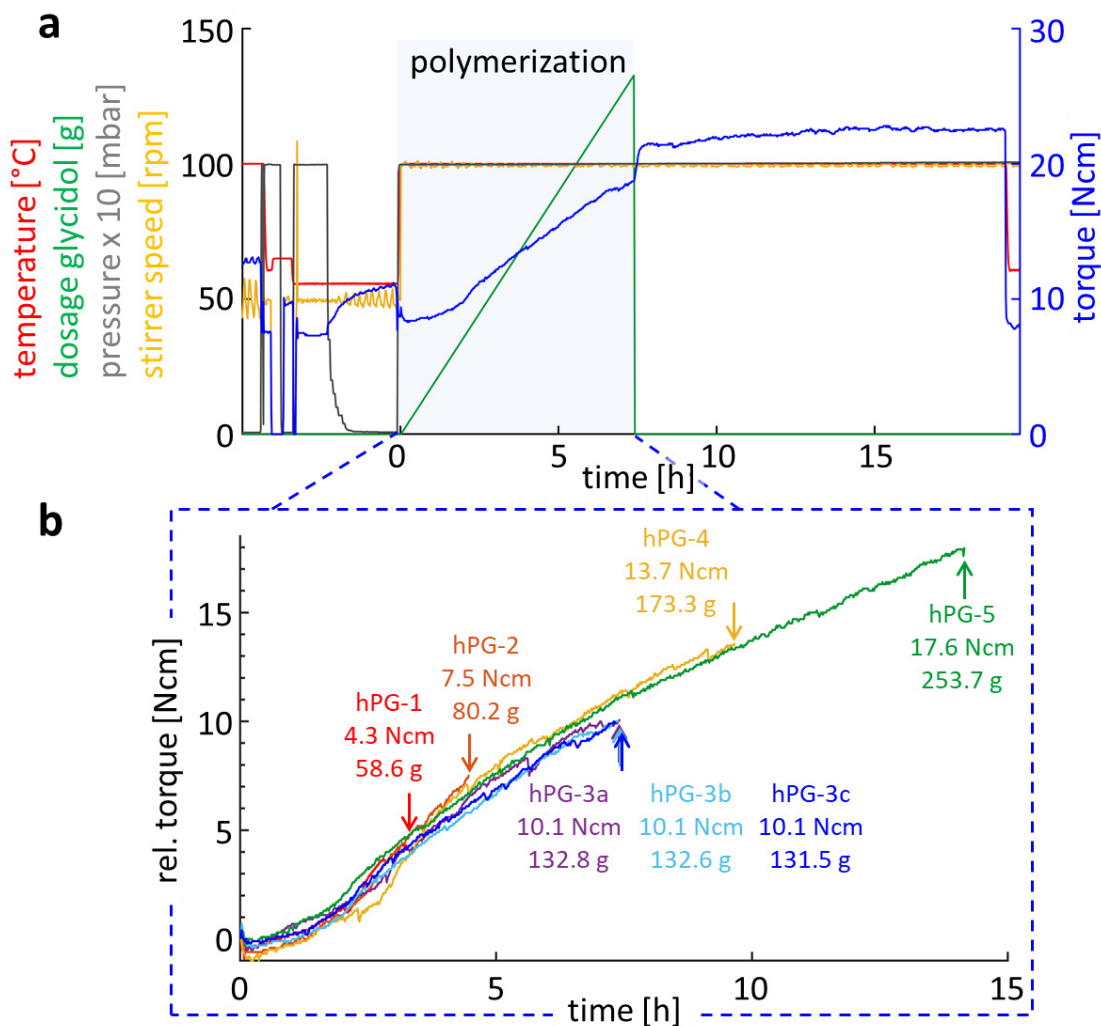


**Figure 2.** (a) Recorded parameter during polymerization of hPG until the terminal torque of 21 Ncm (correspond to 10.1 Ncm relative torque; hPG-3a). (b) Comparison of the relative torque development from all polymerizations with different terminal torque values. The relative torque value of 10.1 Ncm was performed three times to investigate the reproducibility.

Seven individual polymerizations are performed to predefined terminal torques. The absolute targeted torque values are between 15 and 27 Ncm. This range is chosen because the empty system itself needs already ~10 Ncm for stirring and the engine of the stirrer is limited to 28 Ncm. The used stirrer seal out of PTFE closes tight to ensure a good vacuum but causes high friction and therefore high torque values are needed to stir in empty state. This disadvantage could be overcome by using a magnetic stirrer seal in the future.

The starting point of the absolute torque values for each polymerization varies. For the seven polymerizations, the mean starting torque value and the standard deviation is  $11.4 \pm 1.3$  Ncm. To overcome this problem the relative torque increase is compared, which reveals same torque developments for each batch. The same development of the relative torque indicates a reproducible process (**Figure 2b**). After quenching with approximately 350 mL of water, the polymers are stirred with cation exchanger (DOWEX® Monosphere® 650C; hydrogen form) overnight before the molecular weight and the dispersity ( $\mathcal{D}$ ) are determined by gel permeation chromatography. The resulted molecular weight ranges from  $M_w = 3.9$  kDa to  $M_w = 9.7$  kDa and the mean dispersity is about  $1.75 \pm 0.12$  for all raw polymers (**Table 1**).

**Table 1.** Overview properties of raw hPG

	rel. torque [Ncm]	glycidol		[M]/[I] [-]	theory	GPC		
		[g]	[mol]		M [kDa]	$M_n$ [kDa]	$M_w$ [kDa]	$\mathcal{D}$ [-]
hPG-1	4.3	58.6	0.79	32.7	2.6	2.2	3.9	1.75
hPG-2	7.5	80.2	1.08	44.7	3.4	2.7	4.9	1.85
hPG-3a	10.1	132.8	1.79	74.1	5.6	3.8	6.5	1.72
hPG-3b	10.1	132.6	1.79	74.0	5.6	3.6	6.5	1.80
hPG-3c	10.1	131.5	1.78	73.4	5.6	3.2	6.1	1.90
hPG-4	13.7	173.3	2.34	93.6	7.3	4.9	8.5	1.72
hPG-5	17.6	253.7	3.42	128.2	10.6	6.2	9.7	1.52

To prove the reproducibility, the polymerization is performed three times until the relative torque of 10.1 Ncm is reached (Table 1; hPG-3a-c). 10.1 Ncm is chosen because the terminal torque value is in the middle of the tested torque range.

The measured torque values correspond to the molecular weight of the raw hPG. By plotting terminal relative torque values against the measured molecular weight of the raw polymers (obtained by GPC) a linear correlation between these two parameters is observed (see **Figure 3**).

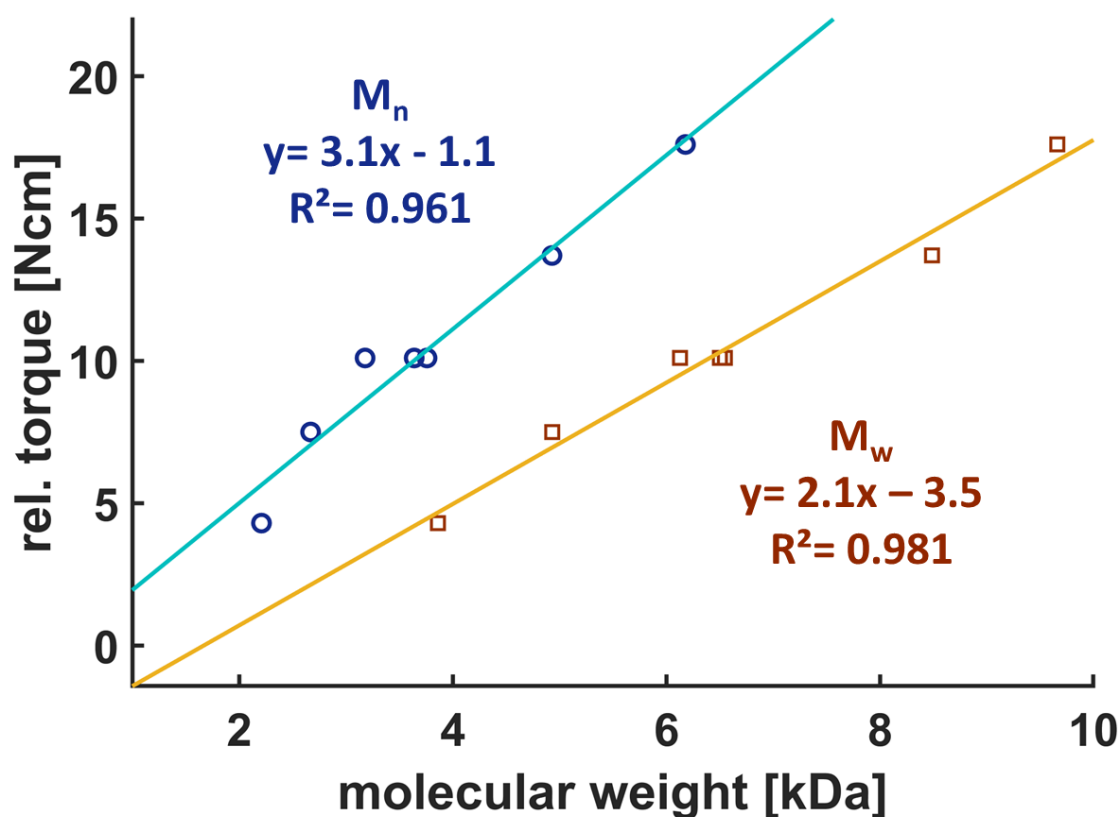


**Figure 3.** Correlation between terminal torque values and resulting molecular weight of raw hPG polymers, determined by GPC. Number average  $M_n$  are shown in blue circles and weight average  $M_w$  in orange squares. Lines present a linear fit.

A high linear correlation of the weight average ( $M_w$ ) with  $R^2 = 0.981$  and of the number average ( $M_n$ ) with  $R^2 = 0.961$  is discovered. A reason for the slightly lower coefficient of determination of  $M_n$  could be that small amounts of glycidol does not drop on the bottom of the reactor rather gets hit by the anchor stirrer blades. In this case the glycidol could get in contact with the reactor wall, where self-initiation due to the elevated temperature (100 °C) could occur. The resulting polymers or oligomers are smaller than the main polymers, which are initiated by TMP at the bottom of the reactor. Since the smaller polymers have a greater influence on  $M_n$  than  $M_w$  the linear correlation of  $M_n$  may fluctuate more than the correlation of  $M_w$ . However, the difference of the coefficient of determination is small.

With the knowledge of the correlation of the relative torque value and the molecular weight, it is possible to translate the online measured torque value to the molecular weight of the polymer in the reactor. This practicable and easy monitoring approach can be done in

all reactors with torque detection. The method fills the gap of online monitoring systems for polymerizations with high viscosity, which could not be covered yet by sample withdrawing systems with following analysis due to difficulties to pump them through the sensor or adhesion to sensors.<sup>[25]</sup>

Purification of polymer amounts in scales of hundreds of grams is mostly done by precipitation in a non-solvent e.g. for hPG acetone. Since our non-solvent polymerization approach tries to fulfill most green chemistry principles, precipitation in organic solvent is refused.<sup>[33]</sup> Here, tangential flow filtration (TFF) is used to purify big amounts of polymer by cycling aqueous polymer solution over an ultrafiltration membrane. Impurities like oligomer, monomer, solvents, salts are removed as permeate and the volume is replaced by fresh water.<sup>[34]</sup> The setup of the TFF is shown in the SI (see **Figure S6**). Due to the usage of certain ultrafiltration membranes with specific molecular weight cut-off (MWCO) the purification can be controlled. Unfortunately, the lowest available MWCO is 1 kDa,<sup>[34]</sup> which lead to a higher loss for smaller polymers like hPG-2 (yield: 33.7 %; **Table 2**). To prevent a high loss of hPG-1, the polymer is dialyzed in a dialysis tube with a molecular weight cut-off of 500 Da against water (yield: 85.2 %). All other polymers are purified with TFF using 1 MWCO. The mean dispersities decrease from 1.75 to 1.37, which shows that oligomers or small polymers are formed during the polymerization, that can be removed using the TFF purification procedure (**Figure 4c**). The here-obtained dispersities are comparable with dispersities out of other studies. Paulus et al. used NMP and THF during the polymerization and obtained hPGs on a kilogram scale with dispersities of  $\bar{D} = 1.9$  (target  $M_n = 2.5$  kDa),  $\bar{D} = 1.4$  (target  $M_n = 5$  kDa) and  $\bar{D} = 2.27$  (target  $M_n = 20$  kDa).<sup>[28]</sup> Kainthan et al. achieved hPG without solvent in 27 g scale with  $\bar{D} = 1.2$  (target  $M_n = 3$  kDa) and  $\bar{D} = 1.6$  (target  $M_n = 20$  kDa).<sup>[35]</sup> This states that the solvent-free polymerization method is in case of the dispersity able to produce similar qualities of hPG.



**Table 2.** Polymer properties after purification by TFF (MWCO: 1kDa).

	theory		GPC		yield	<sup>13</sup> C NMR
	M	M <sub>n</sub>	M <sub>w</sub>	<i>D</i>		DB
	[kDa]	[kDa]	[kDa]	[-]		[%]
hPG-1 <sup>a</sup>	2.6	3.5	5.0	1.41	85.2	59.0
hPG-2	3.4	4.2	6.0	1.43	33.7 <sup>b</sup>	58.2
hPG-3a	5.6	5.7	7.5	1.33	74.4	61.5
hPG-3b	5.6	5.2	7.1	1.37	84.5	55.3
hPG-3c	5.6	4.7	6.7	1.41	79.3	60.2
4-hPG	7.3	6.2	9.0	1.45	90.1	61.3
5-hPG	10.6	8.9	11.0	1.24	85.7	58.0

<sup>a</sup> hPG-1 was dialyzed in a dialysis tube (MWCO: 0.5 kDa).

<sup>b</sup> Loss occurred due to the TFF membrane cutoff (MWCO: 1 kDa).

The purified polymers are further characterized by <sup>1</sup>H NMR to verify the structure of the polymer (**Figure 4a**). Additionally, the methyl- and methylene group of the starter TMP could be identified, which indicates that the polymerization started from the deprotonated TMP and not by thermal self-initiation of glycidol. As discussed before self-initiated polymers are smaller and might have been removed by the TFF before the NMR measurement.

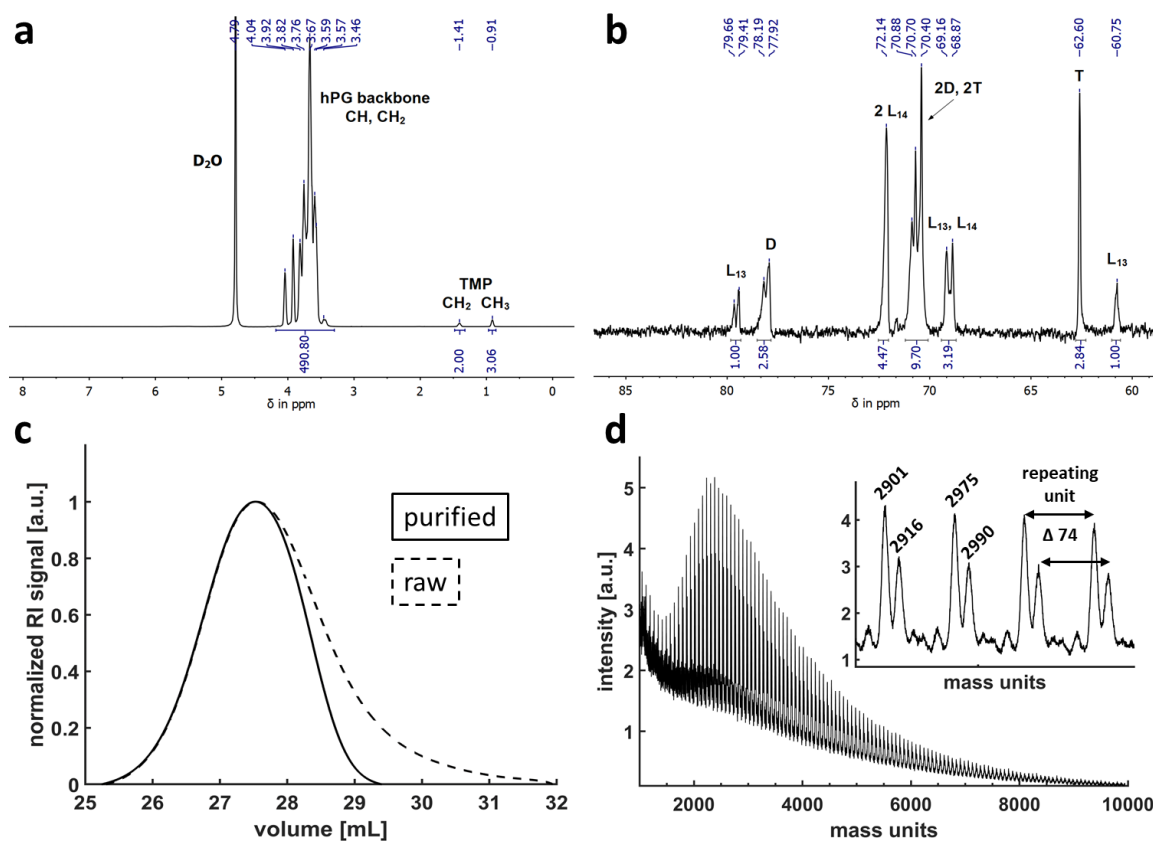


**Figure 4.** Characterization of hPG-3a after TFF purification. (a)  $^1\text{H}$  NMR (300 MHz,  $\text{D}_2\text{O}$ ). (b) Inverse-gated  $^{13}\text{C}$  NMR (700 MHz,  $\text{D}_2\text{O}$ ). (c) Gel permeation chromatography (GPC), raw polymer (dashed line) and after purification with TFF (solid line, 1 kDa MWCO). (d) Matrix-assisted-laser-desorption-ionization time of flight (MALDI-TOF), peak difference determines the molar mass of the repeat unit, the two-peak pattern is due to different counter ions (sodium and potassium).

The different structural units within the polymer like 1,3 linear ( $L_{13}$ ) or 1,4 linear ( $L_{14}$ ), dendritic (D) and terminal units (T) are investigated from  $^{13}\text{C}$  NMR measurements (**Figure 4b**). On the basis of the structural units the degree of branching (DB) can be calculated according to Frey et al.<sup>[2]</sup>

$$DB = \frac{2D}{2D + L_{13} + L_{14}}$$

Additionally, matrix-assisted laser desorption/ionization time-of-flight (MALDI-TOF) mass spectrometry is used to characterize the hPGs. Due to the hyperbranched nature of hPG

not all molecules can be captured at the detector, especially for molecular weights above 5 kDa.<sup>[28]</sup> The reason might be that not all ionized molecules are able to go into the gas phase. Therefore, the distribution of the molecular weight based on MALDI is not included in this study. However, the difference of the mass peaks reveals the molecular weight of the repeat unit (**Figure 4d**). The determined difference is  $74 \text{ g mol}^{-1}$  and matches with the expected molecular weight of the monomer glycidol ( $74.08 \text{ g mol}^{-1}$ ). Therefore, it can be verified that hyperbranched polyglycerol is obtained with the solvent-free polymerization method.

## Conclusion

In this study, a solvent-free green polymerization method for hyperbranched polyglycerol was established. In order to achieve a high reproducibility and ensure traceability an automated reactor system is used. The torque development during the slow monomer addition was the same for all seven polymerizations the same, when the quality of the reactants was kept constant. Also, the three reproduced polymerizations to the identical relative torque increase of  $10.1 \text{ Ncm}$  resulted in the same amount of added glycidol ( $132.3 \pm 0.7 \text{ g}$ ). The same torque developments and the repeated polymer batches indicate a good reproducibility of this method. The produced hPG polymers range in size from  $M_w = 3.9 \text{ kDa}$  to  $M_w = 9.7 \text{ kDa}$  and have mean dispersity of  $1.75 \pm 0.12$  in crude state and  $1.37 \pm 0.07$  after purification with TFF as well as high yield ( $> 75 \%$ ).

Further, it was achieved to detect empirically a linear correlation between the relative torque values and the molecular weight of the hPG in the reactor by the generation of a calibration curve. This correlation can be used for future polymer batches to determine online the molecular weight during the polymerization. This approach is an easy, practical and inexpensive method for online monitoring of the molecular weight. A drawback of the method is that a calibration is necessary to reveal the torque-molecular weight correlation. However, the sample-withdrawing systems of common online monitoring methods for the molecular weight fail for solvent-free polymerizations due to the high viscosity. Therefore, our presented method fills the gap for probing online molecular weights during bulk polymerizations. Further, this method does not require further equipment and can be applied for all reactors with torque detection after the correlation of molecular weight and torque increase is determined.

## Experimental Section

**Material** – glycidol (96.0 %) from Sigma Aldrich was purified by vacuum distillation. 1,1,1-trimethylolpropane (TMP, 97.0 %) and Dowex® Monosphere® 650C (hydrogen form) were obtained from Sigma Aldrich (Steinheim, Germany). Molecular sieves (4 Å, type 514, pearls) were obtained from Roth. Methanol (99.8 %, extra dry over molecular sieves) received from Acros Organics (Geel, Belgium). Potassium hydroxide (KOH, analytical reagent grade) was obtained from Fisher Scientific (Schwerte, Germany). Deuterium oxide (D<sub>2</sub>O, 99.9 %) obtained from Deutero (Kastellaun, Germany). All reagents were used as received without any purification unless otherwise mentioned.

**Distillation of glycidol** – The distillation apparatus out of 2 Schlenk flasks connected through a distillation bridge was dried three times and flushed with argon. The distillation was done under inert condition. 700 – 800 mL of glycidol was exposed to reduced pressure and slightly heated to 40 °C. The pre-carriage of approximately 100 mL was collected in a flask at -78 °C (acetone/ dry ice) until 10<sup>-3</sup> mbar was reached. Afterwards the desired fraction was collected in a 1 L Schlenk flask filled with activated molecular sieves (pore size 4 Å). After 4 h of distillation at 45 °C and 10<sup>-3</sup> mbar approximately 600 ml distilled glycidol was collected and stored at 4 °C under argon. A yellow distillation residue (approx. 20 mL) remained.

**Solvent-free polymerization of hPG** – For all performed polymerization the preparation and all parameters were kept the same except the added amount of monomer was varied. The amount of added monomer was stopped when an assigned terminal torque value was reached. The process sequence was controlled by the automated system. See the flow chart of the polymerization in the SI (**Figure S7**).

The 0.5 L reactor was heated to 100 °C and the pressure was decreased to 3 mbar. Afterwards, the reactor was filled with argon. This evacuation step was repeated after 1.5 h and 3 h. To ensure that no water residues are left in the system, the temperature was kept at 100 °C and 3 mbar for 17 h. Afterwards, the reactor was flushed with argon and the temperature was decreased to 60 °C. At that temperature TMP (3.35 g, 24.2 mmol, 1.0 eq.) was added manually under argon counterflow. By increasing the temperature to 65 °C TMP was molten at a stirring speed of 50 rpm (anchor stirrer). Possible water content in the TMP was removed by decreasing the pressure to 3 mbar for 20 min at the molten state. Small gas

bubbles indicated the evaporation of the water residues. Then the temperature was decreased to 55 °C and 10 mL methanolic potassium hydroxide (0.52 g, 9.3 mmol, 0.38 eq.) solution added. TMP was dissolved and partially deprotonated (approx. 10 % of the OH groups) while a stirring speed of 50 rpm. After 1 h the pressure was decreased to remove the methanol. This was done in several steps (see flow chart SI Figure S7) to prevent spilling of by evaporated methanol. Evaporated methanol was condensed and collected. The final pressure of 3 mbar was kept for 3 h to remove the whole methanol. Then the reactor was flushed with argon, the temperature increased to 100 °C and the stirrer speed was increased to 100 rpm. These parameters were kept during polymerization. With the automated addition ( $18 \text{ g h}^{-1}$ ) of distilled glycidol the polymerization started. The addition continued until an assigned torque value was reached. The total dosed amount of glycidol was recorded by the system (see **Table 1**). After the addition of monomer was stopped, the polymerization condition was kept for at least 2 h to ensure no unreacted monomer is left. Finally, the polymerization was quenched with water (approx. 350 mL) and the temperature was decreased to 60 °C. The added water dissolved the polymer and enabled to take out the polymer through a drain valve at the bottom of the reactor.

**Purification of hPG** – The aqueous polymer solution out of the reactor was taken and cation exchanger beads (DOWEX® Monosphere® 650C) were added and stirred for 20 h to remove the potassium ions. By filtration through a frit (size 2) the beads were removed from the polymer solution. Afterwards, tangential flow filtration (TFF) was performed using an ultrafiltration cassette (Millipore Pellicon® 2 mini, MWCO 1 kDa) and a mini cassette holder (Pellicon® XX42PMINI). Aqueous polymer solution of approximately 0.1 g/mL were cycled in the diafiltration system for 72 h. During the filtration small polymer fractions and small molecule impurities were removed as permeate (approx. 5 L) and continuously replaced with fresh deionized water. Afterwards, all polymers were freeze-dried to remove the water and the yield was determined. The smallest synthesized polymer (15 Ncm) was differently purified due to expected high loss during diafiltration with MWCO 1 kDa. It was dialyzed in a dialysis tube (500 Da MWCO, cellulose ester, Spectrum Laboratories, Waltham, US) against water for 72 h.

**GPC** – The molecular weight distributions ( $M_n$ ,  $M_w$ ) and the dispersity were determined by GPC using a refractive index detector (RI) at 40 °C. 100  $\mu$ L samples with a concentration of 6 mg/mL were injected. Three columns (Polymer Standards Service GmbH (PSSS), Germany; Suprema 100 Å and two 1000 Å; 10  $\mu$ m particle size) were used to separate the sample under a flow of 1 mL min<sup>-1</sup> sodium nitrate solution as mobile phase (0.1 M) at room temperature. The system was calibrated with pullulan standards from PSS.

**NMR** – NMR spectra were recorded with 400 Hz using a JEOL ECX spectrometer (JOEL, Freising, Germany). D<sub>2</sub>O was used as solvent and as reference for all proton (<sup>1</sup>H) and carbon (<sup>13</sup>C) NMR measurements. The chemical shifts were determined in ppm. Carbon NMR was measured with inverse gated decoupling to allow quantification of the spectra.

**MALDI** – Resulting hPGs were characterized by MALDI-TOF mass spectrometry to derive the repeat unit of the polymer. Ultraflex-II TOF/TOF instrument (Bruker Daltonics, Bremen, Germany) equipped with a 200 Hz solid-state Smartbeam™ laser was used.  $\alpha$ -Cyano-4-hydroxycinnamic acid (CHCA) was taken as matrix and sample spotting preparation was done by dried droplet technique. All spectra were acquired in positive linear mode and were separated by the  $m/z$  range of 500 to 20,000.

### **Acknowledgements**

This research was supported by the German Research Foundation (DFG) by grants from SFB 765, the Core Facility BioSupraMol and the Focus Area Nanoscale (Freie Universität Berlin). The authors thank Cathleen Hudziak for extensive GPC measurements. Dr. Pamela Winchester is acknowledged for proof reading the manuscript. Hitec Zhang is thanked for technical support regarding the automated reactor system.

## References

- [1] Calderón, M.; Quadir, M. A.; Sharma, S. K.; Haag, R., Dendritic polyglycerols for biomedical applications. *Advanced materials* **2010**, *22* (2), 190-218.
- [2] Sunder, A.; Hanselmann, R.; Frey, H.; Mülhaupt, R., Controlled synthesis of hyperbranched polyglycerols by ring-opening multibranching polymerization. *Macromolecules* **1999**, *32* (13), 4240-4246.
- [3] Sunder, A.; Mülhaupt, R.; Haag, R.; Frey, H., Hyperbranched polyether polyols: a modular approach to complex polymer architectures. *Advanced Materials* **2000**, *12* (3), 235-239.
- [4] Wilms, D.; Nieberle, J.; Klos, J.; Loewe, H.; Frey, H., Synthesis of hyperbranched polyglycerol in a continuous flow microreactor. *Chemical Engineering & Technology: Industrial Chemistry-Plant Equipment-Process Engineering-Biotechnology* **2007**, *30* (11), 1519-1524.
- [5] Anilkumar, P.; Lawson, T. B.; Abbina, S.; Mäkelä, J. T.; Sabatelle, R. C.; Takeuchi, L. E.; Snyder, B. D.; Grinstaff, M. W.; Kizhakkedathu, J. N., Mega macromolecules as single molecule lubricants for hard and soft surfaces. *Nature Communications* **2020**, *11* (1), 1-9.
- [6] Imran ul-haq, M.; Sheno, R. A.; Brooks, D. E.; Kizhakkedathu, J. N., Solvent-assisted anionic ring opening polymerization of glycidol: Toward medium and high molecular weight hyperbranched polyglycerols. *Journal of Polymer Science Part A: Polymer Chemistry* **2013**, *51* (12), 2614-2621.
- [7] Weinhart, M.; Grunwald, I.; Wyszogrodzka, M.; Gaetjen, L.; Hartwig, A.; Haag, R., Linear poly (methyl glycerol) and linear polyglycerol as potent protein and cell resistant alternatives to poly (ethylene glycol). *Chemistry—An Asian Journal* **2010**, *5* (9), 1992-2000.
- [8] Thomas, A.; Müller, S. S.; Frey, H., Beyond poly (ethylene glycol): linear polyglycerol as a multifunctional polyether for biomedical and pharmaceutical applications. *Biomacromolecules* **2014**, *15* (6), 1935-1954.
- [9] Mohammadifar, E.; Bodaghi, A.; Dadkhahtehrani, A.; Nematikharat, A.; Adeli, M.; Haag, R., Green synthesis of hyperbranched polyglycerol at room temperature. *ACS Macro Letters* **2016**, *6* (1), 35-40.
- [10] Mohammadifar, E.; Zabihi, F.; Tu, Z.; Hedtrich, S.; Kharat, A. N.; Adeli, M.; Haag, R., One-pot and gram-scale synthesis of biodegradable polyglycerols under ambient conditions: nanocarriers for intradermal drug delivery. *Polymer Chemistry* **2017**, *8* (47), 7375-7383.
- [11] Ferraro, M.; Silberreis, K.; Mohammadifar, E.; Neumann, F.; Dervede, J.; Haag, R., Biodegradable Polyglycerol Sulfates Exhibit Promising Features for Anti-inflammatory Applications. *Biomacromolecules* **2018**, *19* (12), 4524-4533.
- [12] Zabihi, F.; Koeppe, H.; Achazi, K.; Hedtrich, S.; Haag, R., One-Pot Synthesis of Poly (glycerol-co-succinic acid) Nanogels for Dermal Delivery. *Biomacromolecules* **2019**, *20* (5), 1867-1875.
- [13] Zabihi, F.; Graff, P.; Schumacher, F.; Kleuser, B.; Hedtrich, S.; Haag, R., Synthesis of poly (lactide-co-glycerol) as a biodegradable and biocompatible polymer with high loading capacity for dermal drug delivery. *Nanoscale* **2018**, *10* (35), 16848-16856.
- [14] Fleige, E.; Quadir, M. A.; Haag, R., Stimuli-responsive polymeric nanocarriers for the controlled transport of active compounds: concepts and applications. *Advanced drug delivery reviews* **2012**, *64* (9), 866-884.
- [15] Nowag, S.; Haag, R., pH-responsive micro-and nanocarrier systems. *Angewandte Chemie International Edition* **2014**, *53* (1), 49-51.
- [16] Zhong, Y.; Dimde, M.; Stöbener, D.; Meng, F.; Deng, C.; Zhong, Z.; Haag, R., Micelles with sheddable dendritic polyglycerol sulfate shells show extraordinary tumor targetability and chemotherapy in vivo. *ACS Applied Materials & Interfaces* **2016**, *8* (41), 27530-27538.
- [17] Osorio-Blanco, E. R.; Rancan, F.; Klossek, A.; Nissen, J. H.; Hoffmann, L.; Bergueiro, J.; Riedel, S.; Vogt, A.; Ruehl, E.; Calderon, M., Polyglycerol-based Thermo-responsive Nanocapsules Induce Skin Hydration and Serve as Skin Penetration Enhancer. *ACS Applied Materials & Interfaces* **2020**.
- [18] Frombach, J.; Rancan, F.; Kübrich, K.; Schumacher, F.; Unbehauen, M.; Blume-Peytavi, U.; Haag, R.; Kleuser, B.; Sabat, R.; Wolk, K., Serine Protease-Mediated Cutaneous Inflammation:

- Characterization of an Ex Vivo Skin Model for the Assessment of Dexamethasone-Loaded Core Multishell-Nanocarriers. *Pharmaceutics* **2020**, *12* (9), 862.
- [19] Bhatia, S.; Hilsch, M.; Cuellar Camacho, J. L.; Ludwig, K.; Nie, C.; Parshad, B.; Wallert, M.; Block, S.; Lauster, D.; Böttcher, C., Adaptive flexible sialylated nanogels as highly potent influenza A virus inhibitors. *Angewandte Chemie International Edition* **2020**.
- [20] Bhatia, S.; Lauster, D.; Bardua, M.; Ludwig, K.; Angioletti-Uberti, S.; Popp, N.; Hoffmann, U.; Paulus, F.; Budt, M.; Stadtmüller, M.; Wolff, T.; Hamann, A.; Böttcher, C.; Herrmann, A.; Haag, R., Linear polysialoside outperforms dendritic analogs for inhibition of influenza virus infection in vitro and in vivo. *Biomaterials* **2017**, *138*, 22-34.
- [21] Dervede, J.; Rausch, A.; Weinhart, M.; Enders, S.; Tauber, R.; Licha, K.; Schirner, M.; Zügel, U.; von Bonin, A.; Haag, R., Dendritic polyglycerol sulfates as multivalent inhibitors of inflammation. *Proceedings of the National Academy of Sciences* **2010**, *107* (46), 19679-19684.
- [22] Fevola, M. J.; Sun, F. C.; York, S. E., Designing new functional cosmetic ingredients from polyglycerol, a versatile bio-based platform for improved sustainability. *Journal of cosmetic science* **2017**, *68* (1), 42-47.
- [23] Schubert, C.; Schömer, M.; Steube, M.; Decker, S.; Friedrich, C.; Frey, H., Systematic Variation of the Degree of Branching (DB) of Polyglycerol via Oxyanionic Copolymerization of Glycidol with a Protected Glycidyl Ether and Its Impact on Rheological Properties. *Macromolecular Chemistry and Physics* **2018**, *219* (1), 1700376.
- [24] Mankar, R. B.; Saraf, D. N.; Gupta, S. K., On-line optimizing control of bulk polymerizations: 1. Development of a software sensor. *Industrial & engineering chemistry research* **1998**, *37* (6), 2436-2445.
- [25] Frauendorfer, E.; Wolf, A.; Hergeth, W. D., Polymerization online monitoring. *Chemical engineering & technology* **2010**, *33* (11), 1767-1778.
- [26] Haven, J. J.; Junkers, T., Online Monitoring of Polymerizations: Current Status. *European Journal of Organic Chemistry* **2017**, *2017* (44), 6474-6482.
- [27] Haipeter, T., Digitalisation, unions and participation: the German case of 'industry 4.0'. *Industrial Relations Journal* **2020**, *51* (3), 242-260.
- [28] Paulus, F.; Weiss, M. E.; Steinhilber, D.; Nikitin, A. N.; Schütte, C.; Haag, R., Anionic ring-opening polymerization simulations for hyperbranched polyglycerols with defined molecular weights. *Macromolecules* **2013**, *46* (21), 8458-8466.
- [29] Hernández, N.; Williams, R. C.; Cochran, E. W., The battle for the "green" polymer. Different approaches for biopolymer synthesis: bioadvantaged vs. bioreplacement. *Organic & biomolecular chemistry* **2014**, *12* (18), 2834-2849.
- [30] Zeschmar-Lahl, B., *Umweltbundesamt* **2017**.
- [31] Kawashima, N.; Yagi, T.; Kojima, K., How Do Bioplastics and Fossil-Based Plastics Play in a Circular Economy? *Macromolecular Materials and Engineering* **2019**, *304* (9), 1900383.
- [32] Hadjichristidis, N.; Iatrou, H.; Pispas, S.; Pitsikalis, M., Anionic polymerization: high vacuum techniques. *Journal of Polymer Science Part A: Polymer Chemistry* **2000**, *38* (18), 3211-3234.
- [33] Anastas, P.; Eghbali, N., Green chemistry: principles and practice. *Chemical Society Reviews* **2010**, *39* (1), 301-312.
- [34] Yee Lau, S.; Pattnaik, P.; Raghunath, B., Integrity Testing of Ultrafiltration Systems for Biopharmaceutical Applications. *BioProcess International* **2012**, *10* (9).
- [35] Kainthan, R. K.; Muliawan, E. B.; Hatzikiriakos, S. G.; Brooks, D. E., Synthesis, Characterization, and Viscoelastic Properties of High Molecular Weight Hyperbranched Polyglycerols. *Macromolecules* **2006**, *39* (22), 7708-7717.

Corresponding authors

\*E-mail: haag@zedat.fu-berlin.de

\*E-mail: stephan.block@fu-berlin.de



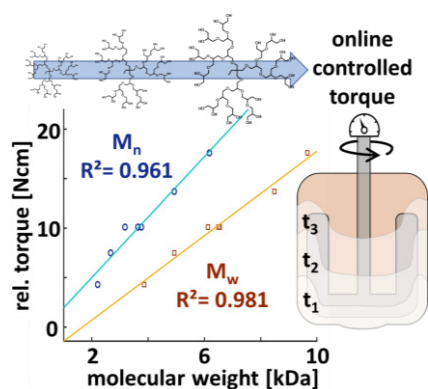
## Notes

The author declares no competing financial interest.

## ToC

An automated solvent-free polymerization of hyperbranched polyglycerol was developed to generate reproducible, biocompatible, non-cytotoxic, and water-soluble polymers for biomedical applications. The empirically investigated correlation between the relative torque and the corresponding molecular weight enabled to monitor the molecular weight online during polymerization.

Keyword: hyperbranched polyglycerol



## Supplementary Information

### Automated Solvent-Free Polymerization of Hyperbranched Polyglycerol with Tailored Molecular Weight by Online Torque Detection

Matthias Wallert,<sup>1</sup> Johann Plaschke,<sup>1</sup> Mathias Dimde,<sup>2</sup> Vahid Ahmadi,<sup>2</sup> Stephan Block,<sup>1</sup> Rainer Haag<sup>2, \*</sup>

<sup>1</sup>Institute of Chemistry and Biochemistry, Emmy-Noether Group "Bionanointerfaces", Freie Universität Berlin, Arnimallee 22, 14195 Berlin, Germany

<sup>2</sup>Institute of Chemistry and Biochemistry, Macromolecular Chemistry, Freie Universität Berlin, Takustr. 3, 14195 Berlin, Germany

\* Corresponding authors

Rainer Haag, e-mail: haag@zedat.fu-berlin.de

Stephan Block, e-mail: stephan.block@fu-berlin.de

<b>Table of contents</b>	page
S1. <sup>1</sup> H NMR of hPG-2	2
S2. <sup>13</sup> C NMR of hPG-2	3
S3. MALDI-TOF measurement of hPG-2	3
S4. MALDI-TOF of hPG-2 zoomed in	4
S5. GPC measurement of hPG-2	5
S6. TFF instrumentation scheme	6
S7. Flow chart of the automated solvent-free polymerization process	7

Details on the characterization of the resulted polymers are presented in this Supplementary Information. The recorded spectra of hPG-2 ( $M_n = 4.2$ ,  $M_w = 6.0$ , and  $\bar{D} = 1.43$ ) are representative for all synthesized hPGs. Recorded NMR, MALDI-TOF, and GPC results are shown (Figure S1-S5). Furthermore, an instrumentation scheme of the TFF purification process is shown (Figure S6). The solvent-free polymerization of hPG is reproducible due to the automatization of the process. The flow chart of the process with each step and its transition is shown (Figure S7). Due to the length of the flow chart this figure is separated in four pages.

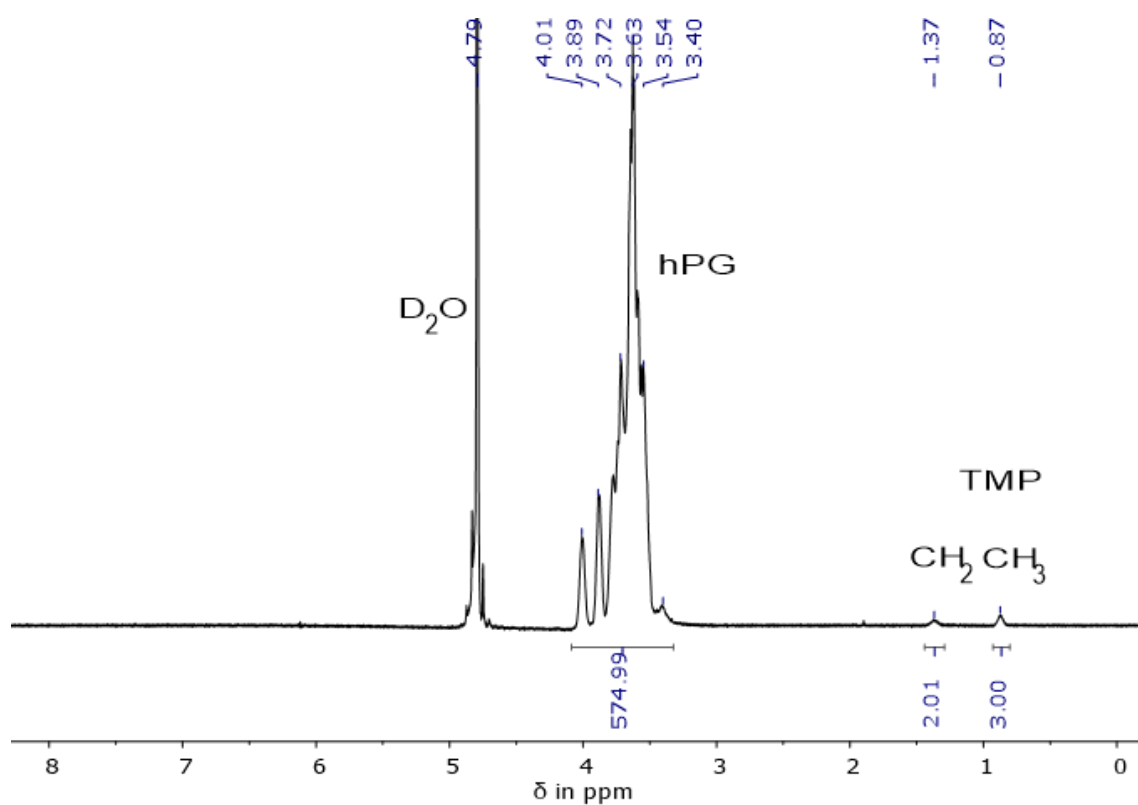


**Figure S1:**  $^1\text{H}$  NMR of hPG-2

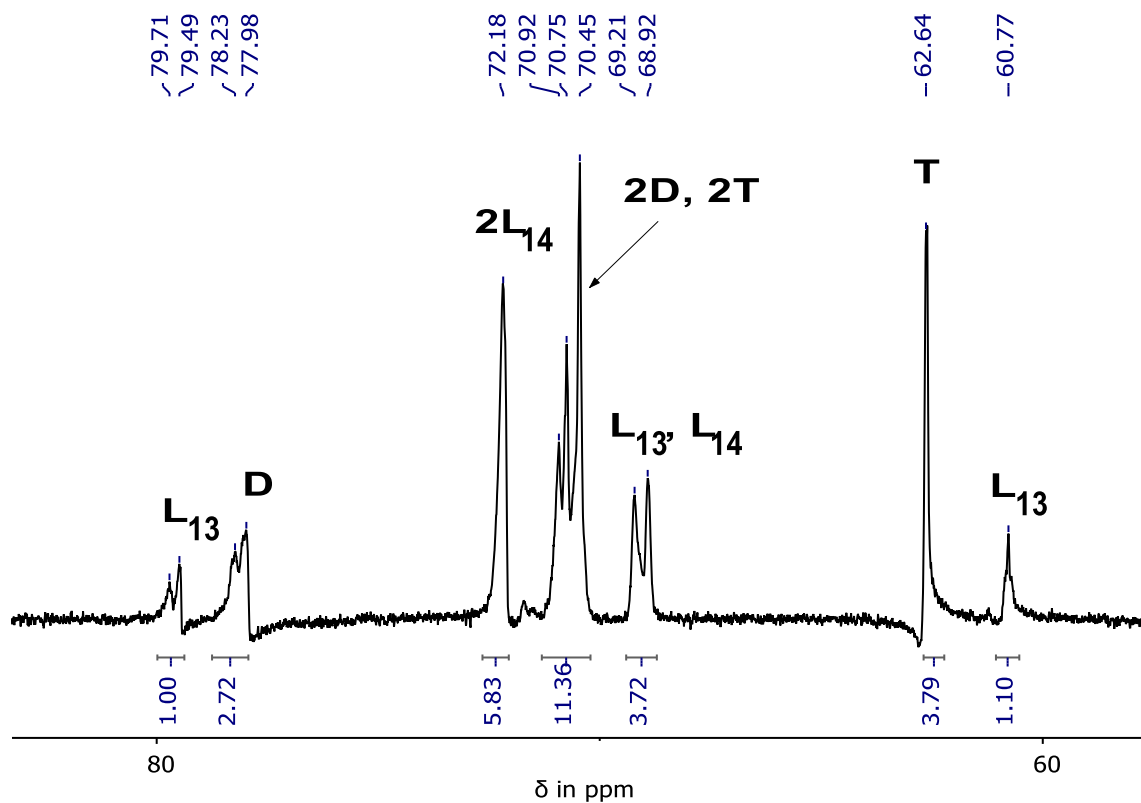


**Figure S2:** The inversely gated  $^{13}\text{C}$  NMR of hPG-2 is used to investigate the structural units of the polymer; 1,3 linear ( $L_{13}$ ) or 1,4 linear ( $L_{14}$ ), dendritic (D) and terminal units (T). The degree of branching (DB = 58.2 %) was calculated from the integrals.

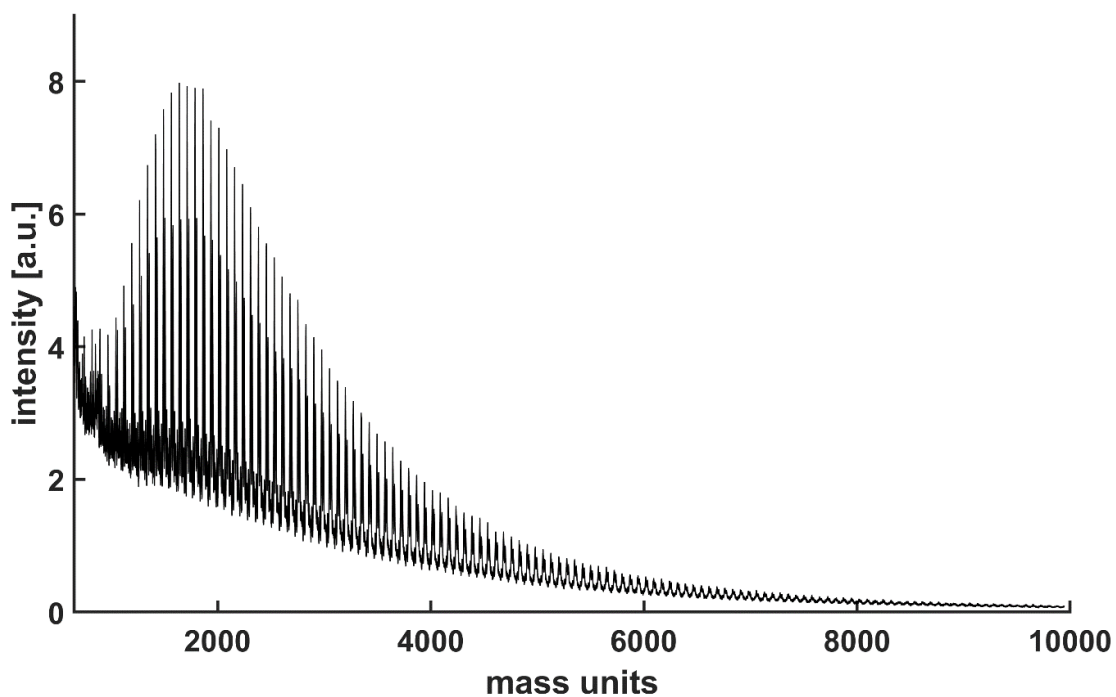


**Figure S3:** MALDI-TOF measurements of hPG-2. The characteristic pattern indicates the repeating of the polymer.

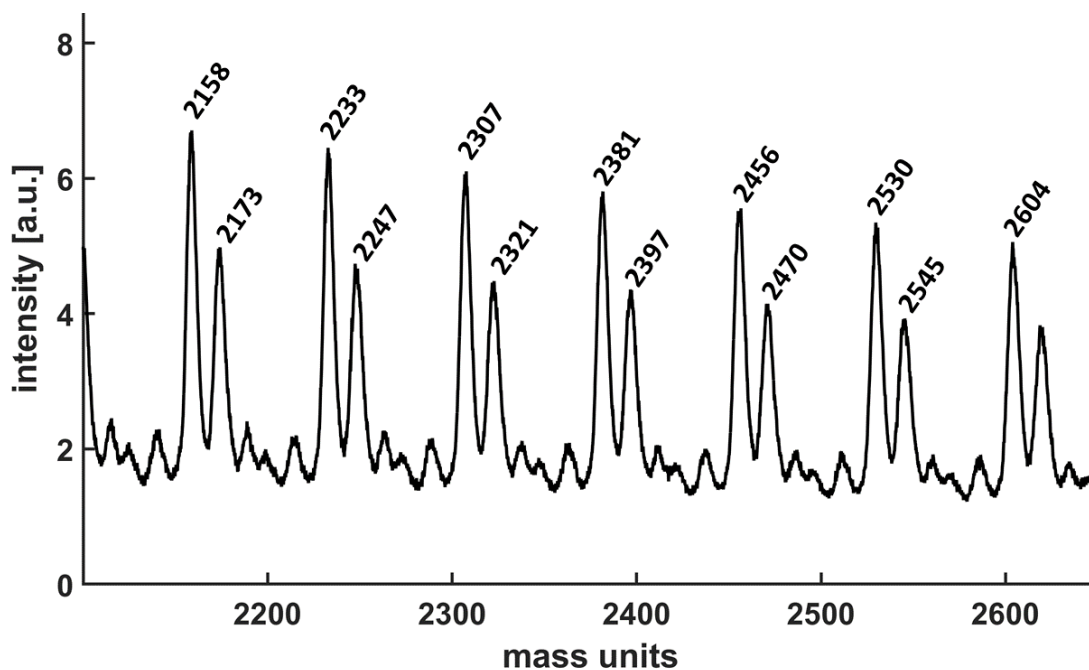


**Figure S4:** Zoomed in view of the MALDI-TOF spectrum of hPG-2. The difference between the mass peaks reveal the molecular weight of the repeating unit. The difference is 74 g/mol, which coincide with the molecular weight of the monomer glycidol (74.08 g/mol).

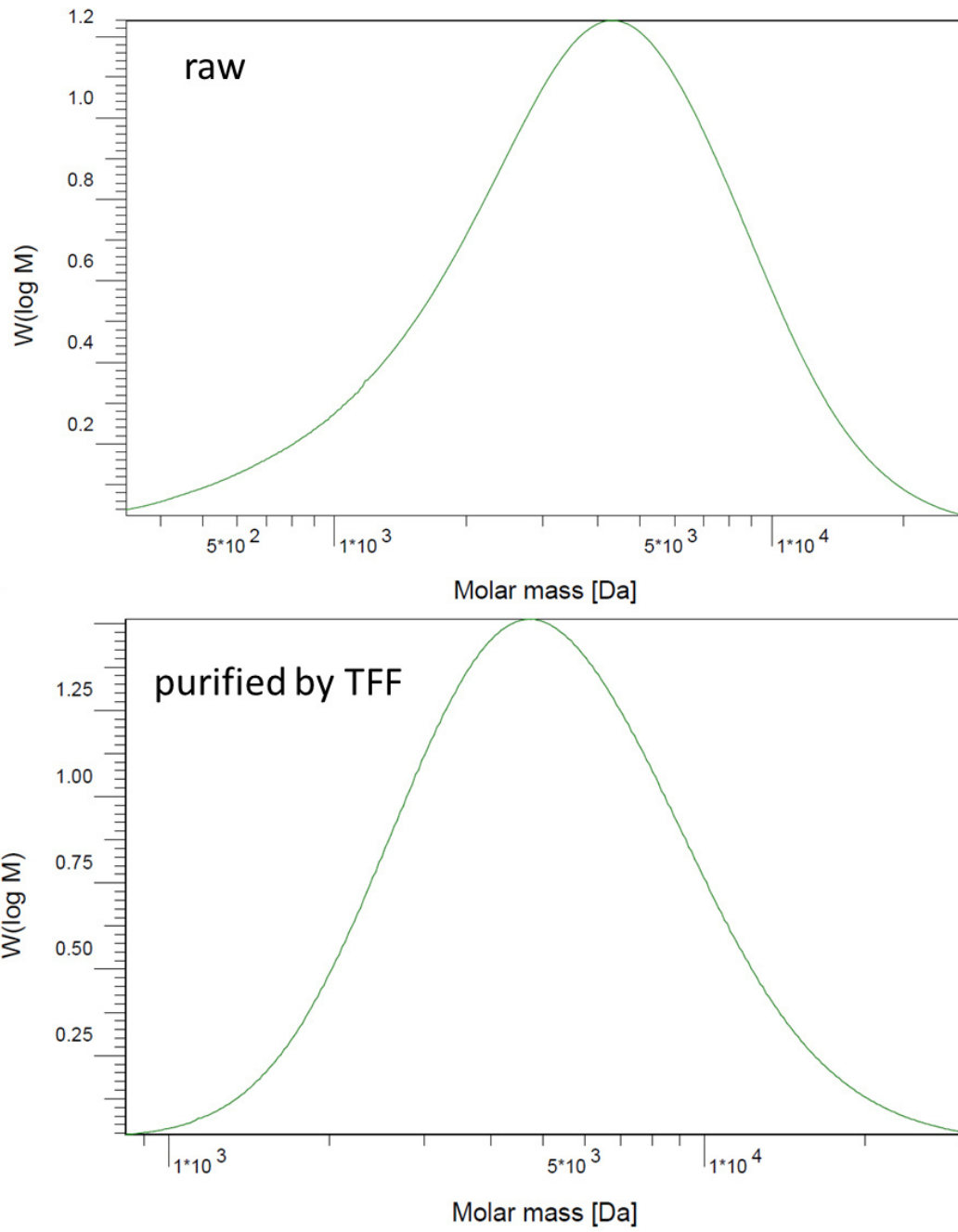


**Figure S5:** GPC measurement of hPG-2 raw (top) and after purification by TFF (1 kDa MWCO, below)

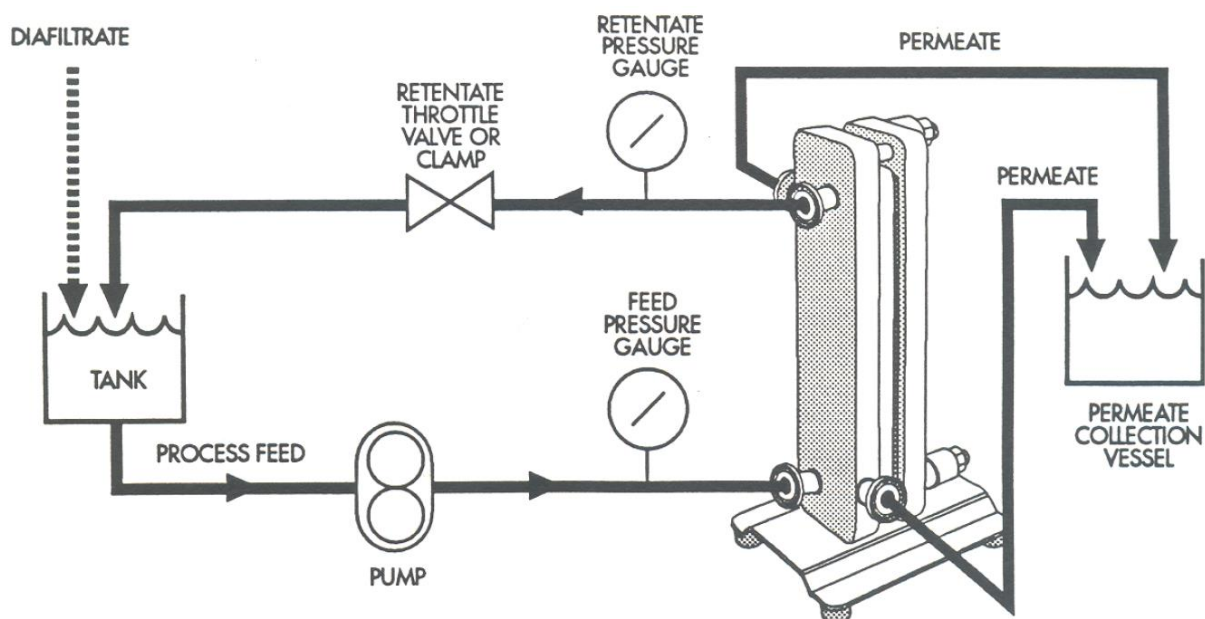
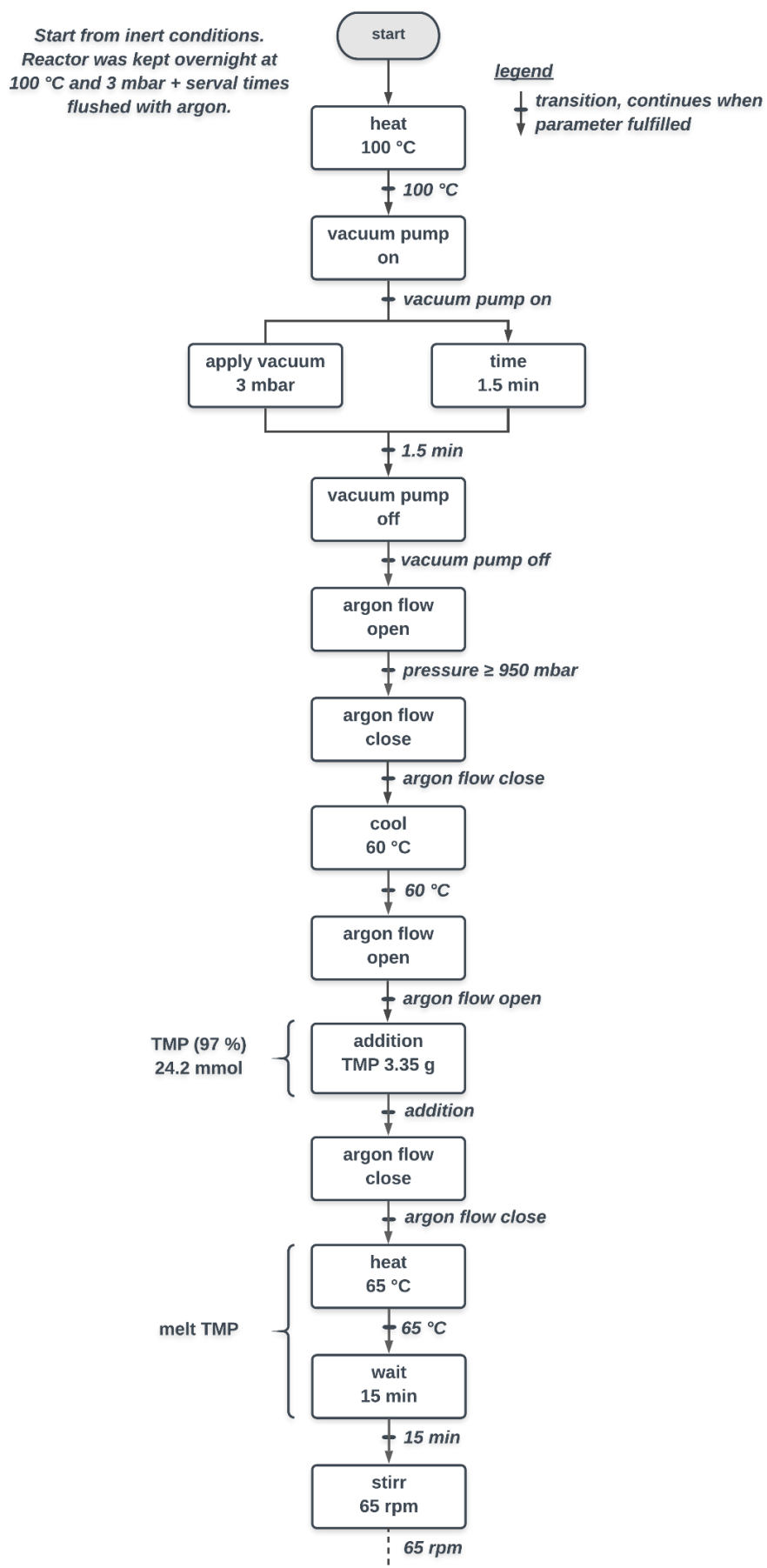


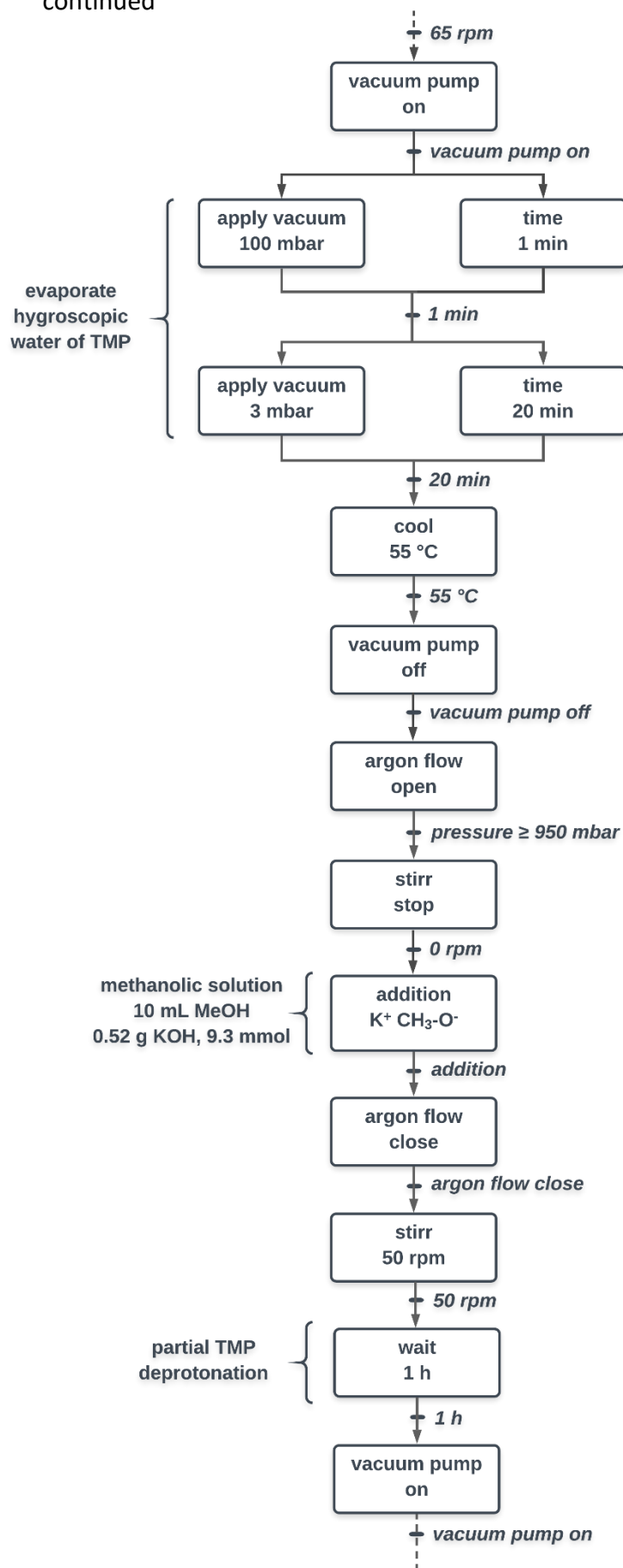
**Figure S6:** Plumbing and instrumentation diagram of the TFF Pellicon® Mini. This filtration method was used to purify the synthesized hPGs. The picture is taken from the user guide. Copyright 2020 Merck KGaA, Darmstadt, Germany.

**Figure S7:** Flow chart of automated reactor protocol

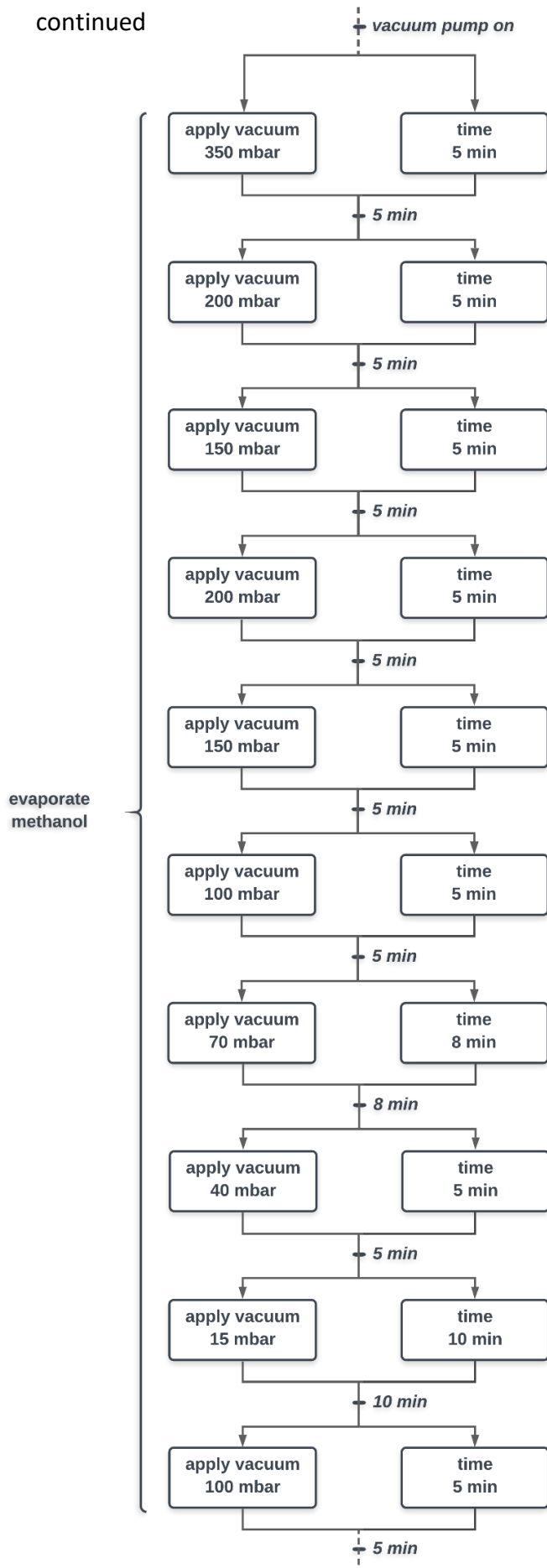




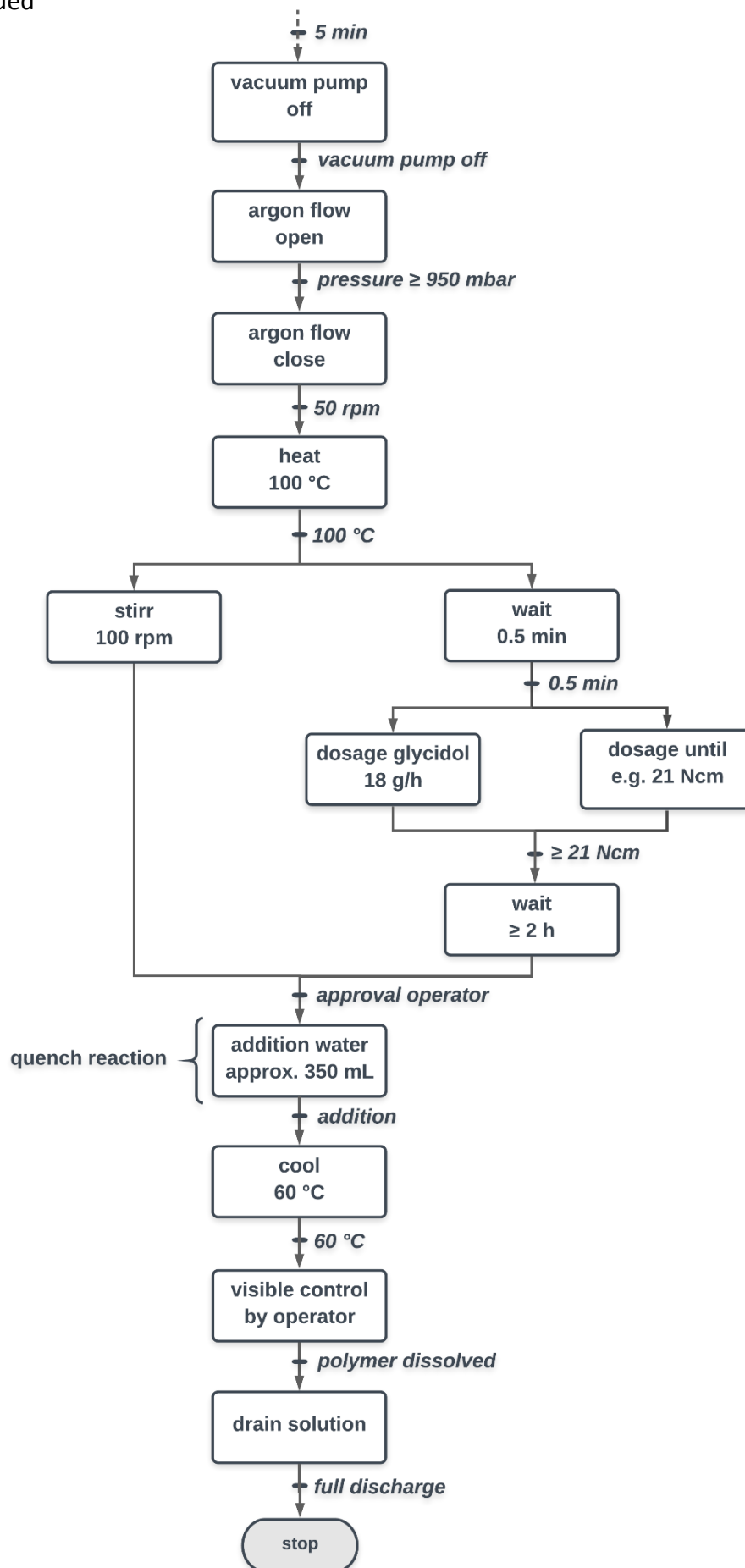
continued



continued



continued



### 3.3 Mucin-inspired, High Molecular Weight Virus Binding Inhibitors Show Biphasic Binding Behavior to Influenza A Viruses

Matthias Wallert, Chuanxiong Nie, Parambath Anilkumar, Srinivas Abbina, Sumati Bhatia, Kai Ludwig, Jayachandran N. Kizhakkedathu, Rainer Haag, Stephan Block, *Small* 2020

<https://doi.org/10.1002/sml.202004635>

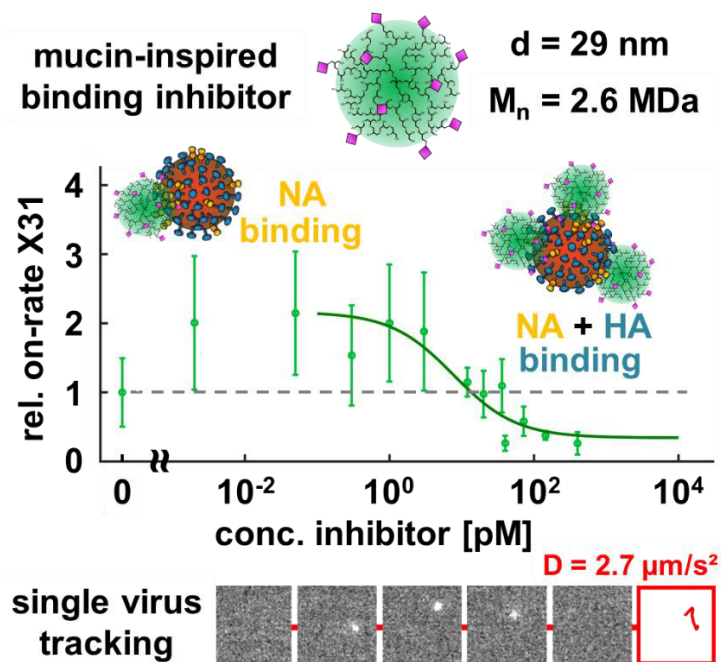


**Figure 21.** Mucin-inspired virus binding inhibitors show biphasic binding behavior to influenza A viruses in the determined attachment-rates measured by TIRF microscopy. Reprinted with permission from ref.<sup>[166]</sup>. Copyright 2020 Wiley-VCH GmbH.

**Author's contribution:** Matthias Wallert did the polymerization of the MDa-sized hPG polymer, functionalization of the mucin-inspired binding inhibitors, performed all TIRF measurements and analyzed the attachment-rates, probed the inhibitors using HAI assay, and wrote the manuscript. Chuanxiong Nie performed the cell-binding tests and introduced me to the HAI assay; Parambath Anilkumar introduced me in the synthesis of MDa-sized hPGs, Srinivas Abbina supported the MDa-sized polymerization. Sumati Bhatia provided acetylated propargyl sialic acid and supported the functionalization. Kai Ludwig performed the TEM images of the MDa-sized hPGs. Jayachandran N. Kizhakkedathu and Rainer Haag contributed with scientific guidance and supervision, Stephan Block analyzed the diffusion and detachment rates, provided the MATLAB scripts for the TIRF analysis, edited the manuscript, and supervised me.

# Mucin-Inspired, High Molecular Weight Virus Binding Inhibitors Show Biphasic Binding Behavior to Influenza A Viruses

Matthias Wallert, Chuanxiong Nie, Parambath Anilkumar, Srinivas Abbina, Sumati Bhatia, Kai Ludwig, Jayachandran N. Kizhakkedathu, Rainer Haag,\* and Stephan Block\*


Multivalent binding inhibitors are a promising new class of antivirals that prevent virus infections by inhibiting virus binding to cell membranes. The design of these inhibitors is challenging as many properties, for example, inhibitor size and functionalization with virus attachment factors, strongly influence the inhibition efficiency. Here, virus binding inhibitors are synthesized, the size and functionalization of which are inspired by mucins, which are naturally occurring glycosylated proteins with high molecular weight (MDa range) and interact efficiently with various viruses. Hyperbranched polyglycerols (hPGs) with molecular weights ranging between 10 and 2600 kDa are synthesized, thereby hitting the size of mucins and allowing for determining the impact of inhibitor size on the inhibition efficiency. The hPGs are functionalized with sialic acids and sulfates, as suggested from the structure of mucins, and their inhibition efficiency is determined by probing the inhibition of influenza A virus (IAV) binding to membranes using various methods. The largest, mucin-sized inhibitor shows potent inhibition at pM concentrations, while the inhibition efficiency decreases with decreasing the molecular weight. Interestingly, the concentration-dependent IAV inhibition shows a biphasic behavior, which is attributed to differences in the binding affinity of the inhibitors to the two IAV envelope proteins, neuraminidase, and hemagglutinin.

## 1. Introduction

Viral infections and resulting pandemics are a human danger and repeatedly get into the focus due to the circulation of newly emerging viruses, such as Zika, influenza, and corona viruses<sup>[1–3]</sup> The development of antivirals to fight viral infections is often a time-consuming process and the generated drugs are often effective only for a certain period of time as mutation of the targeted virus may cause the developed antiviral to become ineffective, for example due to occurrence of resistance.<sup>[4]</sup> Hence, antivirals targeting highly conserved structures of viruses, such as the envelope proteins that are involved in virus binding to the membrane of the host cell, are entering more and more the focus of current research.<sup>[5,6]</sup> As virus binding proteins typically show a very weak affinity to their native attachment factors on the cell membrane,<sup>[7]</sup> viruses bind to cells by forming many protein-receptor interactions in parallel,

M. Wallert, Dr. S. Block  
 Institute of Chemistry and Biochemistry  
 Emmy-Noether Group “Bionanointerfaces”  
 Freie Universität Berlin  
 Takustr. 3, Berlin 14195, Germany  
 E-mail: stephan.block@fu-berlin.de

C. Nie, Dr. S. Bhatia, Prof. R. Haag  
 Institute of Chemistry and Biochemistry  
 Macromolecular Chemistry  
 Freie Universität Berlin  
 Takustr. 3, Berlin 14195, Germany  
 E-mail: haag@zedat.fu-berlin.de

 The ORCID identification number(s) for the author(s) of this article can be found under <https://doi.org/10.1002/smll.202004635>.

© 2020 The Authors. Published by Wiley-VCH GmbH. This is an open access article under the terms of the Creative Commons Attribution License, which permits use, distribution and reproduction in any medium, provided the original work is properly cited.

Dr. P. Anilkumar, Dr. S. Abbina, Prof. J. N. Kizhakkedathu  
 Centre for Blood Research  
 Life Sciences Institute  
 Department of Pathology and Laboratory Medicine  
 University of British Columbia  
 2350 Health Sciences Mall, Vancouver, British Columbia V6T 1Z3, Canada

Dr. K. Ludwig  
 Research Center for Electron Microscopy and Core Facility BioSupraMol  
 Institute of Chemistry and Biochemistry  
 Freie Universität Berlin  
 Fabeckstr. 36a, Berlin 14195, Germany

Prof. J. N. Kizhakkedathu  
 Department of Chemistry  
 University of British Columbia  
 Vancouver, British Columbia V6T 1Z3, Canada

Prof. J. N. Kizhakkedathu  
 School of Biomedical Engineering  
 University of British Columbia  
 Vancouver, British Columbia V6T 1Z3, Canada

DOI: 10.1002/smll.202004635

thereby generating a multivalent interaction to the cell membrane.<sup>[8]</sup> This first step in the infection cycle of cells can be inhibited by addition of multivalent binding inhibitors.<sup>[5,9]</sup>

The design of multivalent virus binding inhibitors is complicated by the fact that many properties, such as inhibitor size and functionalization with virus attachment factors, have a strong impact on the inhibition efficiency,<sup>[10]</sup> making the process of finding inhibitor designs with high inhibition efficiency a time-consuming matter. Nevertheless, the concept of using multivalent interactions to hinder binding of infectious agents (viruses and bacteria) to cells is already implemented in nature by the biological hydrogel mucus, which covers almost all epithelia cells.<sup>[11]</sup> It forms the first defense barrier against viruses and bacteria by capturing such infectious agents before they are able to reach to the cell surface.<sup>[12]</sup> Mucus is formed by dynamic cross-linking of mucins, which are highly glycosylated proteins having molecular weights ranging between 0.1 and few MDa and bind with high specificity and selectivity to viruses while allowing other species (e.g., nutrients) to pass the hydrogel.<sup>[11,13]</sup> As mucins are effective binders of various virus species, our study aims to synthesize virus binding inhibitors, the size and functionalization of which is inspired by mucins, thereby allowing for potent and potentially broad band inhibition of virus binding.

In particular, we aim to generate multivalent virus binding inhibitors reaching molecular weights on the MDa scale, which is a value being in the middle of the weight range reported for mucins.<sup>[13]</sup> Besides mimicking the size of mucins, such large values are further motivated by the observation that the size of a binding inhibitor has a strong impact on its efficiency to bind to viruses,<sup>[10]</sup> which led to the suggestion that the optimal size of a virus binding inhibitor is approximately one third of the size of the virus to be inhibited. As many viruses are within the size range of 30–200 nm, the size of the virus inhibitor should therefore be on the order of a few tens of nanometers, corresponding to polymer scaffolds with a molecular weight hitting the MDa scale. Besides size, the functionalization of the inhibitor is also known to be an important determinant for the strength of the virus-inhibitor interaction. Mucins present a high amount of terminal sialic acid and sulfate moieties,<sup>[12]</sup> which are known to play a role in the binding of various viruses. This motivates to functionalize the virus binding inhibitor with sialic acid and sulfate groups (at degrees of functionalization comparable to mucins) to ensure efficient binding to viruses, thereby offering the perspective to provide broad band virus binding inhibition activity.

The performance of the synthesized, mucin-inspired virus binding (MuVib) inhibitors is investigated by probing the binding inhibition of a H3N2 influenza A virus (IAV) strain using various assays, including a new binding assay based on total internal fluorescence (TIRF) microscopy. MuVib inhibitors with molecular weights ranging between 10 and 2600 kDa are synthesized, which allows to probe the inhibition efficiency as a function of inhibitor size.

## 2. Results and Discussion

The aim of this study is to synthesize virus binding inhibitors, the size and functionalization of which have been motivated

by mucins. With respect to size, this aim requires to synthesize macromolecules having molecular weights on the MDa scale, which can then serve as scaffold for further functionalization with virus attachment factors. Recent studies have demonstrated the synthesis of virus inhibitors hitting the MDa range, which were based on polyacrylamide, polyamidoamine, polyethylene imine or copolymers of them,<sup>[14]</sup> but showed only little biocompatibility due to their positive charges. In order to generate a high molecular weight (MDa-sized) multivalent virus binding inhibitor, we therefore decided to use hyperbranched polyglycerols (hPG), which are known to be highly biocompatible and the synthesis of single hPG molecules with molecular weights of several 100 kDa has recently been demonstrated.<sup>[15,16]</sup> The strategy for the synthesis of MDa-sized hPG molecules for use as mucin-inspired virus binding (MuVib) inhibitor is shown in **Figure 1a**. In addition to this inhibitor, hPGs with lower molecular weights (ranging between 10 and 500 kDa) have been synthesized, which allows for investigating the effect of the inhibitor size on the inhibitor efficiency as suggested in a recent work by Vonnemann et al.<sup>[10]</sup> While single hPG molecules up to 600 kDa can be synthesized in a single step,<sup>[17]</sup> the synthesis of the 2600 kDa hPG molecules required an additional step, in which 600 kDa hPGs served as macroinitiator for a further polymerization (**Figure 1a**) to generate a mucin-sized polymer.<sup>[16]</sup> This approach yielded 4 different hPG scaffolds with molecular weights of 10, 100, 500, and 2600 kDa (**Table 1**). DLS measurements yielded hydrodynamic diameter of ≈6 nm (10 kDa), 9 nm (100 kDa), 13 nm (500 kDa), and 29 nm (2600 kDa), respectively.

Besides size, the functionalization of a polymer scaffold surface with chemical groups is also an important parameter for its efficiency to serve as virus inhibitor, as it determines the amount and strength of interactions formed between a virus and the inhibitor.<sup>[7]</sup> In this work, the hPG-based inhibitors were functionalized with sialic acids (SAs) and sulfate groups, which is motivated by the fact that many terminal glycans in mucins terminate either with a sialic acid (SA) or a sulfate group.<sup>[13]</sup> Furthermore, both groups are known attachment factors for various viruses:<sup>[18]</sup> SAs are, for example, involved in the attachment of influenza virus and many corona virus strains,<sup>[19,20]</sup> while viruses such as the vesicular stomatitis virus or herpes simplex virus bind to sulfated glycosaminoglycans.<sup>[21,22]</sup> As these two chemical groups already enable interaction with various virus species, we simplified the complex structure of mucins by regarding only these two terminal functional groups and thus by functionalizing the hPG scaffolds with SAs and sulfate residues as shown in **Figure 1b**.

Various values for the content of SA and sulfate groups in mucins have been reported in the literature, typically ranging between 4–20 wt% for sialic acid and 1.2–11.9 wt% for sulfates.<sup>[23,24]</sup> In this study, 5 mol% of the hydroxyl groups were substituted with SA and sulfate moieties (**Figure 1b**), respectively, which resulted in 15 wt% SA and 5 wt% sulfate (**Table 1**), being close to the middle of the ranges reported for mucins. In addition, for the 2600 kDa inhibitor two control polymers were prepared, carrying only one of the two moieties. All functionalized inhibitors show a negative zeta potential ranging from –22 to –27 mV (**Table 1**), which is caused by the incorporation the negatively charged sulfate and SA moieties. Both,



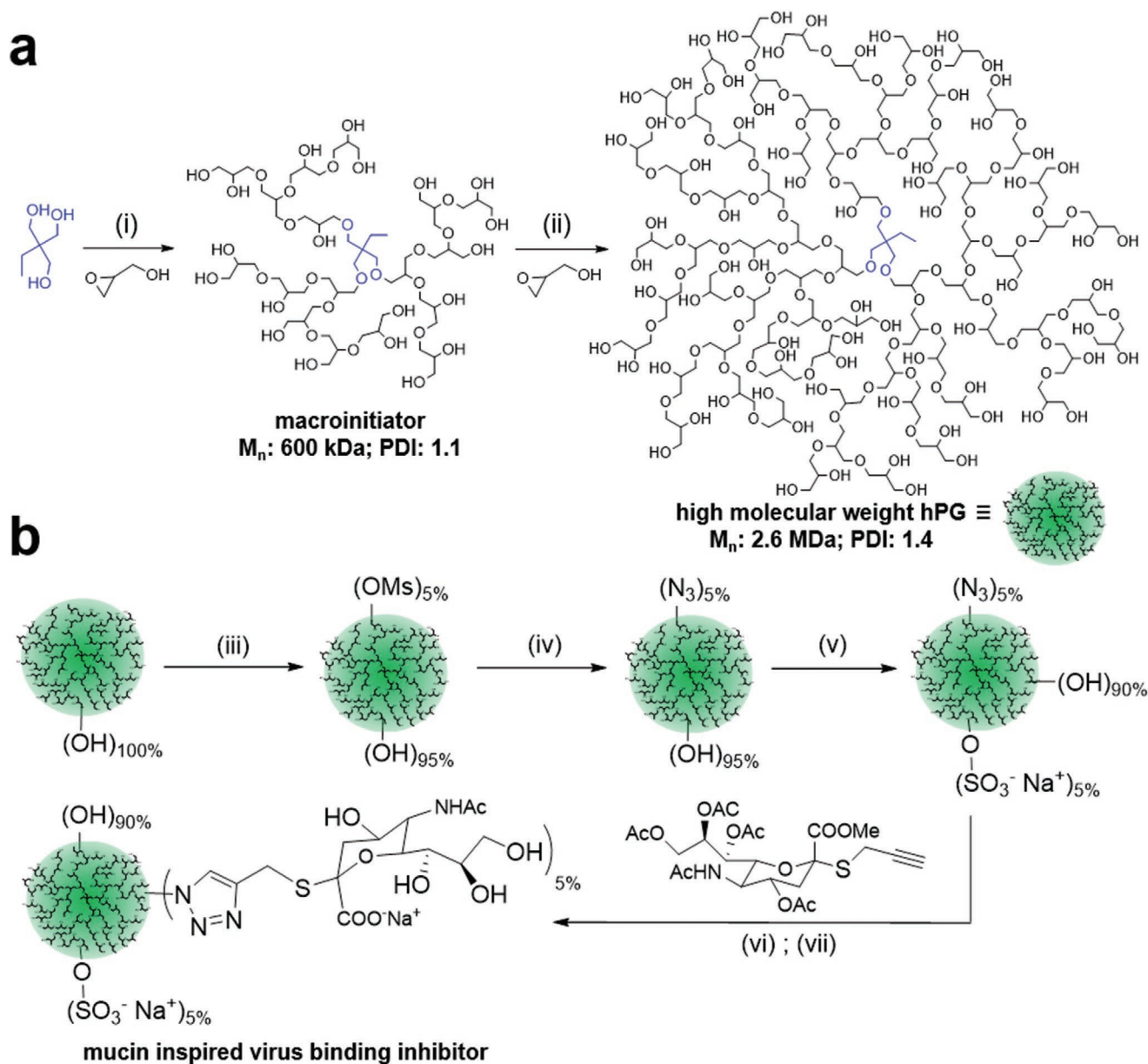


**Figure 1.** Synthesis of mucin-inspired virus binding (MuVib) inhibitors based on high-molecular weight hPG. a) Polymerization of the MDa hPG in two steps i) potassium methoxide in dry 1,4 dioxane at 95 °C and glycidol addition (0.5 mL h<sup>-1</sup>), ii) potassium hydride in dry DMF at 95 °C and glycidol addition (0.9 mL h<sup>-1</sup>). b) Functionalization of the MDa hPG, all reactions were carried out in dry DMF under argon atmosphere, iii) mesylation with mesyl chloride and triethylamine at room temperature for 20 h, iv) azidation using sodium azide at 80 °C for 20 h, v) sulfation with sulfur trioxide pyridine complex at 60 °C for 20 h, vi) copper-catalyzed alkyne-azide cycloaddition using copper sulfate pentahydrate, sodium ascorbate at 50 °C for 20 h, vii) deprotection with sodium hydroxide at room temperature for 2 h.

unfunctionalized and functionalized hPG polymers are highly water soluble. Furthermore, a predominantly spherical morphology of the MuVib inhibitor was verified using cryo-electron microscopy (see Figure S1, Supporting Information).

In a next step, we assessed the applicability of the synthesized inhibitors to hinder binding of viruses to cell membranes. These investigations were done using influenza A virus (IAV), being a highly important representative of the viruses that bind to cells via SAs. In particular, we employed the IAV strain X31 (H3N2), which is often used for assessing the efficiency of IAV

binding inhibition and thus allows for comparing the measured inhibition efficiency with literature values.<sup>[25–27]</sup> Interestingly, two membrane proteins are involved in this binding process of all IAVs: Hemagglutinin (HA) and neuraminidase (NA). Both proteins are able to interact with SAs, but while HA is known to promote IAV attachment to the cell membrane, NA is known to possess SA cleavage activity and is therefore believed to promote IAV egress (after the virus replication cycle has been completed).<sup>[28–30]</sup> The interplay between HA and NA is known to be important for completion of the virus life cycle and started

**Table 1.** Properties of synthesized virus binding inhibitors based on hPG.

	$d^a$	$\zeta$ -pot. <sup>b)</sup>	$\text{SO}_4^{c)}$		SA <sup>c)</sup>		$n_{\text{sulfate}}^d)$	$n_{\text{SA}}^d)$
	[nm]	[mV]	[mol%]	[wt%]	[mol%]	[wt%]	[-]	[-]
hPG <sub>10</sub> -SA-SO <sub>4</sub>	4.9 ± 4.2	-26.3 ± 0.9	7.2	6.2	7.0	19.3	7	7
hPG <sub>100</sub> -SA-SO <sub>4</sub>	12.0 ± 7.2	-22.4 ± 1.0	5.0	4.7	5.5	16.5	68	75
hPG <sub>500</sub> -SA-SO <sub>4</sub>	16.3 ± 9.7	-24.3 ± 0.8	3.9	3.7	5.7	17.1	268	392
hPG <sub>2600</sub> -SA-SO <sub>4</sub>	28.1 ± 17.1	-26.8 ± 1.1	5.0	4.7	5.6	16.7	1724	1931
hPG <sub>2600</sub> -SA	29.2 ± 15.3	-23.4 ± 0.5	-	-	5.6	17.7	-	1931
hPG <sub>2600</sub> -SO <sub>4</sub>	20.8 ± 11.4	-17.1 ± 0.9	4.3	5.3	-	-	1482	-
hPG <sub>2600</sub>	28.9 ± 14.9	9.5 ± 0.5	-	-	-	-	-	-

<sup>a)</sup>Hydrodynamic diameter obtained by DLS at sample concentration of 1 mg mL<sup>-1</sup> in PBS (10 mM, pH 7.4); <sup>b)</sup>Zeta-potential measurement in 10 mM phosphate buffer (pH 7.4); <sup>c)</sup>amount of converted hydroxyl groups in percent, determined by elemental analysis, degree of sialic acid based on fully conversion of azide moieties; <sup>d)</sup>calculated number of sialic acid and sulfate per polymer based on  $M_n$ .

to attract the focus of recent research.<sup>[31]</sup> According to Harris et al.<sup>[32]</sup> there are ≈300 copies of HA compared to 50 copies of NA in the membrane of the influenza A virus strain X31. To prevent NA-mediated cleavage of SAs at our synthesized binding inhibitor, a thioether bond was used to link the sialic acid to the polymer scaffold, which cannot be cleaved by NA.

In this study, the inhibitor performance was first investigated using the hemagglutination inhibition (HAI) assay (Figure S2, Supporting Information), which takes advantage of the feature that red blood cells become crosslinked upon interaction with IAVs (called hemagglutination).<sup>[33]</sup> By addition of virus binding inhibitors, the interaction between the virus and the membranes of red blood cells can be inhibited and the lowest inhibitor concentration at which no agglutination occurs anymore is defined as (HAI assay-derived) inhibition constant  $k_i$ . This assay is a well-established means for determining the amount of inhibitor (concentration) that has to be added in order to efficiently inhibit IAV binding to RBC membranes.<sup>[34]</sup> For the 10 and 100 kDa inhibitors we observed  $k_i$  values in the low  $\mu\text{M}$  range (Table 2), whereas the 500 kDa inhibitor approached the nM range and the most potent inhibition was exhibited by the 2600 kDa MuVib inhibitor (31  $\mu\text{M}$ ; 0.1  $\mu\text{g mL}^{-1}$ ), irrespective if this hPG was functionalized with SA and SO<sub>4</sub> or SA alone. The inhibitors lacking SA (i.e., the sulfated hPGs) showed no notable inhibition.

Although the HAI assay is often used to assess the inhibitory potential of compounds, it does not allow to directly probe the interaction of IAVs with their attachment factors or how

this interaction is altered by addition of inhibitors. In order to obtain such information, we extended a recently introduced virus-membrane binding assay based on total internal reflection fluorescence (TIRF) microscopy (Figure 2).<sup>[35]</sup> In this assay, a supported lipid bilayer (SLB), which is supplemented with the attachment factor of the virus of interest, is formed at a glass interface and the (transient) binding of fluorescently labeled viruses to the SLB is monitored using TIRF microscopy (Figure 2a). By choosing TIRF illumination, the excitation light hits the SLB-glass interface at the critical angle of total internal reflection, which generates an evanescent wave with a penetration depth of ≈100–150 nm,<sup>[36]</sup> so that fluorescence is only excited in very close vicinity of the SLB. Hence, to resolve fluorescently labeled viruses for an appreciable time period in TIRF microscopy, they have to be bound to the SLB, while unbound viruses are not visible.

For probing the IAV-SA interaction, a SLB based of POPC (96.2 wt%, 1-palmitoyl-2-oleoyl-glycero-3-phosphocholine) and DSPE-PEG2k (3.8 wt%, 1 mol%, 1,2-distearoyl-sn-glycero-3-phosphoethanolamine-*N*-[carboxy(polyethylene glycol)-2000] (sodium salt)) was supplemented with the ganglioside GD1a (2.5 wt%, 1 mol%), which presents SAs and thus provides the IAV attachment factor for the interaction studies. Although “human” IAV strains, such as X31 (H3N2), are known to prefer  $\alpha$ -2,6-linked over  $\alpha$ -2,3-linked SAs,<sup>[37]</sup> it has been shown that the corresponding difference in binding affinity is only minor (with HA-SA dissociation constants of  $K_d \approx 2$  and 3 mM for  $\alpha$ -2,6 and  $\alpha$ -2,3 linkage, respectively).<sup>[38]</sup> Despite the fact that GD1a presents  $\alpha$ -2,3-linked SAs, its use in IAV-SA interaction studies is therefore justified and is, for example, in line with the fact that HAI assays probing X31 binding inhibition have been done in the past with RBCs presenting any of the two linkages.<sup>[39,40]</sup>

In order to image the viruses, the envelope of the IAVs was labeled with the dye rhodamine octadecyl and TIRF microscopy was used to follow IAV attachment to/release from the SA-containing SLBs (Figure 2a). Single particle tracking (SPT) applied to the resulting TIRF microscopy videos allowed for tracking the motion of single viruses interacting with the SLB with high spatial accuracy (<15 nm) and subsequent application of the equilibrium fluctuation analysis (EFA)<sup>[41,42]</sup> yielded information on the rate of IAV attachment to the SLB, the IAV diffusion coefficient (which is a qualitative measure for the average

**Table 2.** Inhibitor performance in comparison of HAI and TIRF measurements.

	HAI $k_i$		TIRF IC <sub>50</sub>	
	[mol L <sup>-1</sup> ]	[ $\mu\text{g mL}^{-1}$ ]	[mol L <sup>-1</sup> ]	[ $\mu\text{g mL}^{-1}$ ]
hPG <sub>10</sub> -SA-SO <sub>4</sub>	$82 \times 10^{-6}$	1214	$2 \times 10^{-6}$	30
hPG <sub>100</sub> -SA-SO <sub>4</sub>	$5 \times 10^{-6}$	685	$0.6 \times 10^{-6}$	82
hPG <sub>500</sub> -SA-SO <sub>4</sub>	$50 \times 10^{-9}$	35	$0.4 \times 10^{-6}$	279
hPG <sub>2600</sub> -SA-SO <sub>4</sub>	$31 \times 10^{-12}$	0.1	$30 \times 10^{-12}$	0.1
hPG <sub>2600</sub> -SA	$31 \times 10^{-12}$	0.1	$3 \times 10^{-12}$	0.01
hPG <sub>2600</sub> -SO <sub>4</sub>	no inh.	no inh.	no inh.	no inh.



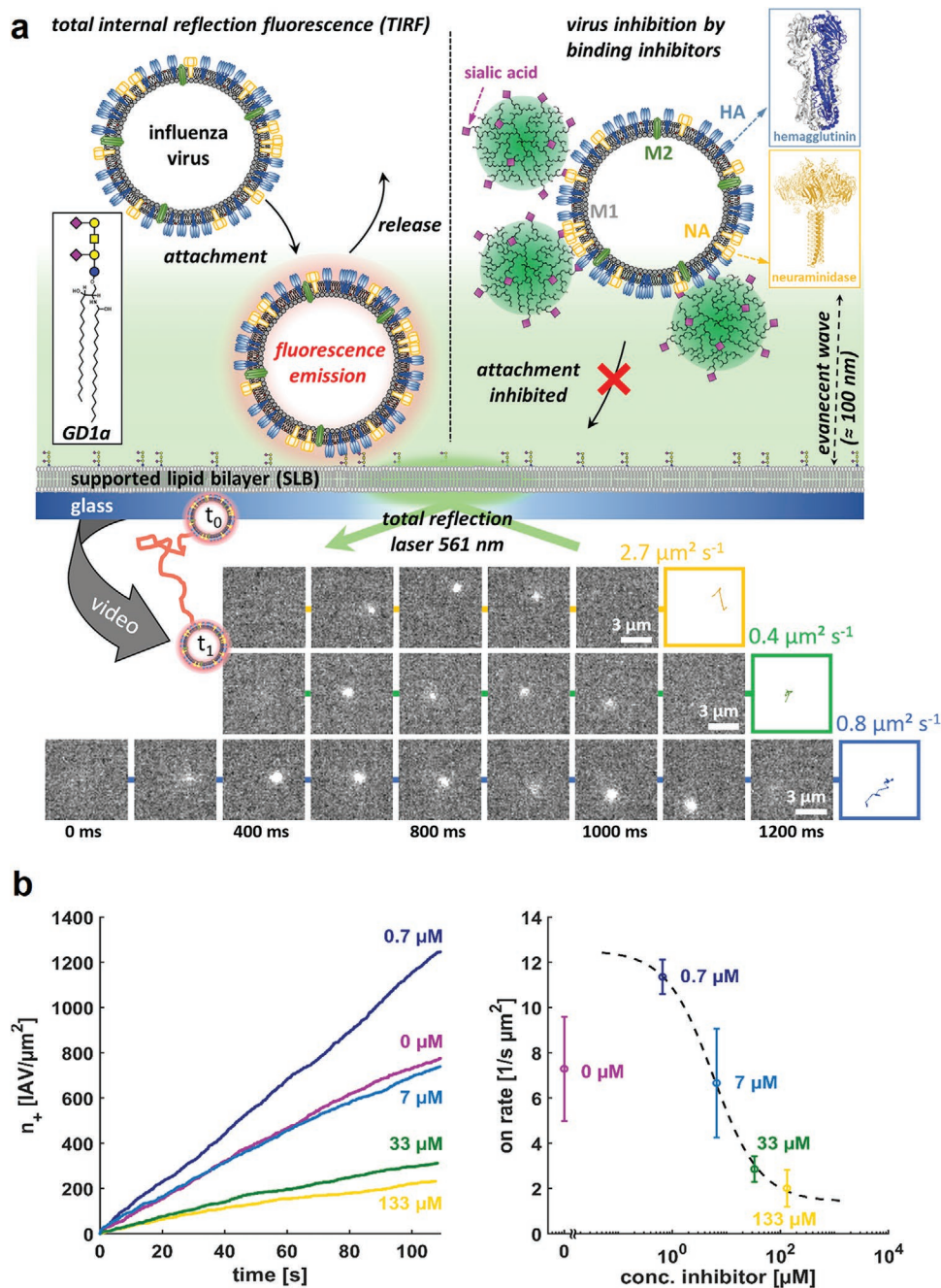


**Figure 2.** Experimental setup used to study IAV X31 binding to sialic acids (SAs) and the modification of this interaction upon addition of hPG inhibitors. a) Supported lipid bilayers (SLBs) containing the sialic acid-presenting ganglioside GD1a were used as artificial cell membranes. Fluorescently labeled IAVs (R18 dye incorporated in the virus envelope) bind to sialic acids exposed by the SLB, a process which is followed by TIRF imaging (always performed at room temperature; 20 °C). b) The cumulative number of newly arriving IAVs, as calculated using the EFA procedure, increases linearly with time. The slope of these traces is proportional to the rate of IAV attachment to the SA-containing SLB and allows for determining IAV binding inhibition upon addition of hPG inhibitors. The plot shows a representative example using the inhibitor hPG<sub>10</sub>-SA-SO<sub>4</sub>.

number of attachment factors bound by the tracked IAV), and the IAV residence time distribution as described previously.<sup>[35]</sup>

As the inhibitors were designed to prevent IAV binding to membranes, it is straightforward to assess their inhibition efficiency by quantifying the change of the rate of IAV attachment to the SA-presenting SLB as function of the inhibitor concentration (Figure 2b). According to the EFA procedure,<sup>[41,42]</sup> this rate

is extracted by calculating, for each recorded TIRF movie separately, the total number of IAVs that have been newly bound to the SLB since the beginning of the TIRF movie. Under equilibrium conditions (i.e., if SLB-bound and solution-dissolved viruses are in thermodynamic equilibrium) this number, the so-called cumulative number of newly arising viruses, increases linearly with measurement time, and the slope of this function

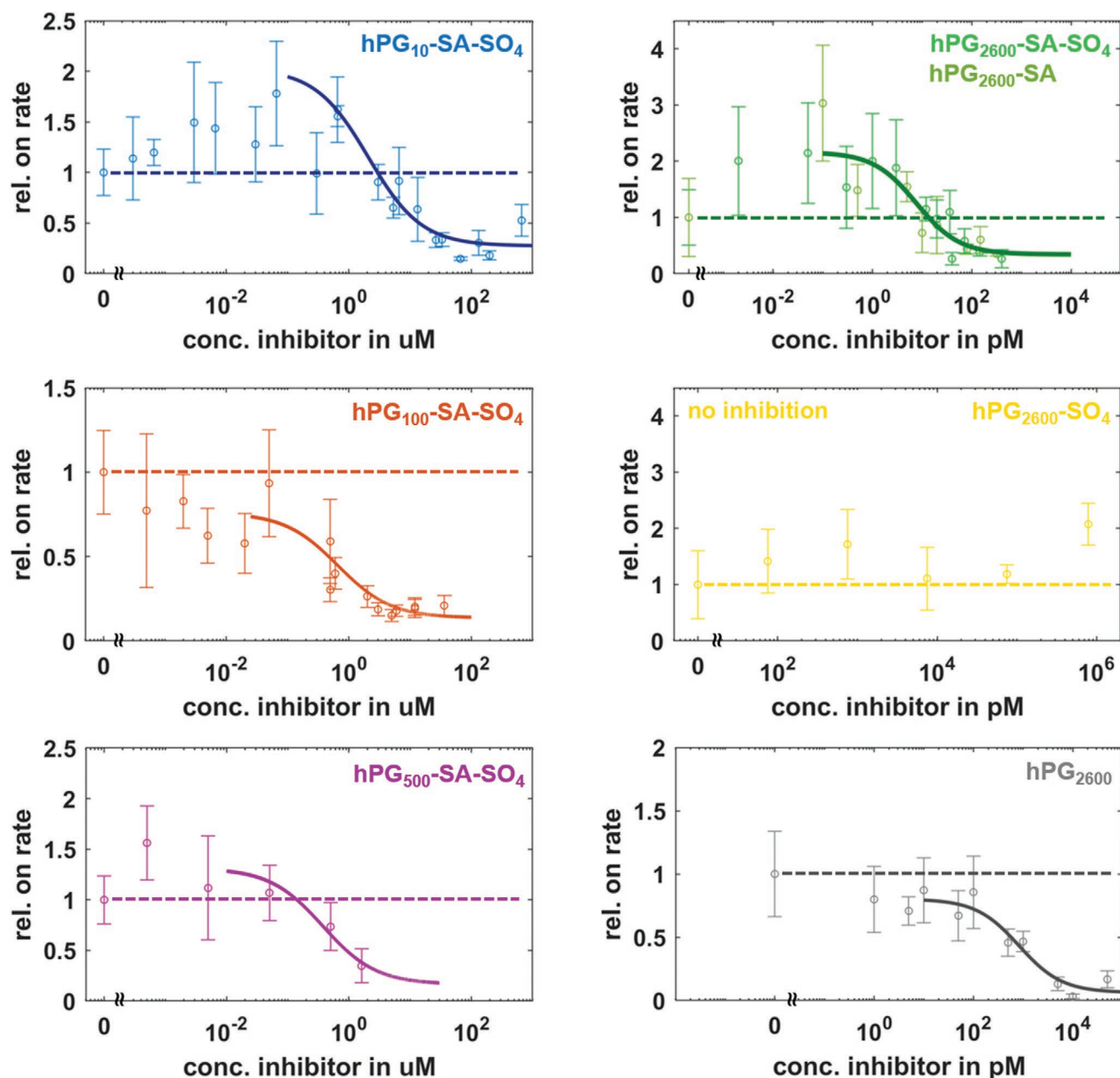


**Figure 3.** Change in IAV attachment rates upon hPG inhibitor (10, 100, 500, 2600 kDa) addition. Shown is the relative on-rate, which was calculated by normalizing the IAV attachment rate at a given hPG inhibitor concentration by the IAV attachment rate in absence of the inhibitor (i.e., at 0 m inhibitor concentration). Dashed lines are fixed to a relative on-rate value of one and thus show, if the rate of IAV attachment increases ( $>1$ ) or decreases ( $<1$ ) upon inhibitor addition. Surprisingly, both cases are observed for all SA-presenting inhibitors (except for the 100 kDa compound), generating a biphasic behavior in IAV binding inhibitor (see main text for details). Solid lines are fits of a Langmuir-type inhibition model to the data, allowing to determine the  $IC_{50}$  value of the inhibitors. Symbols indicate average values  $\pm$  standard deviation of at least five measurements.

corresponds to the IAV attachment rate for the area probed.<sup>[41,42]</sup> Addition of the inhibitors changed the slope of the cumulative number of newly arising IAVs, which indicates a change of the rate of IAV attachment to the SLB caused by the presence of the inhibitors (Figure 2b). Strong inhibition of IAV binding is reflected by a strong decrease in the IAV attachment rate, so that the change in the IAV attachment rate (with respect to its value in absence of any inhibitor) is indicative for the inhibition efficiency.<sup>[22]</sup> Hence, in the following all IAV attachment rates

will be normalized by the value in absence of any inhibitor, which is denoted as relative on-rate in this work.

As expected for binding inhibitors, all SA-presenting hPGs showed a decrease in the relative on-rate for a sufficiently large inhibitor concentration (Figure 3). Fitting a Langmuir-type inhibition curve to the relative on-rate in this concentration range allowed for determining the inhibitor concentration, at which the IAV binding rate to the SLB has been reduced by 50% (the so-called  $IC_{50}$  value; Table 2). While the 10 to 500 kDa

hPG inhibitors showed  $IC_{50}$  values in the  $\mu\text{M}$  molar range, the 2600 kDa hPG inhibitors reached  $\text{pM}$  values. This impressive value is not only due to the high molecular weight of these large inhibitors, but also by an improved inhibition potential as indicated when comparing the  $IC_{50}$  values expressed in mass concentrations (Table 2); compared to the smaller inhibitors, a virus inhibition is achieved for the 2600 kDa hPGs at a three order of magnitudes lower mass concentration, which is indicative for a multivalency-based enhancement of the inhibition. In addition, both SA-functionalized 2600 kDa hPGs showed comparable inhibition efficiency, that is, hPGs with SA and sulfate functionalization is not notably more effective than the inhibitor with just SA, while the one lacking SA but carrying sulfates did not show any IAV inhibition. Both observations are expected, as IAVs bind with much higher affinity to sialic acids than to sulfates, so that the interaction is dominated by sialic acids for the SA-containing inhibitors and negligible (for the inhibitor concentrations investigated) if only sulfates are present on the inhibitor.

As inhibition is only observed for inhibitors presenting SAs (which are known to be the IAV attachment factor) and as SA-presenting inhibitors (see Table 1) as well as SA-presenting bilayers are negatively charged,<sup>[43]</sup> IAV inhibition must be due to binding of the hPG-based inhibitors to the viruses. This conclusion is in line with the observations of related SA-presenting inhibitors and the measurement of size distributions of IAVs in presence and absence of the inhibitor (Figure S3, Supporting Information).<sup>[25]</sup>

In contrast, the non-functionalized MDa hPG also showed inhibition in the TIRF-based assay with an apparent  $IC_{50}$  value of  $\approx 1000 \text{ pM}$ , while no inhibition was observed in the HAI assay. We attribute this behavior to the slightly positive zeta potential (Table S1, Supporting Information) of this polymer, which promotes its binding to negatively charged sialic acid groups presented by the SLB and thus blocks the interaction between IAVs and the SLB by steric depletion of the attachment factors. This view is confirmed by the lack of any inhibition potential of  $\text{hPG}_{2600}\text{-SO}_4$ , which possesses, as all functionalized hPGs, a negative surface charge and is therefore not able to bind to the negatively charged SLB. A reason for its positive zeta potential of the non-functionalized MDa hPG could be the incorporation of salt ions although the polymer was excessively dialyzed against water. A treatment of the polymer solution with cation exchanger before the measurement of the zeta potential did not change the slightly positive zeta potential result. All functionalized hPGs showed the expected zeta potential, which verifies the measurement principle.

Nevertheless, for all SA-presenting inhibitors the results on IAV binding inhibition obtained using the HAI- or TIRF-based assays are qualitatively in good agreement (Table 2), although the TIRF-based assay reports in general slightly smaller  $IC_{50}$  values than the HAI-assay. Both assays show that the  $IC_{50}$  values generally decrease with increasing inhibitor size, that is, that the inhibitors become more potent for increasing size of its scaffold. This trend is in fact expected based on the theoretical considerations of Vonnemann et al.,<sup>[10]</sup> who show based on geometrical considerations that an optimal size for binding inhibitors exists. These considerations show that increasing the inhibitor size also increases the contact area between inhibitor

and virus and thus the virus-inhibitor interaction. Nevertheless, as the inhibitor mass also scales with the third power of the inhibitor size, this increase in inhibitor size also increases the applied mass concentration of the inhibitor, which partially cancels the enhancement caused by the increase in binding strength. Hence, there exists an optimum inhibitor size at which the lowest (total) mass of inhibitor is required for inhibition and which is, according to Vonnemann et al.<sup>[10]</sup> approximately one third of the size of the virus to be inhibited. As IAV X31 typically shows spatial extensions ranging between 80 and 120 nm, an optimum in binding inhibition is expected for inhibitor diameters on the order of 30 nm, which is realized by the MuVib inhibitor ( $\text{hPG}_{2600}\text{-SA-SO}_4$ , Table 1). In this context, the decrease of the  $IC_{50}$  value with increasing inhibitor size qualitatively matches to the predictions of Vonnemann et al.<sup>[10]</sup> A test, if the 2600 kDa MuVib inhibitor indeed achieves optimum inhibition efficiencies was, however, not possible, as this would have required to synthesize notably larger hPG scaffolds, which was not achievable in this study. A complementary approach to achieve related inhibitors with larger sizes is nanoprecipitation, in which smaller hPGs are crosslinked to form nanogels. For example, Bhatia et al. recently introduced hPG-based nanogel inhibitors with sizes of  $\approx 250 \text{ nm}$  and achieved  $IC_{50}$  values of about  $30 \mu\text{g mL}^{-1}$ .<sup>[25]</sup> This performance is two to three magnitudes lower than the one of the 2600 kDa MuVib inhibitor and indicates that the optimum inhibitor size for IAV binding inhibition is in between of 30 and 250 nm.

Nevertheless, while the HAI assay provides a rather binary readout (i.e., if the inhibitor concentration is sufficient to inhibit agglutination of red blood cells),<sup>[33]</sup> the changes in the IAV attachment rate measured by TIRF showed biphasic progression: Starting at small inhibitor concentrations ( $\ll IC_{50}$ ), the attachment rates first increased with increasing inhibitor concentration, followed by a saturation and a strong decrease at large inhibitor concentrations ( $\approx IC_{50}$ ). This surprising behavior indicated that the SA-functionalized hPG inhibitors promoted IAV attachment at relatively low inhibitor concentrations, while IAV binding inhibition was observed for sufficiently large inhibitor concentrations. The first phase (increase in IAV attachment rate) is not resolvable in the HAI-assay, as the IAV concentration is chosen such that IAV-induced agglutination is observed in absence of the inhibitor. This means that an increase in the IAV attachment rate to the cell membranes is not resolved by HAI, as in absence of inhibitors the IAV attachment rate is already sufficiently large to achieve agglutination.

This biphasic behavior, which was observed for all inhibitors except for  $\text{hPG}_{100}\text{-SA-SO}_4$  and which first increases the IAV binding rate to membranes at low inhibitor concentrations until a decrease is observed at large concentrations, was unexpected. Nevertheless, the observed increase in IAV attachment rate resembles changes to the IAV binding properties observed upon application of neuraminidase inhibitors.<sup>[35]</sup> Hence, the biphasic behavior suggests that at relatively low concentrations the inhibitors bind first to the NA and therefore act as NA inhibitors, while binding to HA and thus binding inhibition requires higher inhibitor concentrations. This interpretation is consistent with measurements on the affinity of the envelope proteins to sialosides,<sup>[44,45]</sup> showing that the dissociation constant  $K_d$  of the NA-SA interaction is 3 order of magnitude



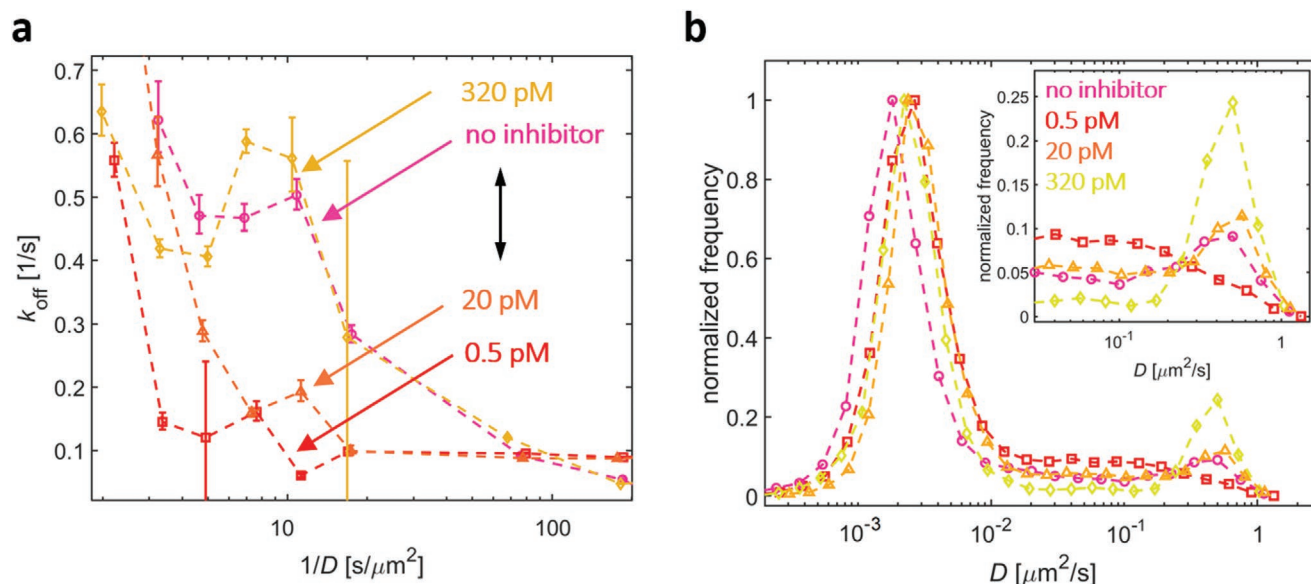


**Figure 4.** a) Changes of the IAV off-rate and b) diffusion coefficient distribution upon addition of the hPG<sub>2600</sub>-SA-SO<sub>4</sub> MuVib inhibitor. The biphasic binding behavior is also observed in these distribution, as addition of small amounts of the inhibitor ( $\leq 20$  pM) leads to a decrease in the off-rate distribution and a shift of the diffusion coefficient distribution from large to small values (indicating an increase in average binding valency), while addition of larger amounts of the inhibitor ( $>20$  pM) restores the off-rate distribution and shifts the diffusion coefficient distribution from small to large values (indicating an decrease in average binding valency).

smaller than the one of the HA–SA interaction ( $\approx \mu\text{M}$  vs.  $\approx \text{mM}$ , respectively) and supporting the hypothesis that also the inhibitors exhibit higher affinity (lower  $K_d$  value) towards NA than HA. Furthermore, evidence is accumulating that NA also contributes to the process of IAV binding to membranes.<sup>[33,46]</sup>

If the hypothesis is correct that the inhibitors bind preferentially to NA at relatively low inhibitor concentrations and to HA at sufficiently large ones, one would expect to see inhibitor concentration-dependent changes of the IAV off-rate and valency distribution, as both IAV binding properties strongly depend on the functional balance between HA and NA.<sup>[35]</sup> In order to test this hypothesis, we extracted IAV off-rate and valency distributions from the TIRF measurements as recently described.<sup>[35]</sup> In brief, here we make use of the fact that the diffusion coefficient of SLB-bound IAVs,  $D$ , decreases with increasing valency (=number of bound GD1a gangliosides), so that the changes to the IAV valency distribution also induce changes to the distribution of IAV diffusion coefficients. Although the exact relationship connecting IAV valency and diffusion coefficient has not yet been resolved, all theoretical models indicate that both properties are connected by a monotonously decreasing function, that is, large values of the diffusion coefficient correspond to a small value of the average valency and vice versa.<sup>[47]</sup> Furthermore, the measurement of the IAV diffusion coefficient also allows to deconvolute the IAV residence time distribution from valency effects, yielding valency-resolved off-rate distributions.<sup>[35]</sup>

In absence of any inhibitor (open circles, **Figure 4a**), the observed off-rate distribution is dominated by a decrease for increasing apparent average valency  $D^{-1}$ , but also shows a peak structure, leading to elevated off-rates at intermediate average valencies ( $D^{-1} \approx 8 \text{ s } \mu\text{m}^{-2}$ ). The presence of a peak structure matches to previous observations,<sup>[35]</sup> in which it is shown that

this structure is caused by the opposing functionalities of HA and NA and vanishes upon application of NA inhibitors such as zanamivir. Furthermore, the addition of zanamivir also increased the rate of IAV attachment and both effects together yielded a strong increase in the number of bound IAVs. Interestingly, exactly the same behavior is observed here at relatively low inhibitor concentrations, at which the relative IAV on-rate increases (Figure 3) and the IAV off-rate decreases with increasing inhibitor concentration (open triangles and squares, Figure 4a). Hence, at relatively low concentrations, the inhibitors behave like a NA inhibitor with respect to the induced changes in IAV attachment and off-rate distribution.

Additional evidence is provided by the diffusion coefficient distributions (Figure 4b), which showed a shift from large to small values upon addition of small amounts of the inhibitor ( $\ll \text{IC}_{50}$ ) and a shift from small to large diffusion coefficient values upon addition of large amounts of the inhibitor ( $\gg \text{IC}_{50}$ ). As the diffusion coefficient  $D$  is indicative for the average valency of the IAV-SA interaction, these changes indicate that the addition of inhibitors modifies the IAV valency distribution. In particular, the shift from large to small  $D$ -values observed for inhibitor concentrations below  $\text{IC}_{50}$  indicates an increase of the average binding valency (“NA-like inhibition”), while the opposite behavior is observed above  $\text{IC}_{50}$  and thus indicates a decrease in average binding valency (“HA inhibition”). There is, however, a lower limit for the valency, below which the interaction of the IAV to the membrane becomes too small to maintain IAV binding to the membrane. This limit is reached for  $D$ -values exceeding  $\approx 1 \mu\text{m}^2 \text{ s}^{-1}$ , so that the  $D$ -distributions exhibit an edge at  $\approx 1 \mu\text{m}^2 \text{ s}^{-1}$  and, in connection with the transfer of events from small to large  $D$ -values, a peak-like structure, which raises with increasing inhibitor concentration added.

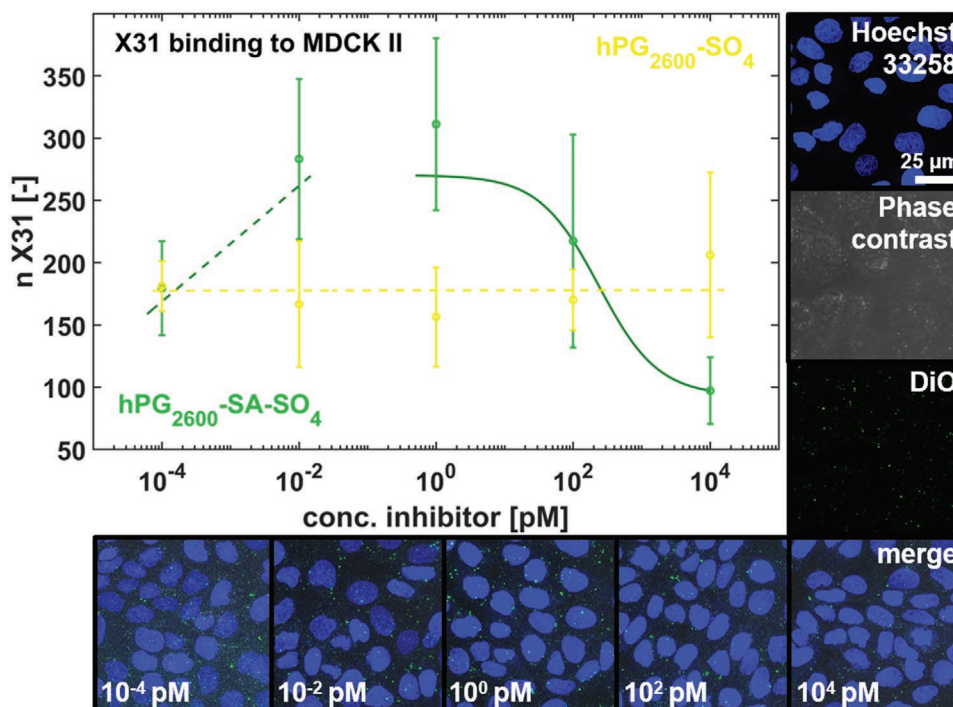


**Figure 5.** Inhibition of IAV X31 binding to MDCK II cells upon addition of the hPG<sub>2600</sub>-SA-SO<sub>4</sub> MuVib inhibitor (green symbols) and of the negative control hPG<sub>2600</sub>-SO<sub>4</sub> (yellow symbol). The cell-based assay also shows a biphasic change of IAV binding inhibition as observed in the TIRF-based binding assay. IAVs were labeled with DiO (green structures in the cell images), while the MDCK II cells were labeled using Hoechst 33 258 (blue structures). Symbols indicate average values  $\pm$  standard deviation of four measurements. Dashed lines are to guide the eye.

Nevertheless, in order to probe, if the phenomenon of increased IAV attachment rates at small inhibitor concentrations ( $\ll$ IC<sub>50</sub>) can also be observed for native cell plasma membranes, we further investigated the IAV binding to MDCK-II cells, which are known to expose  $\alpha$ -2,6-linked and  $\alpha$ -2,3-linked SAs and are an established cell line for investigating IAV binding to and infection of cells.<sup>[48]</sup> Here, labelled IAVs were mixed with different concentration of the inhibitor hPG<sub>2600</sub>-SA-SO<sub>4</sub> at room temperature for 45 min. Afterwards, the virus-inhibitor mixture was incubated with MDCK-II cells for 2 h on ice. Non-bound IAVs were removed by washing twice with PBS buffer, while bound IAVs remained at the cell surface. Using confocal laser scanning microscopy Z-wide images of the cell layer were taken and stacked to visualize all viruses at the cell surface, followed by quantifying the number of bound viruses using ImageJ.<sup>[49]</sup> The number of MDCK-II cell-bound IAVs (**Figure 5**) showed the same dependence of the inhibitor concentration as the relative on-rate determined using TIRF microscopy (Figure 3), verifying an increased IAV attachment at low concentrations and a decrease in IAV attachment at higher concentrations. The sulfated derivative (hPG<sub>2600</sub>-SO<sub>4</sub>) was used as negative control and showed no impact on the IAV binding. Hence, the biphasic change in the IAV binding behavior upon inhibitor addition is observed for IAVs interacting with attachment factor-equipped SLBs as well as with cell membranes, which further supports our view that these inhibitors behave as NA-like inhibitors at low inhibitor concentrations and as HA inhibitors at high concentrations. Furthermore, as MDCK-II cells present  $\alpha$ -2,6-linked as well as  $\alpha$ -2,3-linked SAs, obtaining

the same inhibition curve as in the TIRF assay post-validates that GD1a is a suitable attachment factor for probing the interactions between IAV X31 and GD1a.

### 3. Conclusions

In this study, hyperbranched polyglycerol (hPG)-based virus binding inhibitors have been synthesized, the size and functionalization of which have been inspired from mucins. The resulting mucin-inspired virus binding (MuVib) inhibitor was based on a 2.6 MDa hPG core that was functionalized with sialic acids and sulfate groups (5 mol% of the hPGs OH groups, respectively). In addition, hPG-based inhibitors having the same functionalization but lower molecular weights (ranging between 10 and 2600 kDa) were synthesized as well, which allowed to probe the impact of the inhibitor size on its inhibition efficiency. This efficiency of the synthesized compounds in inhibiting the binding of a common respiratory virus, a H3N2 influenza A virus (IAV), was assessed using a cell binding and the hemagglutination inhibition assay, both of which provide information about the minimum inhibitor concentration that needed to inhibit IAV binding to membranes. Furthermore, a recently developed TIRF-based assay was employed to quantify, how inhibitor addition modified the multivalent interaction arising between IAVs and their native attachment factor, sialic acids.

Surprisingly, the inhibition of IAV binding to membranes showed a biphasic behavior for increasing inhibitor concentrations: At relatively low inhibitor concentrations, the IAV binding

first increased with increasing inhibitor concentrations, followed by a second regime at higher inhibitor concentrations, at which the expected decrease in IAV binding was observed for increasing inhibitor concentrations. The results of the TIRF-based assay and the cell binding assay indicate that the inhibitors bind at low inhibitor concentrations preferentially to the IAV envelope protein neuraminidase (NA), leading to an enhancement of the IAV binding to lipid membranes, while at larger inhibitor concentrations, it binds additionally to another IAV envelope protein, hemagglutinin (HA), causing IAV binding inhibition. Potent inhibition of IAV binding (HA inhibition) by the 2600 kDa MuVib inhibitor is observed in all these assays already at  $\mu\text{M}$  concentrations, while decreasing the molecular weight of the inhibitors decreased their inhibition efficiency (increase in their  $\text{IC}_{50}$  value), which is in qualitative agreement with the prediction by a recent study of Vonnemann et al.<sup>[10]</sup>

#### 4. Experimental Section

**Synthesis of High-Molecular Weight hPG:** The synthesis of the MDa hPG was performed in two steps,<sup>[16]</sup> as previous investigations showed that using one step approaches the molecular weight of hPGs can be increased to only 800–900 kDa.<sup>[17,50]</sup> This limitation has been attributed in the past to the decrease in the concentration of active alkoxide units on polyglycerol, which are key elements to chain/branching and propagation of the hPG systems.<sup>[51]</sup>

First, a macroinitiator was synthesized in a heterogenous reaction mixture in dioxane. Dry trimethylolpropane (120 mg, 0.89 mmol, 1.0 eq.) was partially deprotonated (30% OH) with potassium methoxide (67  $\mu\text{L}$ , 0.27 mmol, 0.3 equiv., 25% in methanol) in argon atmosphere at 60 °C for 30 min. After the addition of 24 mL dioxane (dry) the turbid mixture was heated to 100 °C. Glycidol (12 mL, 0.18 mol, 201 equiv.) was slowly added (0.5 mL  $\text{h}^{-1}$ ) via syringe pump into the reaction mixture. The polymer was purified by removing the dioxane, precipitation as methanolic solution in acetone and dialysis against water in regenerated cellulose membrane (10 kDa MWCO). The resulted hPG (Mn: 600 kDa,  $\bar{D}$  1.1) was obtained with a yield of 93.6 %.

In the second step, this hPG was used as macroinitiator to grow the polymer further. 2.5 g (0.034 mol, total OH groups) of the lyophilized polymer was dissolved in dry DMF (35 mL). The polymer was partially deprotonated with the addition of potassium hydride in oil (30 wt%) (80  $\mu\text{g}$ , 272  $\mu\text{L}$ , 2.0  $\mu\text{mol}$ ). The temperature was increased to 100 °C and glycidol (25 mL, 0.37 mol) were added with a rate of 0.9 mL  $\text{h}^{-1}$ . After precipitation in acetone and dialysis against water in regenerated cellulose membrane (50 kDa MWCO) the resulted molecular weight was 2.6 MDa with a  $\bar{D}$  of 1.4.

**Mesylation and Azidation:** Both reactions were performed sequentially in one pot. 1300 mg hPG (2.6 MDa) (0.88 mol OH to be functionalized) was dissolved in dry DMF (18 mL). The mesylation was done with methanesulfonyl chloride (201 mg, 1.8 mmol, 2.0 eq.) in the presence of triethyl amine (306  $\mu\text{L}$ , 2.2 mmol, 2.5 mol eq.) at room temperature for 16 h. Afterwards the azidation was directly performed by the addition of sodium azide (456 mg, 7.0 mmol, 8 equiv.) at 80 °C for 20 h under argon atmosphere. Purification was done by dialysis against water (2 kDa MWCO, benzoylated). The product was analyzed by  $^1\text{H}$  NMR and elemental analysis to determine the amount of introduced azide groups (see Figure S5, Supporting Information).

**Sulfation:** The azidated hPG (400 mg, 0.27 mmol OH to be functionalized, 1.0 equiv.) was sulfated using sulfur trioxide pyridine complex (55.9 mg, 0.4 mmol, 1.3 equiv.) in dry DMF (12 mL) at 60 °C for 20 h under argon atmosphere. After the reaction time was over the pH value was increased to pH 10 by the addition of sodium hydroxide solution (0.3 mol  $\text{L}^{-1}$ ). The product was dialyzed against sodium hydroxide solution (0.3 mol  $\text{L}^{-1}$ ), 10 wt% NaCl and water. The yield of the

sulfation was analyzed by elemental analysis. Further, a  $^1\text{H}$  NMR of the product was performed (see Figure S6, Supporting Information).

**Click Protected Propagylated Sialic Acid by CuAAC:** The sulfated polymer hPG<sub>2600</sub>-N<sub>3</sub>-SO<sub>4</sub> (150 mg, 0.11 mmol OH to be functionalized, 1.0 equiv.) was mixed with acetyl protected propagylated sialic acid (72.9 mg, 1.3 mmol, 1.2 equiv.) in DMF. Copper sulfate pentahydrate (11.1 mg, 0.04 mmol, 0.4 equiv.) and sodium-L-ascorbate (88.3 mg, 0.4 mmol, 4 equiv.) were dissolved separately in a small amount of water and combined afterwards. The solution was transferred to the polymer solution. The reaction was performed at 50 °C for 20 under argon atmosphere. Infrared spectroscopy indicated complete conversion by the disappearance of the azide band (2100  $\text{cm}^{-1}$ ; see Figure S7, Supporting Information) within the resolution limit of the instrument (determined by multiple repetitions of the measurement and calculation of the standard error). Hence, it is reasonable to assume that the functional degree of conjugated sialic acid is almost the same as the initial degree of azidation ( $\approx 5\text{--}7\%$ ). The pH value was increased to pH 10 with sodium hydroxide solution (2 mol  $\text{L}^{-1}$ ) to cleave the acetyl protection of the sialic acid within 2 h. EDTA disodium salt (14.0 mg, 0.04 mmol, 0.4 equiv.) was added to improve the removal of copper ions during dialysis against water. The purified polymer was analyzed by  $^1\text{H}$  NMR (see Figure S9, Supporting Information) and elemental analysis.

The synthesized virus binding inhibitors were characterized in regard to size with dynamic light scattering (DLS) and in respect of surface charge by zeta potential measurements.

**Dynamic Light Scattering:** The hydrodynamic diameter was measured by dynamic light scattering at a concentration of 1 mg  $\text{mL}^{-1}$  in PBS buffer using Zetasizer Nano series ( $\lambda = 532\text{ nm}$ ) from Malvern Panalytical (Kassel, Germany). Disposable cuvettes (ZEN0040) from Brand (Wertheim, Germany) out of polystyrene were used. Before the measurement all samples were filtered through a 0.2  $\mu\text{m}$  Minisart RC 15 syringe filter from Satorius (Göttingen, Germany). Temperature equilibration was done for 1 min at 25 °C. The measurements were performed for ten scans each 15 s in back scattering mode (173°). The stated values result from at least three measurements.

**Zeta-Potential:** The surface charge was investigated by zeta-potential measurement with Zetasizer Nano series ( $\lambda = 532\text{ nm}$ ) using folded capillary zeta cells (DTS 1070) from Malvern Panalytical (Kassel, Germany). The sample concentration was 1 mg  $\text{mL}^{-1}$  in 10 mm phosphate buffer solution (0.411 g  $\text{L}^{-1}$  Na<sub>2</sub>HPO<sub>4</sub>, 0.178 g  $\text{L}^{-1}$  KH<sub>2</sub>PO<sub>4</sub>, pH 7.4). All samples were filtered through a 0.2  $\mu\text{m}$  Minisart RC 15 syringe filter from Satorius (Göttingen, Germany). Five measurements with ten scans (each 15 s) were done to obtain the zeta potential based on the Smoluchowski model.

The virus binding performance was investigated by two independent methods: hemagglutination inhibition (HAI) assay and total internal reflection fluorescence (TIRF) microscopy.

**Hemagglutination Inhibition Assay:** The inhibitors were two-fold diluted with PBS in a v-shaped microtiter plate. Afterwards, 2 HA X31 virus were transferred to each inhibitor dilution. After 30 min incubation time at room temperature 50  $\mu\text{L}$  of 1% chicken RBC solution (Robert Koch-Institute, Berlin) was added to each well. Then, it was incubated for 60 min at room temperature before the read out was done. The lowest concentration where the sedimentation of red blood cells was still inhibited by hemagglutination represents the inhibitor constant  $k_i$  (see Figure S2, Supporting Information).

**Total Internal Reflection Fluorescent Microscopy:** Single virus tracking was done on a supported lipid bilayer (SLB), which represents the cell surface. IAV bind in a multivalent fashion to incorporated GD1a gangliosides (1 mol%). Extruded vesicles out of POPC and 1 mol% GD1a were exposed in an aqueous solution (0.33 mg  $\text{mL}^{-1}$ ) on a cleaned glass, absorb, deform, and form a cohesive supported lipid bilayer by rupturing on the glass surface. Sialic acids on the GD1a are the natural target of IAVs. After 10 min excess vesicles were removed by washing with PBS buffer. Then, IAV solution with or without containing binding inhibitor was injected. Through excitation in TIRF mode, an evanescent light beam (white light + m-cherry filter) penetrates approximately 100 nm in the solution and reaches therefore just bound viruses ( $\approx 100\text{ nm}$ ) on



the membrane. This ensures that rhodamine (R18) labeled viruses in the evanescent region get excited and emit light, non-bound labeled virus in the solution are not visible. Videos with 0.11 fps were taken to visualize the virus attachment, diffusion and detachment on the GD1a receptor containing SLB. The videos were analyzed by homemade MATLAB scripts using equilibrium fluctuation analysis (EFA).

**IAV Binding to MDCK-II Cells:** The cultured MDCK II cells were seeded in 8-well confocal slides and cultured for 1–2 days till confluency. 100  $\mu$ L X31 solution (protein content: 0.36mg mL<sup>-1</sup>, 1.1  $\times$  10<sup>11</sup> particles mL<sup>-1</sup>) was incubated with 2  $\mu$ L of 20  $\mu$ M DiO (in ethanol, D4929 in Merck, Darmstadt, Germany) for 30 min in dark. The free dyes were removed by spin column then. A mixture of 90  $\mu$ L inhibitor (in PBS) and 10  $\mu$ L labelled virus was added after 45 min at room temperature on the cell layer (culture medium was removed before by washing with PBS twice). After an incubation for 2 h on ice, non-binding viruses were removed by washing twice with PBS. The cell nucleus was labelled with Hoechst 33258 and the cells fixed with 4% paraformaldehyde. Finally, Z-wide images were taken with confocal laser scanning microscopy from the whole cell layer (30 images, step size 0.4  $\mu$ m). The number of binding viruses was determined from the stacked images using ImageJ.

## Supporting Information

Supporting Information is available from the Wiley Online Library or from the author.

## Acknowledgements

This work was supported by the German Research Foundation (BL1514/1-1 and project A6 within the CRC 765) and by the Focus Area NanoScale (Freie Universität Berlin). The authors thank the core facility BioSupraMol and the Macromolecular Hub (CBR) for the use of their research facilities. J.N.K. acknowledges the funding by Canadian Institutes of Health Research (CIHR), Natural Sciences and Engineering Council of Canada (NSERC) and Canada Foundation for Innovation (CFI). J.N.K. holds a Career Investigator Scholar award from the Michael Smith Foundation for Health Research (MSFHR). S.A. acknowledges a MSFHR postdoctoral fellowship.

Open access funding enabled and organized by Projekt DEAL.

## Conflict of Interest

The authors declare no conflict of interest.

## Keywords

hyperbranched polyglycerol, influenza A viruses, single particle tracking, TIRF microscopy, virus binding inhibition

Received: July 30, 2020  
Revised: September 28, 2020  
Published online:

- [1] M. Hoffmann, H. Kleine-Weber, S. Schroeder, N. Kruger, T. Herrler, S. Erichsen, T. S. Schiergens, G. Herrler, N. H. Wu, A. Nitsche, M. A. Muller, C. Drosten, S. Pohlmann, *Cell* **2020**, 181, 271.  
[2] C. V. Ventura, M. Maia, V. Bravo-Filho, A. L. Góis, R. Belfort, *Lancet* **2016**, 387, 228.  
[3] G. Neumann, T. Noda, Y. Kawaoka, *Nature* **2009**, 459, 931.  
[4] E. De Clercq, G. Li, *Clin. Microbiol. Rev.* **2016**, 29, 695.

- [5] C. Fasting, C. A. Schalley, M. Weber, O. Seitz, S. Hecht, B. Kokschi, J. Dornedde, C. Graf, E. W. Knapp, R. Haag, *Angew. Chem. Int. Ed. Engl.* **2012**, 51, 10472.  
[6] L. L. Kiessling, J. E. Gestwicki, L. E. Strong, *Curr. Opin. Chem. Biol.* **2000**, 4, 696.  
[7] M. Mammen, S. K. Choi, G. M. Whitesides, *Angew. Chem. Int. Ed. Engl.* **1998**, 37, 2754.  
[8] A. Mulder, J. Huskens, D. N. Reinhoudt, *Org. Biomol. Chem.* **2004**, 2, 3409.  
[9] M. Marsh, A. Helenius, *Cell* **2006**, 124, 729.  
[10] J. Vonnemann, S. Liese, C. Kuehne, K. Ludwig, J. Dornedde, C. Bottcher, R. R. Netz, R. Haag, *J. Am. Chem. Soc.* **2015**, 137, 2572.  
[11] J. Witten, T. Samad, K. Ribbeck, *Curr. Opin. Biotechnol.* **2018**, 52, 124.  
[12] J. V. Fahy, B. F. Dickey, *N. Engl. J. Med.* **2010**, 363, 2233.  
[13] R. Bansil, B. S. Turner, *Curr. Opin. Colloid Interface Sci.* **2006**, 11, 164.  
[14] J. D. Reuter, A. Myc, M. M. Hayes, Z. Gan, R. Roy, D. Qin, R. Yin, L. T. Piehler, R. Esfand, D. A. Tomalia, *Bioconjugate Chem.* **1999**, 10, 271.  
[15] M. Calderón, M. A. Quadir, S. K. Sharma, R. Haag, *Adv. Mater.* **2010**, 22, 190.  
[16] P. Anilkumar, T. B. Lawson, S. Abbina, J. T. Mäkelä, R. C. Sabatelle, L. E. Takeuchi, B. D. Snyder, M. W. Grinstaff, J. N. Kizhakkedathu, *Nat. Commun.* **2020**, 11, 2139.  
[17] M. I. ul-Hag, R. A. Sheno, D. E. Brooks, J. N. Kizhakkedathu, *J. Polym. Sci., Part A: Polym. Chem.* **2013**, 51, 2614.  
[18] R. A. Cone, *Adv. Drug Deliv. Rev.* **2009**, 61, 75.  
[19] N. K. Sauter, J. E. Hanson, G. D. Glick, J. H. Brown, R. L. Crowther, S. J. Park, J. J. Skehel, D. C. Wiley, *Biochemistry* **1992**, 31, 9609.  
[20] M. A. Tortorici, A. C. Walls, Y. Lang, C. Wang, Z. Li, D. Koerhuis, G. J. Boons, B. J. Bosch, F. A. Rey, R. J. de Groot, D. Velesler, *Nat. Struct. Mol. Biol.* **2019**, 26, 481.  
[21] G. H. Guibinga, A. Miyanochara, J. D. Esko, T. Friedmann, *Mol. Ther.* **2002**, 5, 538.  
[22] N. Peerboom, E. Schmidt, E. Trybala, S. Block, T. Bergstrom, H. P. Pace, M. Bally, *ACS Infect. Dis.* **2018**, 4, 944.  
[23] R. E. Loomis, A. Prakobphol, M. J. Levine, M. S. Reddy, P. C. Jones, *Arch. Biochem. Biophys.* **1987**, 258, 452.  
[24] J. Bolscher, E. Veerman, A. Van Nieuw Amerongen, A. Tulp, D. Verwoerd, *Biochem. J.* **1995**, 309, 801.  
[25] S. Bhatia, M. Hilsch, J. L. Cuellar Camacho, K. Ludwig, C. Nie, B. Parshad, M. Wallert, S. Block, D. Lauster, C. Böttcher, *Angew. Chem., Int. Ed.* **2020**, 59, 12417.  
[26] S. Bhatia, D. Lauster, M. Bardua, K. Ludwig, S. Angioletti-Uberti, N. Popp, U. Hoffmann, F. Paulus, M. Budt, M. Stadtmüller, *Biomaterials* **2017**, 138, 22.  
[27] D. Lauster, S. Klenk, K. Ludwig, S. Nojumi, S. Behren, L. Adam, M. Stadtmüller, S. Saenger, S. Zimmmer, K. Hönzke, L. Yao, U. Hoffmann, M. Bardua, A. Hamann, M. Witzernath, L. E. Sander, T. Wolff, A. C. Hocke, S. Hippenstiel, S. De Carlo, J. Neudecker, K. Osterrieder, N. Budisa, R. R. Netz, C. Böttcher, S. Liese, A. Herrmann, C. P. R. Hackenberger, *Nat. Nanotechnol.* **2020**, 15, 373.  
[28] E. de Vries, W. Du, H. Guo, C. A. M. de Haan, *Trends Microbiol.* **2020**, 28, 57.  
[29] P. E. Hamming, N. J. Overeem, J. Huskens, *Chem. Sci.* **2019**, 11, 27.  
[30] R. Wagner, M. Matrosovich, H. D. Klenk, *Rev. Med. Virol.* **2002**, 12, 159.  
[31] H. Guo, H. Rabouw, A. Slomp, M. Dai, F. van der Vegt, J. W. M. van Lent, R. McBride, J. C. Paulson, R. J. de Groot, F. J. M. van Kuppeveld, E. de Vries, C. A. M. de Haan, *PLoS Pathog.* **2018**, 14, e1007233.  
[32] A. Harris, G. Cardone, D. C. Winkler, J. B. Heymann, M. Brecher, J. M. White, A. C. Steven, *Proc. Natl. Acad. Sci. U. S. A.* **2006**, 103, 19123.  
[33] J. L. McAuley, B. P. Gilbertson, S. Trifkovic, L. E. Brown, J. L. McKimm-Breschkin, *Front. Microbiol.* **2019**, 10, 39.  
[34] J. C. Pedersen, *Avian Influenza Virus*, Springer, Berlin, **2008**, pp. 53–66.

- [35] M. Müller, D. Lauster, H. H. K. Wildenauer, A. Herrmann, S. Block, *Nano Lett.* **2019**, *19*, 1875.
- [36] D. Axelrod, *Methods Cell Biol.* **1989**, *30*, 245.
- [37] T. Ito, Y. Kawaoka, *Vet. Microbiol.* **2000**, *74*, 71.
- [38] N. K. Sauter, M. D. Bednarski, B. A. Wurzburg, J. E. Hanson, G. M. Whitesides, J. J. Skehel, D. C. Wiley, *Biochemistry* **1989**, *28*, 8388.
- [39] M. Mammen, G. Dahmann, G. M. Whitesides, *J. Med. Chem.* **1995**, *38*, 4179.
- [40] J. Martín, S. A. Wharton, Y. P. Lin, D. K. Takemoto, J. J. Skehel, D. C. Wiley, D. A. Steinhauer, *Virology* **1998**, *241*, 101.
- [41] D. W. Lee, H. L. Hsu, K. B. Bacon, S. Daniel, *PLoS One* **2016**, *11*, e0163437.
- [42] M. Bally, A. Gunnarsson, L. Svensson, G. Larson, V. P. Zhdanov, F. Hook, *Phys. Rev. Lett.* **2011**, *107*, 188103.
- [43] R. McDaniel, K. Sharp, D. Brooks, A. McLaughlin, A. Winiski, D. Cafiso, S. McLaughlin, *Biophys. J.* **1986**, *49*, 741.
- [44] X. Zhu, R. McBride, C. M. Nycholat, W. Yu, J. C. Paulson, I. A. Wilson, *J. Virol.* **2012**, *86*, 13371.
- [45] R. E. Amaro, P. U. leong, G. Huber, A. Dommer, A. C. Steven, R. M. Bush, J. D. Durrant, L. W. Votapka, *ACS Cent. Sci.* **2018**, *4*, 1570.
- [46] J. Yang, S. Liu, L. Du, S. Jiang, *Rev. Med. Virol.* **2016**, *26*, 242.
- [47] S. Block, *Biomolecules* **2018**, *8*, 30.
- [48] S. Hatakeyama, Y. Sakai-Tagawa, M. Kiso, H. Goto, C. Kawakami, K. Mitamura, N. Sugaya, Y. Suzuki, Y. Kawaoka, *J. Clin. Microbiol.* **2005**, *43*, 4139.
- [49] C. Nie, B. Parshad, S. Bhatia, C. Cheng, M. Stadtmüller, A. Oehrl, Y. Kerkhoff, T. Wolff, R. Haag, *Angew. Chem. Int. Ed.* **2020**, *59*, 15532.
- [50] R. K. Kainthan, E. B. Muliawan, S. G. Hatzikiriakos, D. E. Brooks, *Macromolecules* **2006**, *39*, 7708.
- [51] D. Wilms, F. Wurm, J. Nieberle, P. Bohm, U. Kemmer-Jonas, H. Frey, *Macromolecules* **2009**, *42*, 3230.





## Supporting Information

for *Small*, DOI: 10.1002/smll.202004635

Mucin-Inspired, High Molecular Weight Virus Binding Inhibitors Show Biphasic Binding Behavior to Influenza A Viruses

*Matthias Wallert, Chuanxiong Nie, Parambath Anilkumar, Srinivas Abbina, Sumati Bhatia, Kai Ludwig, Jayachandran N. Kizhakkedathu, Rainer Haag,\* and Stephan Block\**

## Supporting Information

**Mucin-Inspired, High Molecular Weight Virus Binding Inhibitors Show Biphasic Binding Behavior to Influenza A Viruses**

*Matthias Wallert, Chuanxiong Nie, Parambath Anilkumar, Srinivas Abbina, Sumati Bhatia, Kai Ludwig, Jayachandran N. Kizhakkedathu, Rainer Haag\*, Stephan Block\**

\*Corresponding authors:

Stephan Block, e-mail: [stephan.block@fu-berlin.de](mailto:stephan.block@fu-berlin.de)

Rainer Haag, email: [haag@zedat.fu-berlin.de](mailto:haag@zedat.fu-berlin.de)

**Table of contents**

1. Synthesis	2
1.1 Materials	2
1.2 Synthesis of hyperbranched polyglycerols (hPG)	3
1.3 Functionalization of hyperbranched polyglycerols	3
1.3.1 Mesylation and azidation	4
1.3.2 Sulfation	4
1.3.3 Click protected propagylated sialic acid by CuAAC and deprotection	5
2. Characterization	6
2.1 Materials	6
2.2 Cryo-electron microscopy	7
2.3 Total internal reflection fluorescence microscopy	8
2.4 Cell binding of IAV X31 to MDCK-II cells	9
2.5 Nanoparticle tracking analysis	10

3. Figures and tables	11
S1: TEM measurement of hPG <sub>2600</sub> -SA-SO <sub>4</sub>	11
S2: Hemagglutination inhibition assay of all inhibitors	12
S3: NTA of concentration dependent binding of X31 and hPG <sub>2600</sub> -SA-SO <sub>4</sub>	13
S4: GPC measurement of hPG <sub>2600</sub>	14
S5: <sup>1</sup> H NMR of hPG <sub>2600</sub> -N <sub>3</sub>	14
S6: <sup>1</sup> H NMR of hPG <sub>2600</sub> -N <sub>3</sub> -SO <sub>4</sub>	15
S7: IR spectra to verify conversion of azide moieties by click reaction	15
S8: Overview IR spectra binding inhibitors (10 kDa, 100 kDa, 500 kDa)	16
S9: <sup>1</sup> H NMR of hPG <sub>2600</sub> -SA-SO <sub>4</sub>	17
S10: <sup>1</sup> H NMR of hPG <sub>500</sub> -SA-SO <sub>4</sub>	17
S11: <sup>1</sup> H NMR of hPG <sub>100</sub> -SA-SO <sub>4</sub>	18
S12: <sup>1</sup> H NMR of hPG <sub>10</sub> -SA-SO <sub>4</sub>	18
S13: <sup>1</sup> H NMR of hPG <sub>2600</sub> -SO <sub>4</sub>	19
S14: <sup>1</sup> H NMR of hPG <sub>2600</sub> -SA	19
Table S1: Overview of hPGs used as scaffold for virus binding inhibitor	20
Table S2: Overview functionalization of hPG based binding inhibitor	20
Table S3: Overview data elemental analysis	21
4. References	22

## 1. Synthesis

### 1.1 Material

Glycidol was obtained from Sigma Aldrich (Steinheim, Germany) and was vacuum distilled over CaH<sub>2</sub> at 45 °C and stored over 4 Å molecular sieves at 4 °C. Trimethylolpropane, potassium methoxide (25 % in methanol), anhydrous 1,4-dioxane (99,8 %), potassium hydride (30 wt.% in oil), methanesulfonyl chloride, triethyl amine (≥99.5 %), sulfur trioxide pyridine complex (98 %), sodium L-ascorbate (≥ 98 %), sodium hydroxide (≥ 98 %), DMF (max. 0.005 % water), sodium azide (≥99.5 %), dialysis tube (benzoylated, 2 kDa MWCO) were obtained from Sigma Aldrich. Regenerated cellulose dialysis tubes (50 kDa, 10 kDa MWCO) were obtained from Spectrum Laboratories (Waltham, US). Sodium chloride was obtained

from Fisher Scientific (Schwerte, Germany). Sodium hydroxide ( $\geq 98\%$ ), copper(II) sulfate pentahydrate (p.a.) were obtained from Merck (Darmstadt, Germany). All reagents were used as received without any purifications, unless otherwise mentioned. Acetylated propagyl sialic acid (sialic acid derivative prop-2-ynyl  $\alpha$ -thiosialoside) was prepared by procedure as reported in literature.<sup>[1,2]</sup>

## 1.2 Synthesis of hyperbranched polyglycerols (hPG)

The recent published two step synthesis of hPG enables to reach molecular weights in the MDa region.<sup>[3]</sup> The molecular weight and dispersity were determined by GPC (see Figure S4) with a Waters 2695 separation module, a DAWN HELEOS II multi angle laser light scattering (MALS) detector coupled with Optilab T-rEX refractive index detector (Wyatt Technology, Santa Barbara, US). Using Waters ultrahydrogel columns (guard, linear and 120) the GPC measurements were performed in aqueous  $\text{NaNO}_3$  (0.1 M, pH 7). The used  $\text{dn/dc}$  value for polyglycerol was  $0.12 \text{ mL g}^{-1}$ . Further, all polymers were characterized by  $^1\text{H}$  NMR and invers gated  $^{13}\text{C}$  NMR using the solvent deuterated water as reference. The used NMR spectrometer are AVANCE700 (700 MHz, Bruker, Karlsruhe, Germany) and ECP500 (500 MHz, Jeol, Freising Germany).

The scaffold  $\text{hPG}_{2600}$  was stored the whole time in aqueous solution because after drying processes (*e.g.*, lyophilization) problems to redissolve the polymer can occur. The dry high-molecular weight  $\text{hPG}_{2600}$  is white and has a marshmallow like texture.

## 1.3 Functionalization of hyperbranched polyglycerols

The general synthesis sequence was the same for all hPG sizes (Figure 1b, main manuscript). Five percent of the hydroxy groups of the hPG were mesylated and subsequently converted to azide groups. Afterwards, five percent of the initial hydroxy groups were sulfated with sulfur trioxide pyridine complex. Subsequently acetyl protected propagylated sialic acid was linked via copper(I)-catalyzed alkyne-azide cycloaddition (CuAAC) to the

polymer. The deprotection of the sialic acid was done by the addition of sodium hydroxide (2M).

### 1.3.1 Mesylation and azidation

1300 mg of hPG<sub>2600</sub> (0.88 mmol OH to be functionalized, 1 eq.) was weighted from aqueous solution in a 25 mL round bottom flask. Under reduced pressure, 50 °C water was evaporated until almost no water was left. Dry DMF (4 mL) was added and the polymer dissolved again. Under reduced pressure, 50 °C DMF was evaporated until approximately 0.5 mL DMF was left. The addition and evaporation of dry DMF was repeated three times to remove water residues. Afterwards, the polymer was dissolved in 18 mL dry DMF. The reaction flask was equipped with a magnetic stir bar, a rubber septum and flushed with argon to exchange the gas face. Triethyl amine (306 µL, 2.2 mmol, 2.5 eq.) was added via Hamilton syringe in the reaction mixture. For 15 min argon was bubbled through the reaction mixture. Afterwards, methanesulfonyl chloride (136 µL, 1.8 mmol, 2.0 eq.) was added via Hamilton syringe slowly direct in the stirred reaction mixture. The flask was equipped with a balloon filled with argon and stirred at room temperature for 20 h. Afterwards, sodium azide (456 mg, 7.02 mmol, 8 eq.) were added and the flask was placed in an oil bath at 80 °C for 20 h. The reaction mixture was transferred in a dialysis tube (2 kDa MWCO, benzoylated) and dialyzed against water. A sample was taken and lyophilized to calculate the overall polymer amount in the solution. The obtained amount was 902.8 mg (yield 68.4 %) with a degree of azidation of 5.7 mol% (determined by elemental analysis). Further, a <sup>1</sup>H NMR (D<sub>2</sub>O, 500 MHz) was performed (see Figure S5).

### 1.3.2 Sulfation

The azidated polymer hPG<sub>2600</sub>-N<sub>3</sub> (400 mg, 0.27 mmol OH to be functionalized, 1.0 eq.) was weighted from aqueous polymer solution in a 25 mL round bottom flask. Under reduced pressure at 50 °C the water was evaporated until almost no water was left. Dry DMF (3 mL) was added to dissolve the polymer. Under reduced pressure, 50 °C DMF was evaporated until

approximately 0.5 mL DMF was left. To remove all water residues the addition, evaporation step of dry DMF was repeated thrice. Afterwards the polymer was dissolved in 8 mL dry DMF. The flask was equipped with a magnetic stir bar, a rubber septum and argon was bubbled through the polymer solution for 15 min. Sulfur trioxide pyridine complex (55.9 mg, 0.4 mmol, 1.3 eq.) was added in the stirred reaction mixture. The wall of the round bottom flask was washed with 4 mL dry DMF. After additional 10 min of bubbling argon through the solution the flask was equipped with a balloon filled with argon and placed in an oil bath at 60 °C for 20 h. The reaction was quenched with 7 mL sodium hydroxide solution (0.3 mol L<sup>-1</sup>), pH value 10. The reaction mixture was transferred in a dialysis tube (2 kDa MWCO, benzoylated) and dialyzed for 24 h against 0.3 mol L<sup>-1</sup> NaOH (two changes), 24 h against 10 wt.% NaCl solution and 72 h (9 changes) against water. 421.8 mg hPG<sub>2600</sub>-N<sub>3</sub>-SO<sub>4</sub> was obtained, which results in a yield of 97.7 %. By elemental analysis 5.0 mol% degree of sulfation was determined and the degree of azidation was verified. Further an <sup>1</sup>H NMR (500 MHz) spectrum was performed in D<sub>2</sub>O (see Figure S6).

### 1.3.3 Click protected propagylated sialic acid by CuAAC and deprotection

The polymer hPG<sub>2600</sub>-N<sub>3</sub>-SO<sub>4</sub> (150 mg, 0.11 mmol OH to be functionalized, 1.0 eq.) was weighted from aqueous solution in a 25 mL round bottom flask. Under reduced pressure, 50 °C the water was evaporated until almost no water was left. The polymer was dissolved again by the addition of 3 mL DMF (dry). Under reduced pressure, 50 °C DMF was evaporated until approximately 0.5 mL DMF was left. The addition and evaporation of DMF was repeated once again. Then 12 mL DMF was added and the polymer dissolved. The flask was equipped with a magnetic stir bar and rubber septum. Acetyl protected propagylated sialic acid (72.9 mg, 0.13 mmol, 1.2 eq.) were added and the wall of the flask was washed with 6 mL DMF. Argon was bubbled through the solution for 15 min. In a glass vial CuSO<sub>4</sub> 5H<sub>2</sub>O (11.1 mg, 0.04 mmol, 0.4 eq.) were dissolved in 150 µL H<sub>2</sub>O (blue, clear solution). In another glass vial sodium-L-ascorbate (88.3 mg, 0.45 mmol, 0.4 eq.) were dissolved in

150  $\mu\text{L}$   $\text{H}_2\text{O}$  (colorless, clear solution). The sodium ascorbate solution was transferred into the copper sulfate solution and mixed by shaking. A color change occurred from dark brown to bright brown to an orange turbid mixture. The orange mixture was transferred dropwise into the stirred polymer solution. For 10 min ultrasound was applied while argon bubbled through the solution. After that, the flask was equipped with a balloon filled with argon and placed in an oil bath at 50  $^\circ\text{C}$  for 20 h. The absence of the azide band in the infrared spectra at  $2100\text{ cm}^{-1}$  indicated the complete conversion of the click reaction with respect to the detection limit and the standard error of the measurement (see Figure S7). To deprotect the acetylated sialic acid 4 mL  $\text{H}_2\text{O}$  were added to increase the solubility and afterwards the pH value was increased to pH 10 with approximately 6 mL  $\text{NaOH}$  ( $2\text{ mol L}^{-1}$ ) solution. At this pH value the mixture was stirred for 2 h. EDTA disodium salt (14.0 mg, 0.04mmol, 0.4 eq.) was added to improve the removal of copper ions. Dialysis was done in a dialysis tube (2 kDa MWCO, benzoylated) against  $\text{H}_2\text{O}$ . The conversion of the azide groups was shown by infra-red spectroscopy. Therefore, the functional degree of sialic acid was assumed to be almost equal to the initial degree of azidation (5.6 mol%). Furthermore, a  $^1\text{H}$  NMR (700 MHz) was performed in  $\text{D}_2\text{O}$  (see Figure S9).

## 2. Characterization

### 2.1 Material

POPC (1-palmitoyl-2-oleoyl-glycero-3-phosphocholine), the ganglioside GD1a (disialoganglioside-GD1a (porcine brain, diammonium salt)), DSPE-PEG2k carboxylic acid (1,2-distearoyl-sn-glycero-3-phosphoethanolamine-N-[carboxy(polyethylene glycol)-2000] (sodium salt)), were purchased from Avanti Polar Lipids Inc. (Alabaster, AL). Tris-HCl (tris(hydroxymethyl)aminomethane hydrochloride), Dulbecco's phosphate buffered saline (DPBS), chloroform ( $\geq 99.9\%$ ), R18 (octadecyl rhodamine B chloride), calcium chloride ( $\geq 97\%$ ), Liquinox (critical-cleaning liquid detergent) were obtained from Sigma Aldrich

(Steinheim, Germany). Potassium dihydrogen phosphate (for analysis), Disodium hydrogen phosphate were obtained from Merck (Darmstadt, Germany). Potassium chloride (>99.5 %) was obtained from Grüssing (Filsum, Germany). 10x PBS buffer concentrate was used to prepare PBS buffer, according to the manufacturer's instructions. Propagation and labeling of influenza A/X-31 (H3N2) virus (IAV) was done in the same way as in our previous study.<sup>[4]</sup>

## 2.2 Cryo-electron microscopy

A perforated carbon film-covered microscopical 200 mesh grid (R1/4 batch of Quantifoil, MicroTools GmbH, Jena, Germany) was cleaned with chloroform and hydrophilised by 60 s glow discharging at 8 W in a BAL-TEC MED 020 device (Leica Microsystems, Wetzlar, Germany) before 5  $\mu$ l of the hPG2600-SA-SO<sub>4</sub> solution (0.7 mM) in PBS was applied to the grid. The sample was vitrified by automatic blotting and plunge freezing with a FEI Vitrobot Mark IV (Thermo Fisher Scientific Inc., Waltham, Massachusetts, USA) using liquid ethane as cryogen. The vitrified specimen was transferred to the autoloader of a FEI TALOS ARCTICA electron microscope (Thermo Fisher Scientific Inc., Waltham, Massachusetts, USA). This microscope is equipped with a high-brightness field-emission gun (XFEG) operated at an acceleration voltage of 200 kV. Micrographs were acquired on a FEI Falcon 3 direct electron detector (Thermo Fisher Scientific Inc., Waltham, Massachusetts, USA) using the 70  $\mu$ m objective aperture at a nominal magnification of 28,000 x, corresponding to a calibrated pixel size of 3.69 Å/pixel.

To generate stereo images, the same image section was recorded at two different tilt angles (4° and -4°) using the Compustage of the microscope. The corresponding micrographs were aligned with the software StereoPhoto Maker (Masuji Suto, Japan) and the resulting stereograms were inspected using Stereo shutter glasses.



### 2.3 Total internal reflection fluorescence microscopy

**Vesicle preparation** - Vesicles were used to form supported lipid bilayers. The vesicle composition consisted out of POPC (96.2 wt.%), ganglioside GD1a (2.5 wt.%, 1 mol %) and DSPE-PEG2k carboxylic acid (3.8 wt.%, 1 mol%). DSPE-PEG2k carboxylic acid was incorporated to promote unilamellarity of the vesicles and an enhanced fluidity of the formed SLBs after small volume extrusion. All lipids were stored in chloroform separately. The vesicle solution of ( $1 \text{ mg mL}^{-1}$ ) was prepared by mixing the dissolved lipids in a 50 mL round bottom flask. Afterwards, the lipids were dried under nitrogen stream and subsequently dried under vacuum for 1 h. The dried lipid mixture was rehydrated with 0.5 mL Tris-HCl buffer (0.1 M Tris-HCl, 50 mM potassium chloride, 5 mM calcium chloride; adjusted pH 7.4 with HCl). The mixture was homogenized via vortex for 30 s and extruded for 31 time through a polycarbonate membrane (100 nm pore size; Avanti Polar Lipids Inc., Alabaster, AL). The aqueous solution was stored in a glass vial at  $4 \text{ }^{\circ}\text{C}$  and were used for one month.

**SLB formation** - Glass slides (coverslips, 25 mm; VWR, Darmstadt, Germany) were placed in a holder in a 250 mL beaker (high) and cleaned with 150 mL deionized water (Milli-Q; Merck, Darmstadt, Germany) and 0.5 mL Liquinox. The beaker was heated for 75 min at  $85 \text{ }^{\circ}\text{C}$ . Afterwards, every glass slide was taken out separately and cleaned intensively with deionized water. Clean glass slides were stored in a 50 mL falcon tube in 10 mL deionized water until further use, but discarded after one day.

Cleaned glass slides were dried at room temperature and self-made wells out of polydimethylsiloxane (PDMS) were mounted at the glass slides. Vesicle solution ( $0.33 \text{ mg mL}^{-1}$ ) was added into the wells and the SLB is formed by the rupture of the adsorbed vesicles at the glass surface. After 10 min the remaining vesicles in the solution were removed by washing with PBS buffer (10 times) using a micropipette, followed by injection influenza A virus (IAV) solution with or without containing inhibitor. The inhibitor concentration was changed, while the virus concentration was kept constant.

**TIRF microscopy** – A Nikon Eclipse Ti-E microscope (Nikon, Düsseldorf, Germany) was equipped with a T-SFL TIRF illuminator, a 100x Plan-Apo oil immersion objective (NA 1.45), a Lumen 200 (Prior Scientific, Cambridge, UK) white light source and an Andor Zyla 4.2 sCMOS camera (Oxford Instruments, Oxford, UK).

Virus interactions with the SLB were investigated by recording 5 TIRF microscopy videos (each 1000 frames, fps=0.11, exposure time 80 ms, 2 x 2 binning, 25 % light intensity, field of view 133  $\mu\text{m}$  x 133  $\mu\text{m}$ , pixel size 130 nm x 130 nm; mCherry filter cube). Single virus tracking was done using homemade MATLAB scripts described earlier,<sup>[4]</sup> yielding information about virus binding kinetics like attachment-, detachment-rates and the diffusion coefficient of SLB-bound viruses. Out of this data the on-rate and off-rate of the IAV-SLB interaction were extracted by equilibrium fluctuation analysis (EFA).<sup>[5, 6]</sup>

#### **2.4 Cell binding of IAV X31 to MDCK-II cells**

Madin-Darby Canine Kidney-II (MDCK) epithelial cells (ATCC, Manassas, US) were grown using Dulbecco's Modified Eagle Medium (PAN Biotech, Aidenbach, Germany; containing 10 % fetal bovine serum, 2 mM L-glutamine, 100  $\mu\text{g ml}^{-1}$  streptomycin and 100units  $\text{ml}^{-1}$  penicillin) at 37 °C and 5 % carbon dioxide. The cultured MDCK II cells are seeded in 8-well confocal slides and cultured for 1-2 days till confluency. 100  $\mu\text{L}$  X31 solution (protein content: 0.36  $\text{mg mL}^{-1}$ ,  $1.1 \times 10^{11}$  particles  $\text{mL}^{-1}$ ) was incubated with 2  $\mu\text{L}$  DiO (20  $\mu\text{M}$ , 3,3'-Dioctadecyloxycarbocyanine perchlorate in ethanol, D4929 in Merck) for 30 min in dark. The free dyes were removed by spin column then. The to be tested MuVib inhibitors were diluted in PBS to desired concentrations and 90  $\mu\text{L}$  inhibitor was incubated with 10  $\mu\text{L}$  labelled virus for 45 min at room temperature with constant gentle shaking. The cells are washed twice with PBS to remove culture medium and the MuVib inhibitor mixture was applied and incubated on ice for 2 hours. Afterwards, the non-binding viruses were removed by washing twice with PBS. The cell nucleus was labelled with Hoechst 23358 for

10 min and then the cells were washed once with PBS to remove free dyes. The cells were then fixed with 4 % paraformaldehyde for 10 min at r. t. and washed again with PBS. Finally, Z-wide images were taken with confocal laser scanning microscopy (Leica SP8, Wetzlar, Germany) by setting the glass slide as the bottom and the last layer above the cell surface to see the viruses on top. From bottom to top, 30 images with step size around 0.4  $\mu\text{m}$  were taken to visualize the virus on the cells. The images were stacked to see all the virus on the surface. The processing and the counting of the virus number were performed as described recently.<sup>[7]</sup>

### **2.5 Nanoparticle tracking analysis (NTA)**

The virus binding to the synthesized MuVib inhibitor hPG<sub>2600</sub>-SA-SO<sub>4</sub> is studied by nanoparticle tracking analysis (NTA; NanoSight NS500, Malvern). The fluid channel and chamber were washed thoroughly by MilliQ water prior to the experiment. Then, 1 mL X31 solution (1  $\mu\text{g}/\text{mL}$  in PBS) with different concentrations of inhibitor was loaded via a peristaltic pump and a 30-second video (749 frames, 25 fps) of particles was captured at 25 °C with more than  $10^4$  particles being recorded. The video was analyzed with the default script for particle sizes. The experiment was repeated for 3 times for each inhibitor concentration tested (see Figure S3).

## 3. Figures and tables

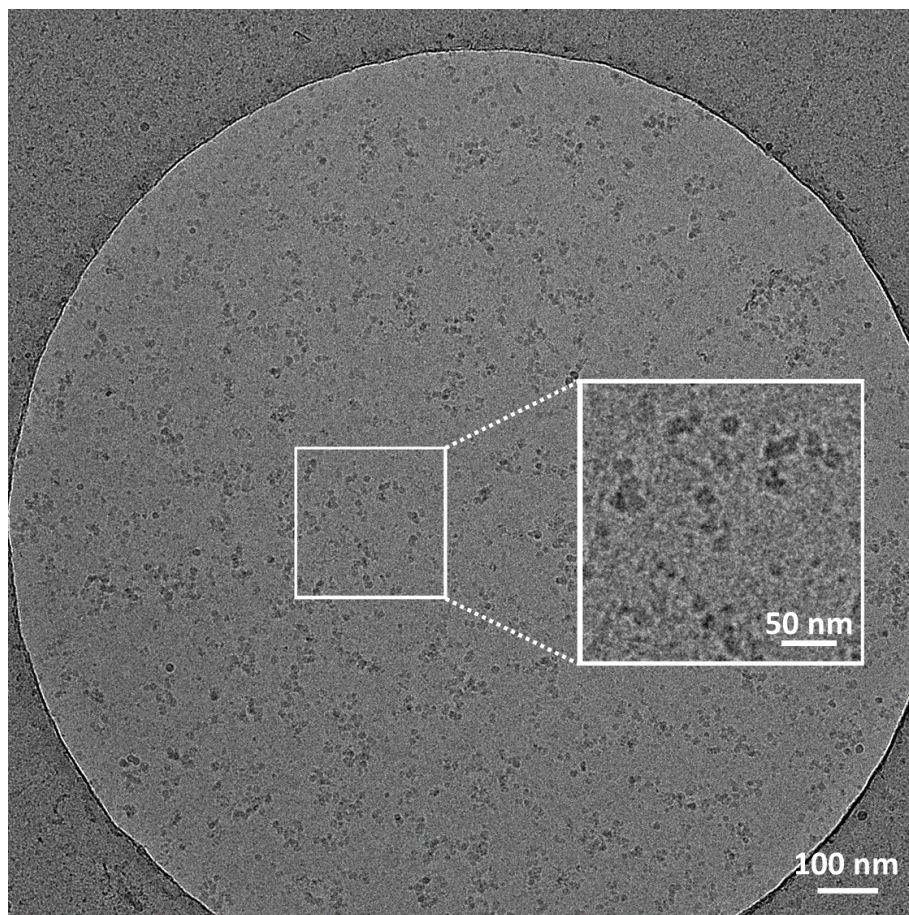


**Figure S1.** Cryo-electron microscopy of hPG<sub>2600</sub>-SA-SO<sub>4</sub> in PBS. The micrograph shows that the polymers are of spherical or partly slightly elongated shape. In order to verify that these projection images do not contain large aggregates, but mostly individual polymers, stereograms were created to obtain additional information in the z-direction. The stereograms were evaluated with the help of stereo shutter glasses and showed absence of large aggregates.

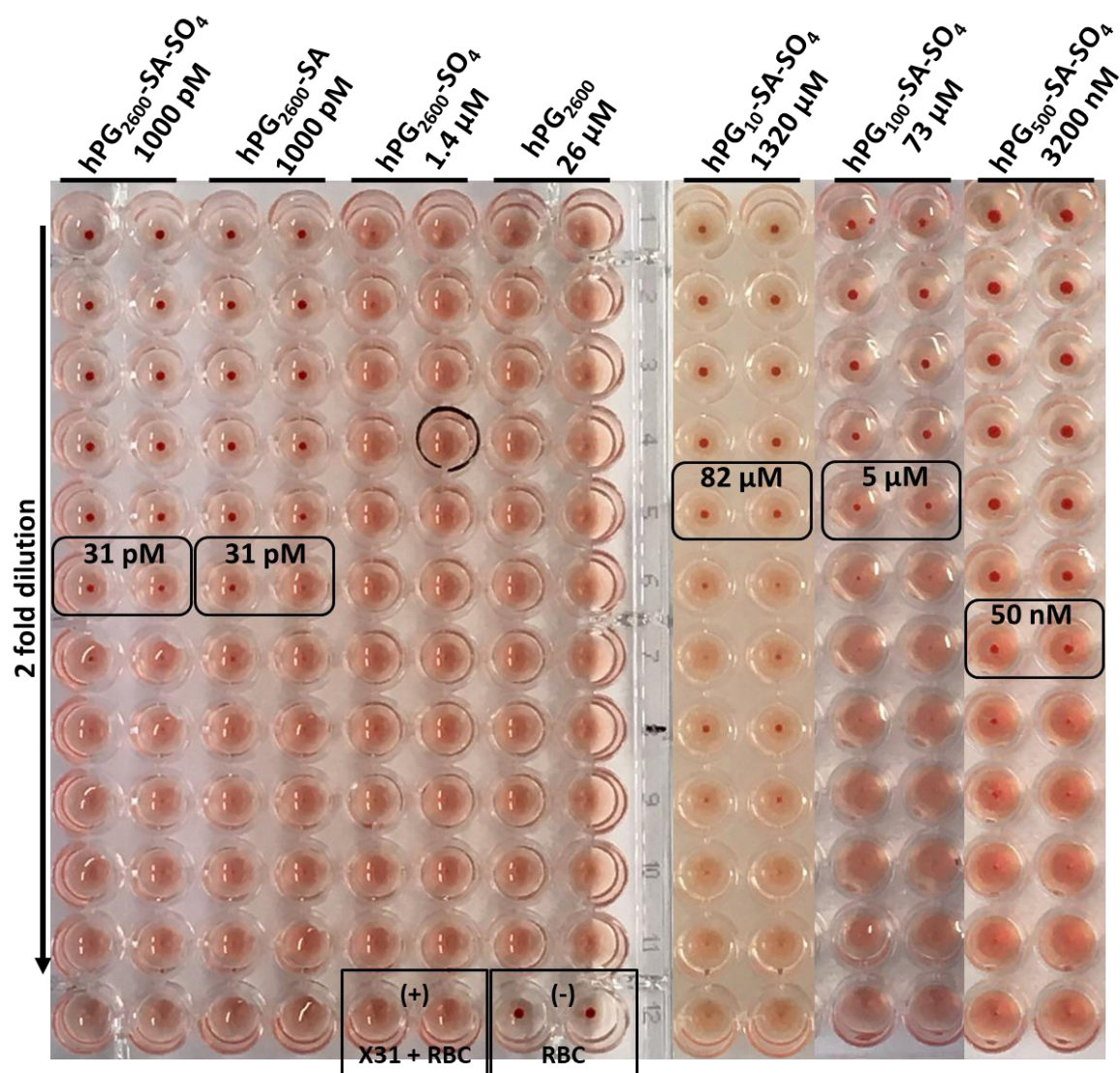


**Figure S2.** Performance of all synthesized mucin-inspired binding inhibitors in hemagglutination inhibition assay.



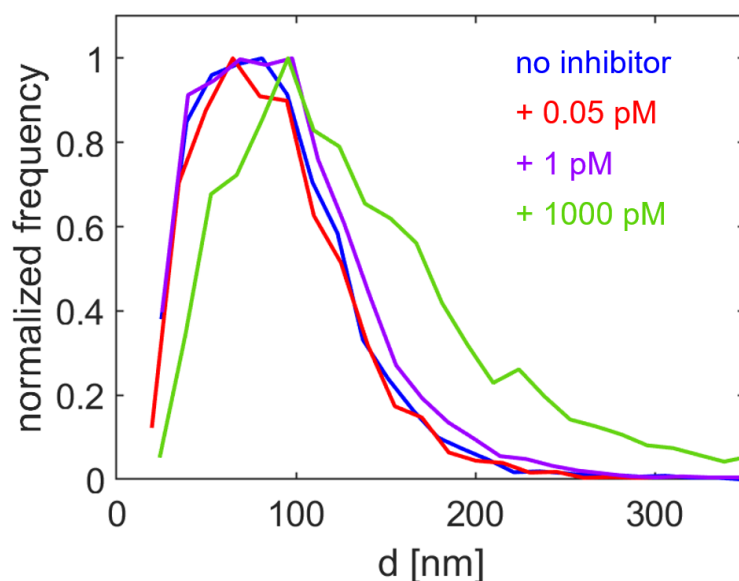


**Figure S3.** Size distributions of the IAV strain X31 (blue) and of mixtures of this IAV with either 0.05 pM (red trace), 1 pM (purple trace), or 1000 pM (green trace) of the MuVib inhibitor hPG2600-SA-SO<sub>4</sub>. These size distributions were determined using nanoparticle tracking analysis (NTA) and normalized by the peak frequency. The size distribution of the IAV strain X31 exhibits a mean value of  $99.2 \pm 2.7$  nm (average value  $\pm$  standard deviation from 3 measurements), which shifts to  $95.6 \pm 2.4$  nm,  $105.4 \pm 2.7$  nm, and  $173.6 \pm 6.3$  nm after addition of 0.05 pM (red trace), 1 pM (purple trace), and 1000 pM (green trace) of the MuVib inhibitor hPG<sub>2600</sub>-SA-SO<sub>4</sub>, respectively. Application of a student's t-test indicates that the changes to the size distribution between 0 pM and 0.05 pM are statistically not significant ( $p < 0.16$ ), while the increase in mean diameter caused by addition of 1 pM and 1000 pM is statistically significant ( $p < 0.05$  and  $p < 0.0001$ , respectively), thereby proving binding of the MuVib inhibitor to the IAVs. This interaction causes only a relatively small increase of the average size after adding 1 pM of the MuVib inhibitor, which indicates that the IAVs are only partially covered with inhibitors in this case. For 1000 pM, however, the size distribution shifts by  $\sim 70$  nm, which matches very well with twice the size of the MuVib inhibitor ( $\sim 60$  nm) and thus indicates full coverage on the IAVs. Both observations can be understood based on the notation that neuraminidase has been shown to form clusters in the IAV envelope, while hemagglutinin is rather homogenously distributed in the envelope.<sup>[8]</sup>

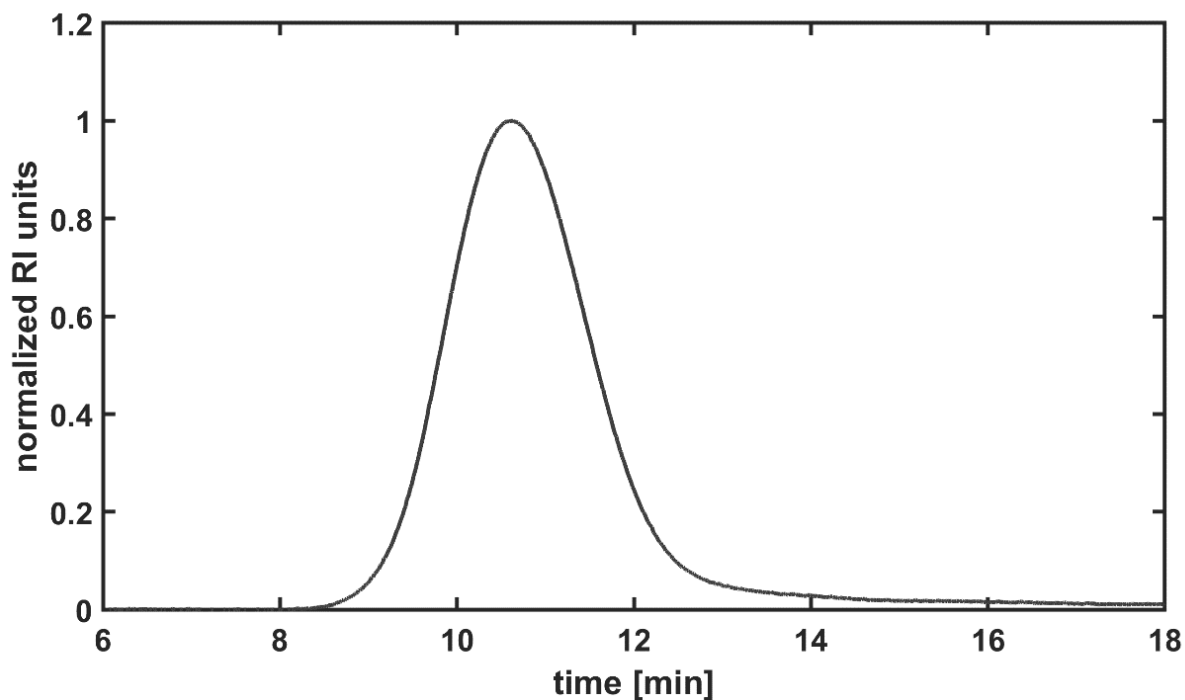


Figure S4. GPC measurement of  $hPG_{2600}$  shows a monomodal distribution

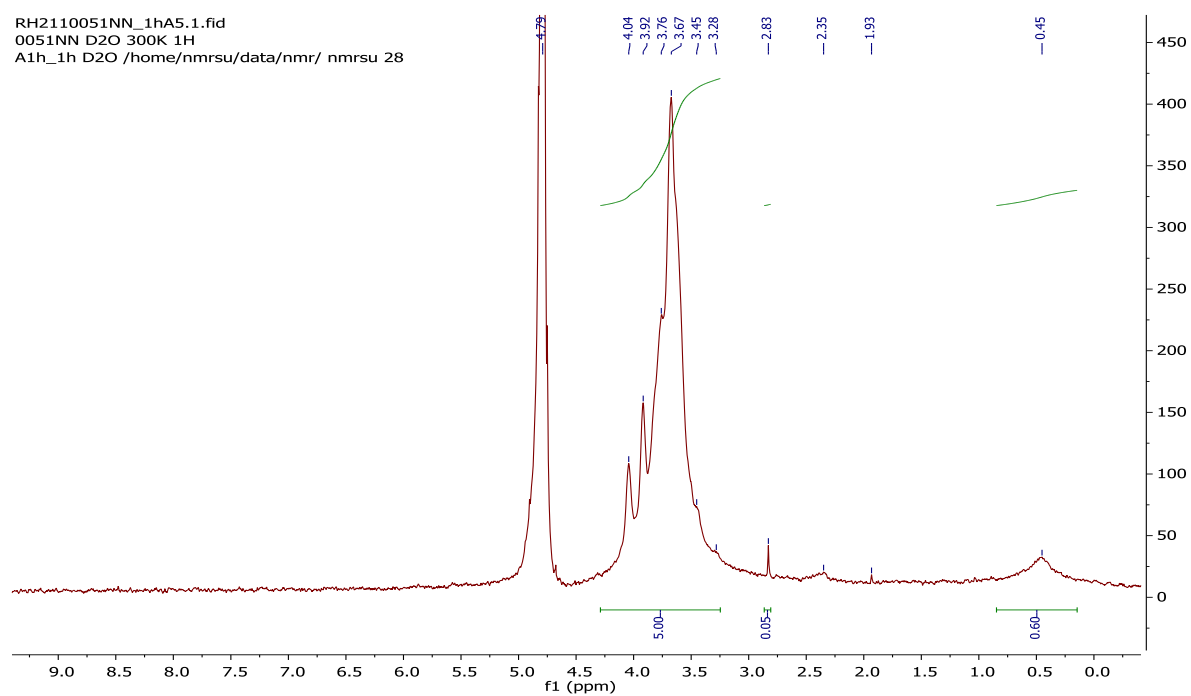
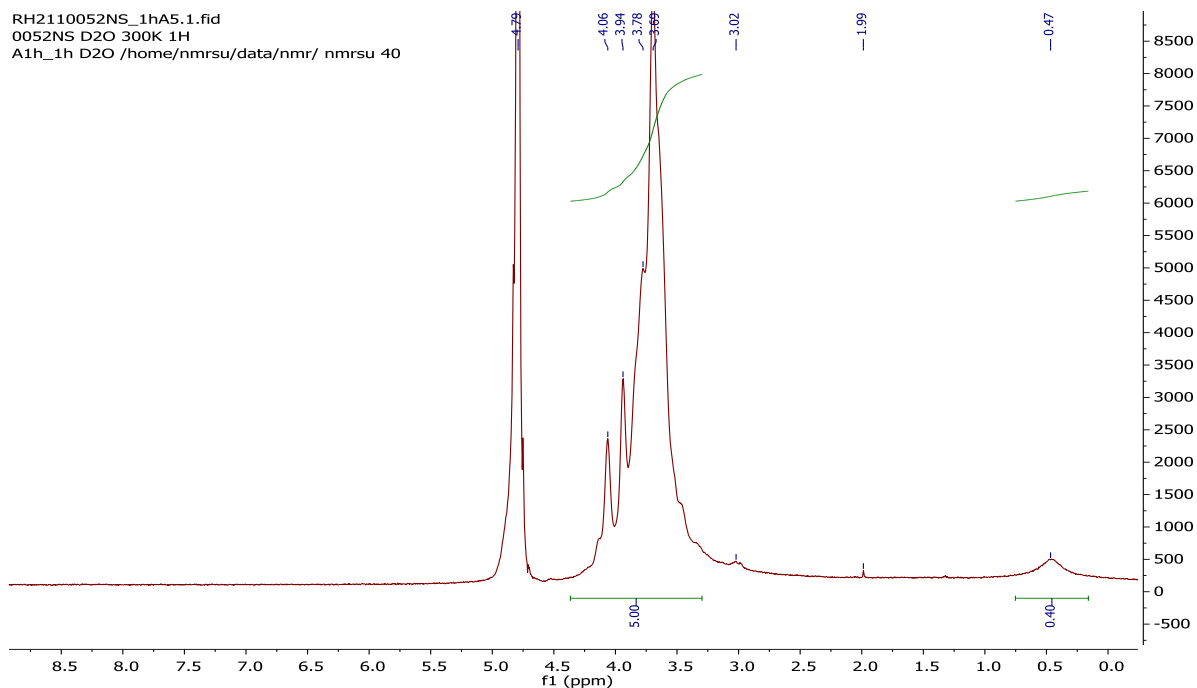
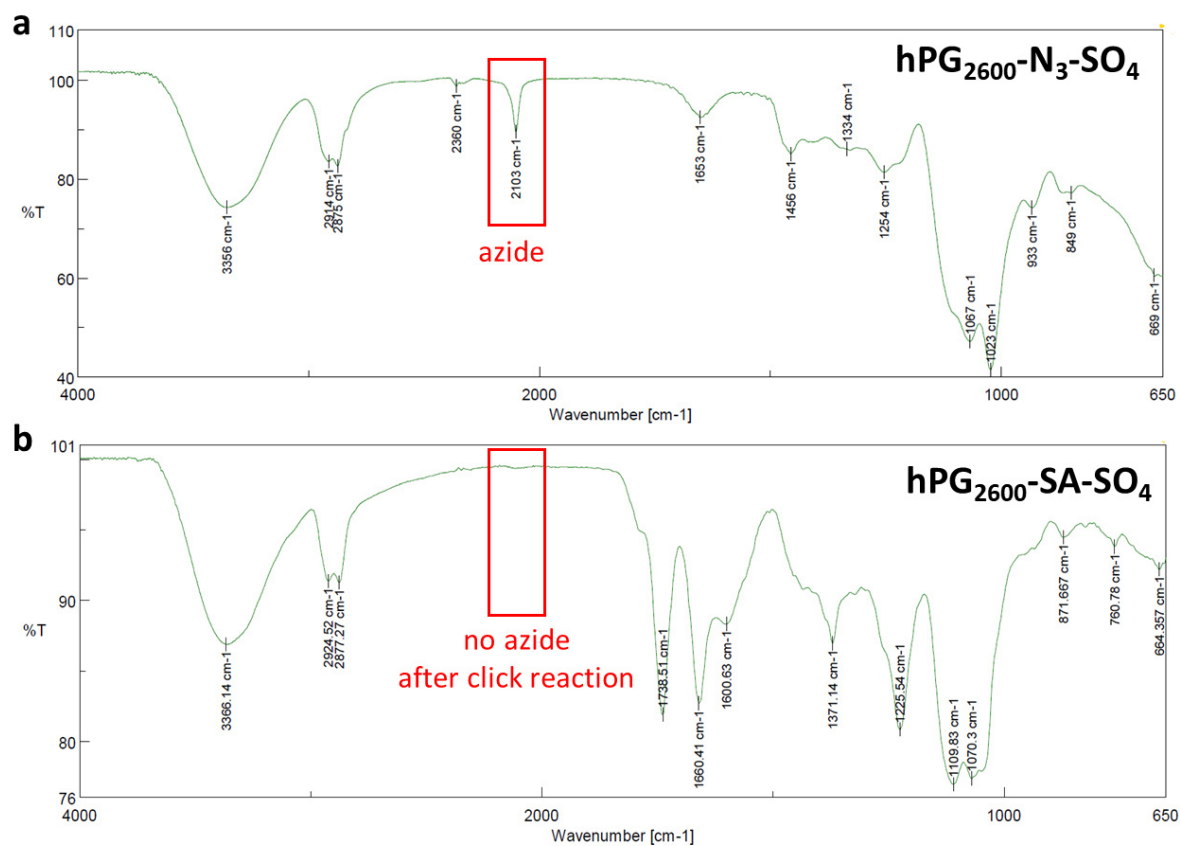


Figure S5.  $^1H$  NMR (500 MHz,  $D_2O$ ) of  $hPG_{2600-N_3}$



**Figure S6.**  $^1\text{H}$  NMR (500 MHz,  $\text{D}_2\text{O}$ ) of  $\text{hPG}_{2600}\text{-N}_3\text{-SO}_4$



**Figure S7.** IR spectra before (a,  $\text{hPG-N}_3\text{-SO}_4$ ) and after click reaction (b,  $\text{hPG-SA-SO}_4$ ). Used spectrometer was FT/IR-4100 from Jasco Deutschland, Pfungstadt.



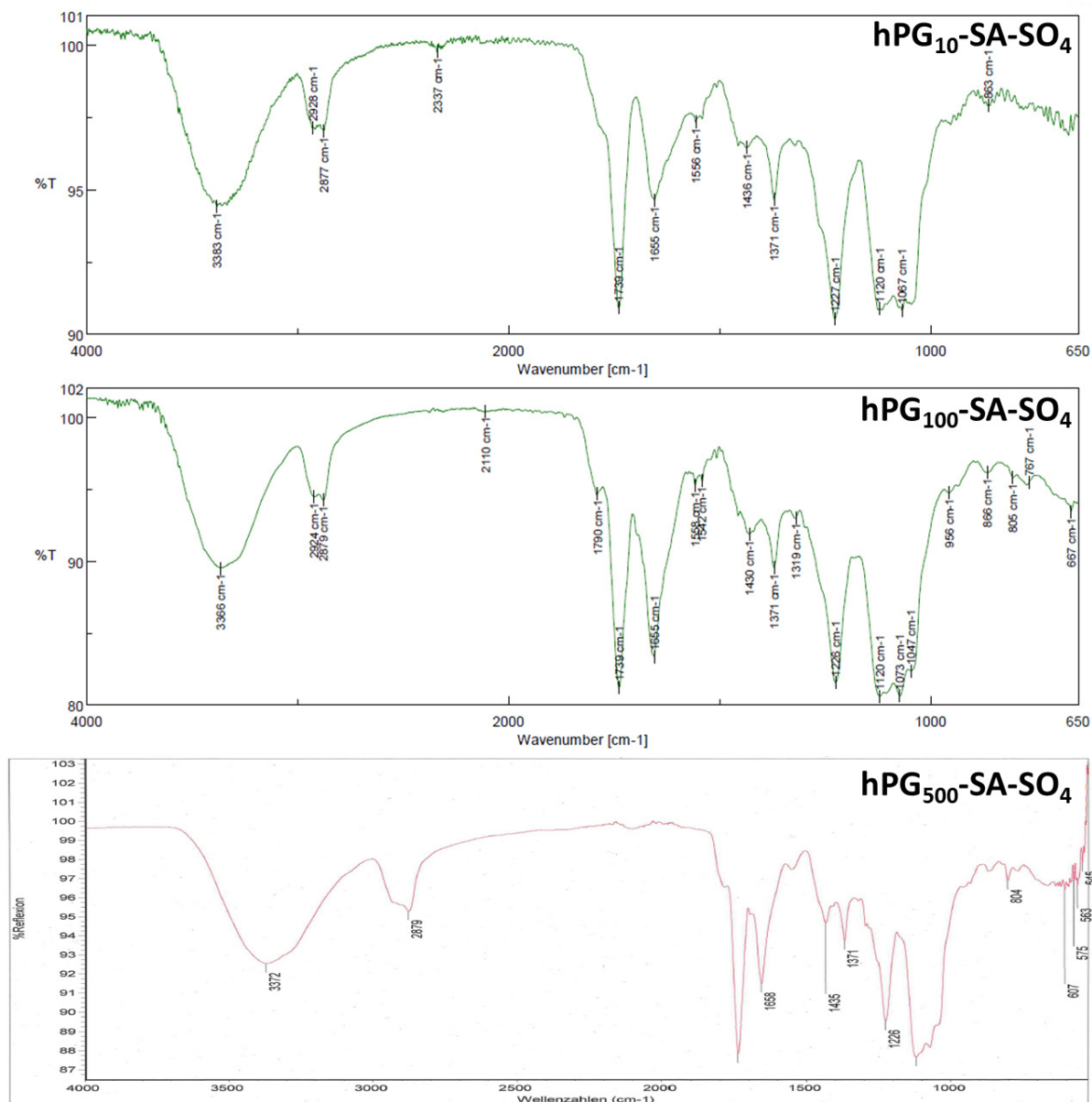


**Figure S8.** Overview IR spectra of virus binding inhibitors 10 kDa, 100 kDa and 500 kDa hPG functionalized with sialic acid (5 mol%) and sulfate (5 mol%). IR (neat, cm<sup>-1</sup>)  $\nu$ : 1047, 1073, 1120, 1126, 1371, 1665, 1739, 2878, 3372.

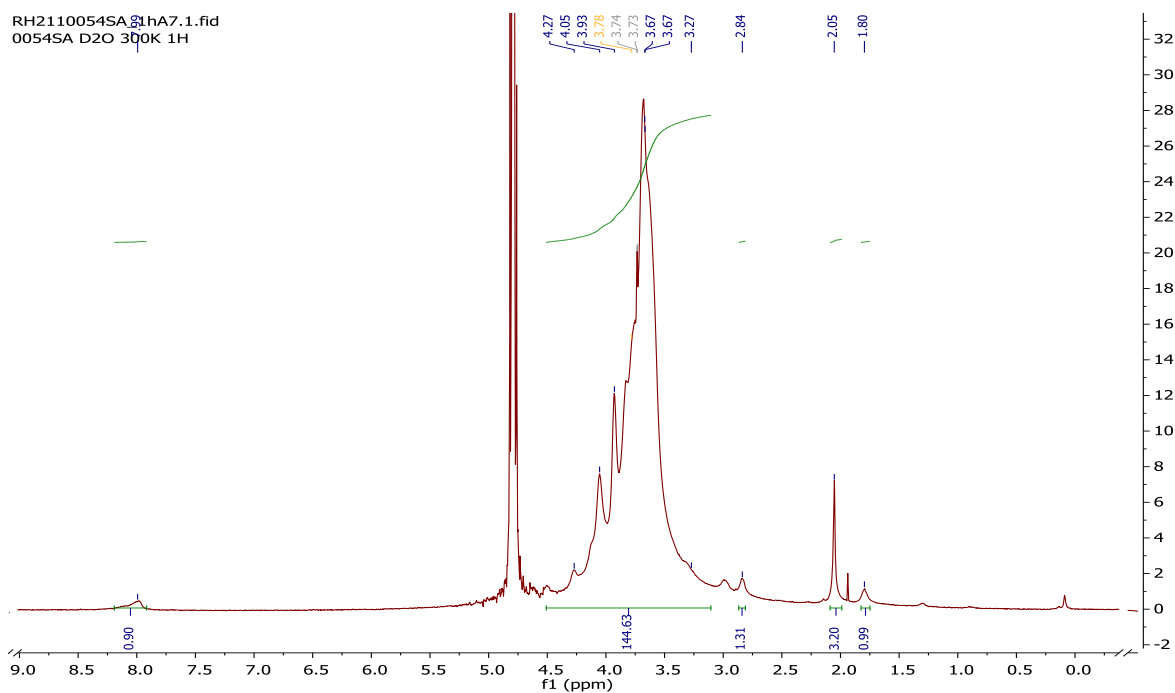


**Figure S9.**  $^1\text{H}$  NMR (700 MHz) of 2.6 MDa hPG-SA-SO<sub>4</sub> in D<sub>2</sub>O,  $\delta$ : 7.99 (bs, 1H, triazolyl proton), 4.52-3.27 [m, 9H (SA), dPG backbone], 2.84 (bs, 1H, SA H-3e), 2.05 (s, 3H, NHAc), 1.80 (bs, 1H, SA H-3a).

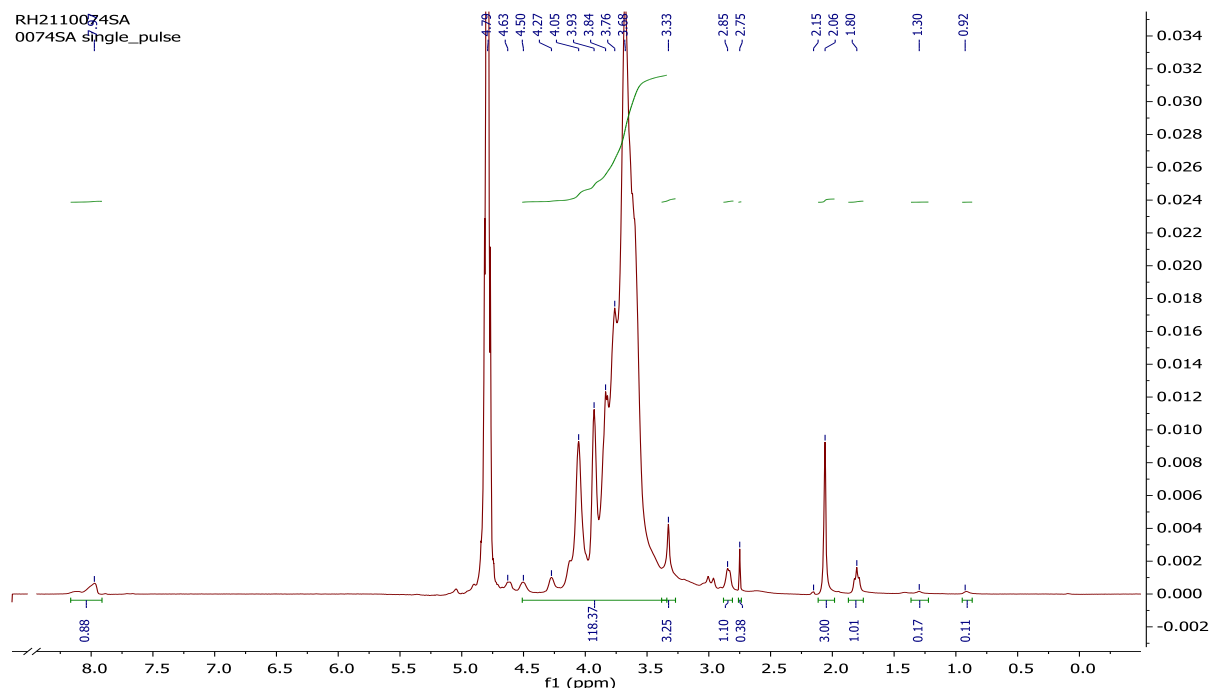


**Figure S10.**  $^1\text{H}$  NMR (700 MHz, D<sub>2</sub>O) of hPG<sub>500</sub>-SA-SO<sub>4</sub>,  $\delta$ : 7.99 (bs, 1H, triazolyl proton), 4.51-3.34 [m, 9H (SA), dPG backbone], 2.85 (bs, 1H, SA H-3e), 2.06 (s, 3H, NHAc), 1.80 (bs, 1H, SA H-3a).

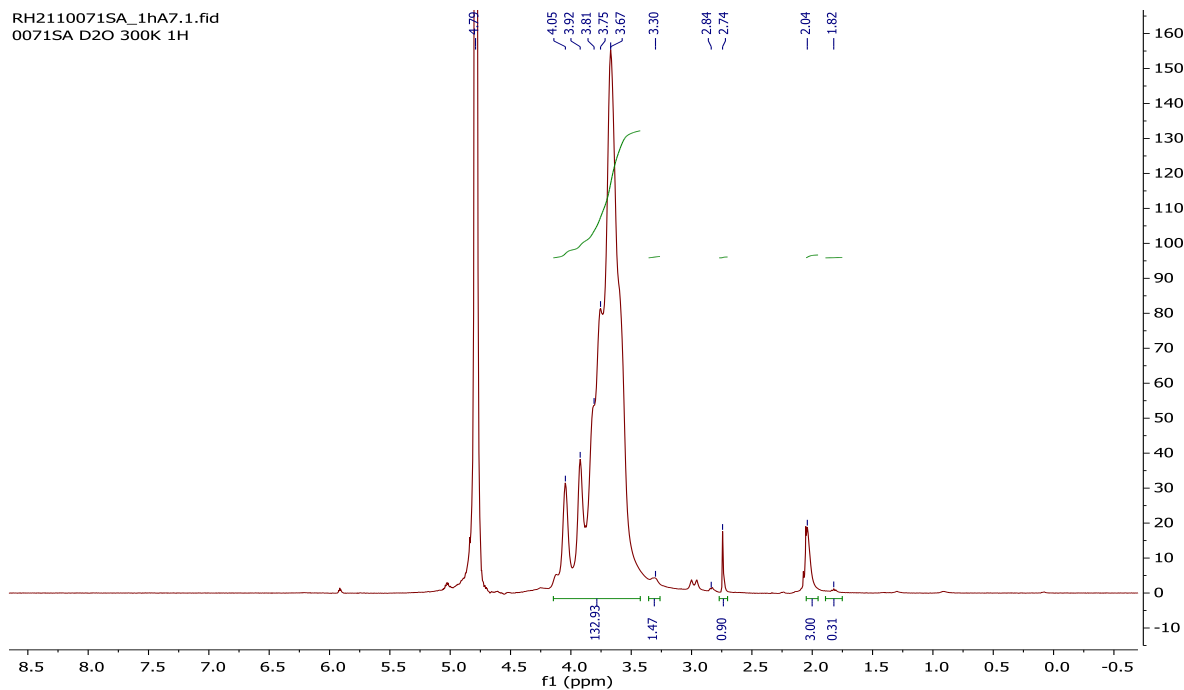


**Figure S11.**  $^1\text{H}$  NMR (700 MHz,  $\text{D}_2\text{O}$ ) hPG<sub>100</sub>-SA-SO<sub>4</sub>

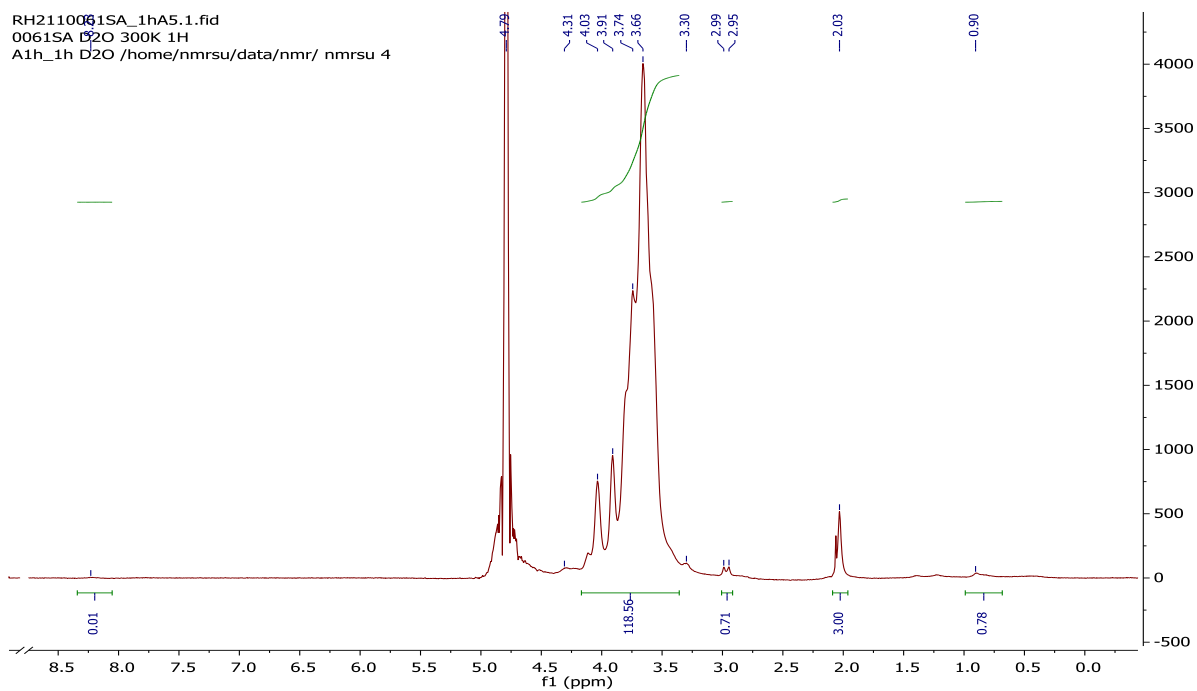


**Figure S12.**  $^1\text{H}$  NMR (500 MHz,  $\text{D}_2\text{O}$ ) of hPG<sub>10</sub>-SA-SO<sub>4</sub>

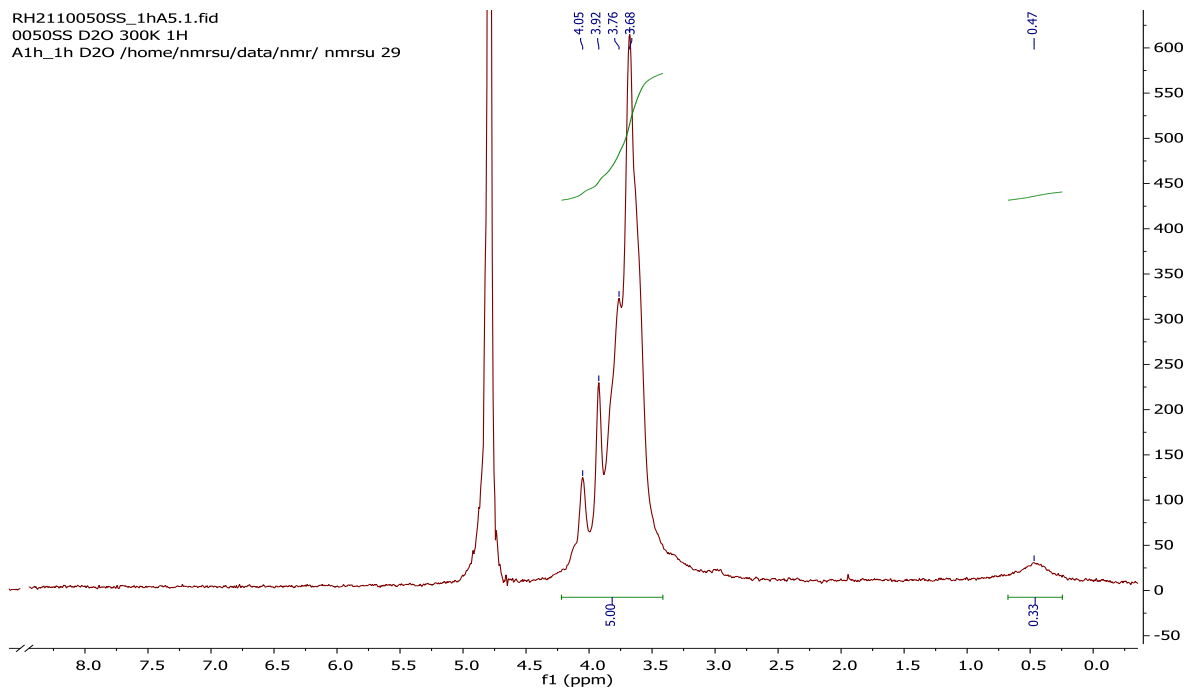


**Figure S13.**  $^1\text{H}$  NMR (500 MHz,  $\text{D}_2\text{O}$ ) of  $\text{hPG}_{2600}\text{-SO}_4$

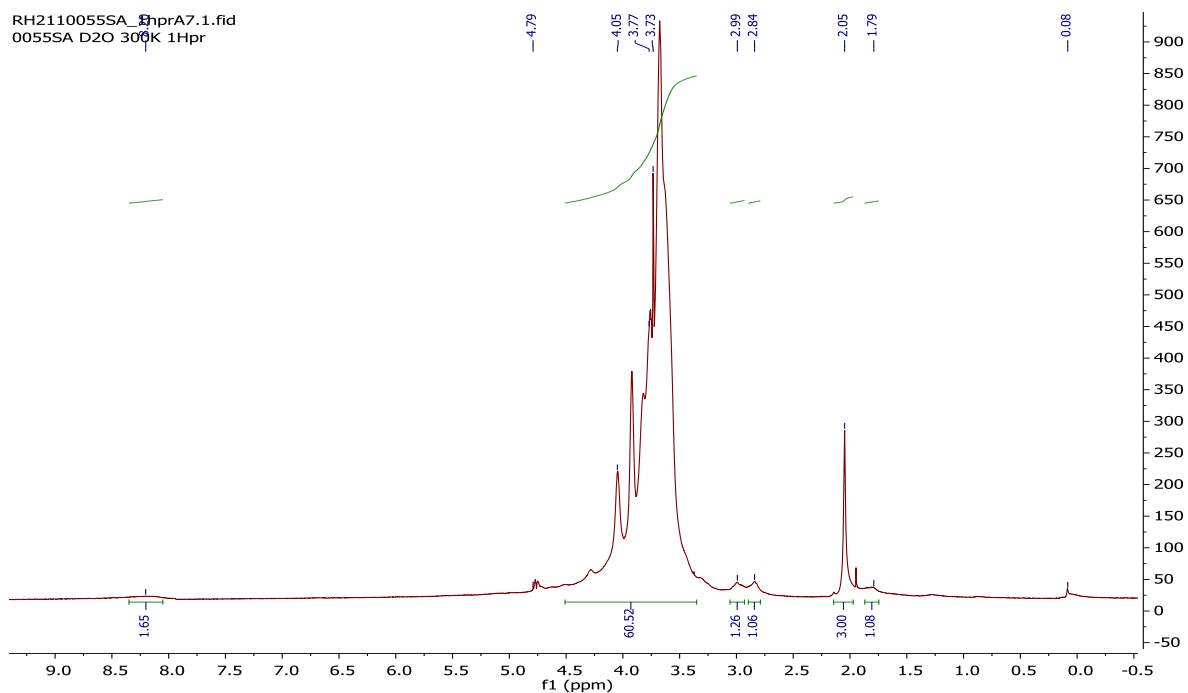


**Figure S14.**  $^1\text{H}$  NMR (500 MHz,  $\text{D}_2\text{O}$ ) of  $\text{hPG}_{2600}\text{-SA}$ ,  $\delta$ : 7.99 (bs, 1H, triazolyl proton), 4.51-3.28 [m, 9H (SA), dPG backbone], 2.84 (bs, 1H, SA H-3e), 2.05 (s, 3H, NHAc), 1.79 (bs, 1H, SA H-3a).

**Table S1.** Overview of hPGs used as scaffold for virus binding inhibitor

	$M_n^a$	$M_w^a$	$\bar{D}^a$	DB <sup>b</sup>	$d^c$	$\zeta$ -pot. <sup>d</sup>
sample	[kDa]	[kDa]	[-]	[%]	[nm]	[mV]
hPG <sub>10</sub>	6.9	10.9	1.66	60	6.2 ± 5.7	-3.9 ± 0.7
hPG <sub>100</sub>	100.6	126	1.26	53	8.5 ± 4.1	-5.2 ± 2.0
hPG <sub>500</sub>	509	549	1.08	57	13.0 ± 4.0	-3.9 ± 1.2
hPG <sub>2600</sub>	2554	3608	1.41	57	28.9 ± 14.9	9.5 ± 0.5

<sup>a</sup>)  $M_n$ ,  $M_w$  and dispersity ( $\bar{D}$ ) were determined by GPC using a MALLS detector; <sup>b</sup>) Degree of branching (DB) was determined from inverse gated <sup>13</sup>C NMR integrals;<sup>[9]</sup> <sup>c</sup>) hydrodynamic diameter (volume distribution, error half width, n=3) was investigated by DLS measurements 1 mg mL<sup>-1</sup> sample concentration in PBS buffer; <sup>d</sup>) Zeta-potential measurements 1 mg mL<sup>-1</sup> in 10 mM phosphate buffer solution (error standard deviation, n=5)

**Table S2.** Overview functionalization of hPG based binding inhibitor

	azidation		sulfation			click sialic acid
	N <sub>3</sub>	yield	SO <sub>4</sub>	N <sub>3</sub>	yield	yield
	[mol%]	[%]	[mol%]	[mol%]	[%]	[%]
<b>hPG<sub>10</sub>-SA-SO<sub>4</sub></b>	7.2	98.6	7.2	7.0	61.5	95.6
<b>hPG<sub>100</sub>-SA-SO<sub>4</sub></b>	5.0	91.0	5.0	5.5	81.9	77.3
<b>hPG<sub>500</sub>-SA-SO<sub>4</sub></b>	6.1	86.8	3.9	5.7	78.8	97.8
<b>hPG<sub>2600</sub>-SA-SO<sub>4</sub></b>			5.0	5.6	97.7	99.0
<b>hPG<sub>2600</sub>-SA</b>	5.7	68.4	-	-	-	99.5
<b>hPG<sub>2600</sub>-SO<sub>4</sub></b>	-	-	4.3	-	81.4	-

percentage of functionalization are based on elemental analysis (see Table S3)

**Table S3.** Overview elemental analysis data after each functionalization

	azidation				
	C	H	O	N	S
	[%]	[%]	[%]	[%]	[%]
<b>hPG<sub>10</sub>-N<sub>3</sub></b>	46.57 ± 0.27	8.02 ± 0.06	n.a.	3.99 ± 0.04	0.005 ± 0.002
<b>hPG<sub>100</sub>-N<sub>3</sub></b>	47.85 ± 0.04	7.99 ± 0.01	n.a.	2.83 ± 0.03	0.000 ± 0
<b>hPG<sub>500</sub>-N<sub>3</sub></b>	47.40 ± 0.05	7.56 ± 0.06	n.a.	3.36 ± 0.003	0.000 ± 0
<b>hPG<sub>2600</sub>-N<sub>3</sub></b>	46.79 ± 0.17	9.94 ± 0.03	n.a.	3.19 ± 0.02	0.007 ± 0.001
	sulfation				
	C	H	O	N	S
	[%]	[%]	[%]	[%]	[%]
<b>hPG<sub>10</sub>-N<sub>3</sub>-SO<sub>4</sub></b>	45.33 ± 0.15	7.79 ± 0.03	n.a.	3.82 ± 0.01	2.76 ± 0.05
<b>hPG<sub>100</sub>-N<sub>3</sub>-SO<sub>4</sub></b>	44.60 ± 0.04	7.61 ± 0.08	n.a.	2.864 ± 0.05	2.004 ± 0.001
<b>hPG<sub>500</sub>-N<sub>3</sub>-SO<sub>4</sub></b>	45.90 ± 0.04	7.58 ± 0.11	n.a.	2.989 ± 0.01	1.549 ± 0.04
<b>hPG<sub>2600</sub>-N<sub>3</sub>-SO<sub>4</sub></b>	44.83 ± 0.04	8.38 ± 0.03	n.a.	2.862 ± 0.01	1.977 ± 0.01
<b>hPG<sub>2600</sub>-SO<sub>4</sub></b>	46.71 ± 0.13	7.51 ± 0.02	n.a.	0.001 ± 0	1.720 ± 0.02
	click sialic acid				
	C	H	O	N	S
	[%]	[%]	[%]	[%]	[%]
<b>hPG<sub>10</sub>-SA-SO<sub>4</sub></b>	42.60 ± 0.43	8.46 ± 0.25	n.a.	3.85 ± 0.01	3.60 ± 0.09
<b>hPG<sub>100</sub>-SA-SO<sub>4</sub></b>	43.30 ± 0.14	7.00 ± 0.02	n.a.	3.07 ± 0.01	2.72 ± 0.001
<b>hPG<sub>500</sub>-SA-SO<sub>4</sub></b>	45.25 ± 0.01	7.96 ± 0.01	n.a.	3.15 ± 0.03	2.64 ± 0.01
<b>hPG<sub>2600</sub>-SA-SO<sub>4</sub></b>	44.68 ± 0.12	6.97 ± 0.02	n.a.	3.00 ± 0.004	3.06 ± 0.01
<b>hPG<sub>2600</sub>-SA</b>	45.66 ± 0.06	6.99 ± 0.01	n.a.	3.11 ± 0.02	2.00 ± 0.003

Given error is the standard deviation ( $n \geq 2$ )

### 3 References

- [1] Ogura, H.; Furuhashi, K.; Itoh, M.; Shitori, Y., *Carbohydrate Research* **1986**, *158*, 37-51. DOI 10.1016/0008-6215(86)84004-6.
- [2] Gan, Z. H.; Roy, R., *Canadian Journal of Chemistry-Revue Canadienne De Chimie* **2002**, *80* (8), 908-916. DOI 10.1139/v02-053.
- [3] Anilkumar, P.; Lawson, T. B.; Abbina, S.; Mäkelä, J. T.; Sabatelle, R. C.; Takeuchi, L. E.; Snyder, B. D.; Grinstaff, M. W.; Kizhakkedathu, J. N., *Nature Communications* **2020**, *11* (1), 1-9.
- [4] Müller, M.; Lauster, D.; Wildenauer, H. H. K.; Herrmann, A.; Block, S., *Nano Lett* **2019**, *19* (3), 1875-1882. DOI 10.1021/acs.nanolett.8b04969.
- [5] Lee, D. W.; Hsu, H. L.; Bacon, K. B.; Daniel, S., *PLoS One* **2016**, *11* (10), e0163437. DOI 10.1371/journal.pone.0163437.
- [6] Bally, M.; Gunnarsson, A.; Svensson, L.; Larson, G.; Zhdanov, V. P.; Hook, F., *Phys Rev Lett* **2011**, *107* (18), 188103. DOI 10.1103/PhysRevLett.107.188103.
- [7] Nie, C.; Parshad, B.; Bhatia, S.; Cheng, C.; Stadtmüller, M.; Oehrl, A.; Kerkhoff, Y.; Wolff, T.; Haag, R., *Angewandte Chemie International Edition* **2020**.
- [8] Harris, A.; Cardone, G.; Winkler, D. C.; Heymann, J. B.; Brecher, M.; White, J. M.; Steven, A. C., *Proc Natl Acad Sci U S A* **2006**, *103* (50), 19123-7. DOI 10.1073/pnas.0607614103.
- [9] Sunder, A.; Hanselmann, R.; Frey, H.; Mülhaupt, R., Controlled synthesis of hyperbranched polyglycerols by ring-opening multibranching polymerization. *Macromolecules* **1999**, *32* (13), 4240-4246.

## 4 Summary and conclusion

This work focused on the development of mucin-inspired virus binding inhibitors and their influence on the multivalent binding process of influenza A viruses (IAVs). New approaches of influenza virus inhibition are required, due to continuous mutations of influenza viruses by antigenic drift and shift, which lead to a decreased efficiency or resistance of currently used monovalent antiviral drugs. To this end, hyperbranched polyglycerols (hPG) were functionalized with typical terminal functional groups occurring in mucins: sialic acid and sulfate moieties. As recent theoretical investigations indicated a strong impact of inhibitor size on inhibitor efficiency,<sup>[163]</sup> the polymeric scaffold was systematically varied in size bridging 2 to 3 order of magnitudes in molecular weight (10 kDa to 2600 kDa). The inhibition efficiency was tested with HAI assay and cell binding experiments. Neither these methods nor other established methods like glycan micro array, BLI and AFM are able to detect the induced change of the multivalent virus-receptor binding interaction by the addition of inhibitor. Hence, the establishment of a new approach was necessary to monitor inhibitor-induced changes of multivalent virus-receptor interaction.

This goal was accomplished in the first project, in which a TIRF-based assay for investigation of multivalent IAV binding events was developed. Here, the binding of single IAVs to sialic acid containing GD1a receptors within a fluid phase-supported lipid bilayer (SLB, serving as artificial membrane) out of phosphatidylcholine (POPC) lipids was investigated. As expected, an increasing content of GD1a receptors within the SLB led to higher number of binding viruses (= higher attachment rate) and at a certain GD1a concentration the attachment rate saturated. The analysis of the virus mobility (2D diffusion) of bound IAVs was used to deconvolute the residence time distribution from valency effects. It was hypothesized that bound IAVs with high average binding valency show slow and IAVs with low average binding valency fast diffusion coefficients. By sorting the IAVs binding events in similar diffusion coefficient ranges (= same average binding valency) the detachment rate distributions for each average binding valency were derived. The detachment rate distribution showed the expected decrease in detachment rate with increasing valency but also exposed an unexpected peak with elevated detachment rates at a certain average valency. The detachment rate peak decreased in a dose-dependent manner with the addition of zanamivir, a monovalent neuraminidase (NA) inhibitor. This indicated that the interplay of hemagglutinin (HA) and NA was



responsible for the peak and due to the NA inhibitor, the balance was shifted to HA interactions. Additionally, the attachment rate increased in the presence of NA inhibitor. This powerful method was used to characterize the influence of mucin-inspired-binding inhibitors to IAV-binding processes in project 3.

In the second project, an automated solvent-free method was established to synthesize hyperbranched polymers, which served as a multivalent scaffold for the synthesis of mucin-inspired virus inhibitors. The polymerization was performed with slow monomer addition and controlled by online-monitoring of the torque value of the anchor stirrer. This investigation showed that the torque value can be used as indirect indicator for the molecular weight of the hPG in the reactor. Since the molecular weight of the polymer increases with the amount of monomer, the viscosity increases as well as the mass in the reactor. Due to these two factors, an increasing force to stir (torque) is necessary to keep the stir frequency constant. The relation between measured torque and the corresponding molecular weight was determined empirically in terms of a calibration curve. Knowing this relation, an automated, reproducible method was established to synthesize hPGs with defined molecular weights.

The third project focused on the synthesis and characterization of mucin-inspired virus binding inhibitors with different sizes (ranging between 10 to 2600 kDa). Small hPG (10 kDa) was provided by the solvent-free polymerization method out of project 2. Higher molecular weights of hPG were synthesized using a recently developed two-step synthesis approach. Each hPG was functionalized with sialic acid (5 mol%) and sulfate (5 mol%) in a multivalent fashion. The highest molecular weight meets the size of natural mucins (MDa range) and resulted after the functionalization in a mucin-inspired virus-binding inhibitor. The investigated binding inhibition in the HAI assay and  $IC_{50}$  value of the TIRF assay-derived attachment rate showed enhanced inhibition with increasing inhibitor size. The most effective was the mucin-inspired virus binding inhibitor based on the 2600 kDa hPG scaffold. Interestingly, the TIRF measurements revealed a biphasic binding behavior. An unexpected attachment rate increase at low inhibitor concentrations and an expected decrease at high inhibitor concentrations were observed. This phenomenon was verified by binding of IAVs to MDCK-II cells. The biphasic binding behavior indicated that the inhibitor binds preferably to NA of the IAV at low inhibitor concentrations, resulting in increased virus attachment to the receptors in the SLB (higher attachment-rate). At higher inhibitor concentrations, the inhibitor also binds to HA and causes a decrease in attachment of IAV (lower attachment rate). The effect can be

explained with higher affinities of NA to sialic acids compared the affinity of HA to sialic acids and supports the idea that NA also contributes to the attachment process.

## 5 Outlook

This work demonstrated the high inhibition efficiency of MDa-sized, mucin-inspired virus-binding inhibitors. Although only being demonstrated using IAVs, the functionalization of the mucin-inspired inhibitors exhibits two chemical groups often involved in virus binding, sialic acid and sulfate. This suggests broad-band activity for a variety of different viruses, including vesicular stomatitis virus (VSV), herpes simplex virus (HSV), and respiratory syncytial virus (RSV), which should be assessed in future experiments. Preliminary measurements probing VSV already showed efficient inhibition by the mucin-inspired virus binding inhibitor. Currently, the synthesized mucin-inspired binding inhibitors mimic the size and the surface functionalization of mucins. In order to get even closer to the architecture of mucins, their shape should be mimicked by the inhibitor as well. Natural mucins appear as elongated chains due to the high glycosylation. Hence, the inhibition efficiency of MDa-sized, linearly dendronized polymer architectures is of high interest, in particular, as the impact of inhibitor shape on the inhibition efficiency is yet unknown.

Further, the TIRF-based assay turned out to be a powerful tool because it allowed new insights in the mode of action of inhibitors. Since, this assay is not limited to IVAs, it could be established as generic tool for the characterization of virus-receptor interactions and how the interaction is changed by the addition of inhibitors.

## 6 Zusammenfassung

Diese Arbeit beschreibt die Entwicklung von Mucin-inspirierten Virenbindungsinhibitoren und deren Einfluss auf den multivalenten Bindungsprozess von Influenza A Viren (IAVs). Neue Herangehensweisen für die Inhibition von Influenza Viren sind nötig, da die kontinuierliche Mutation von Influenza Viren durch Antigendrift und -shift häufig zu einer niedrigeren Effizienz oder sogar Resistenz von den zurzeit benutzten monovalenten antiviralen Wirkstoffen führt. Zu diesem Zweck wurden hochverzweigte Polyglycerole mit typischen in Mucinen vorkommenden terminalen funktionellen Gruppen, Sialinsäuren und Sulfatgruppen, funktionalisiert. Da kürzlich theoretische Untersuchungen einen starken Einfluss der Inhibitorengröße aufgezeigt haben, wurde das Polymergerüst systematisch in der Größe so variiert, dass das Molekulargewicht 2 bis 3 Größenordnungen umfasst (10 kDa bis 2600 kDa). Die Inhibitoreffektivität wurde mit dem Hämagglutination Inhibition (HAI) Test und Zellbindungsexperimenten untersucht. Diese Methoden und auch andere etablierte Methoden wie Glykan-Mikroarray, Bio-Schicht-Interferometrie (BLI) oder Rasterkraftmikroskopie ermöglichen nicht, die Veränderung der multivalenten Virus-Rezeptor-Wechselwirkung durch Zugabe der Inhibitoren zu messen.

Im ersten Projekt wurde ein Assay basierend auf Interne Totalreflexionsfluoreszenzmikroskopie (TIRF) für die Untersuchung von multivalenten IAV Bindungsvorgängen entwickelt. Hierbei wurden Bindungsvorgänge von einzelnen Viren an GD1a Rezeptoren mit Sialinsäuren innerhalb einer festkörperunterstützten Lipiddoppelschicht aus Phosphatidylcholin (POPC; in Flüssigphase) untersucht. Wie erwartet führte eine höhere GD1a Rezeptorkonzentration in der Lipiddoppelschicht zu einer größeren Anzahl an bindenden Viren (höhere Anbindungsrate) und ab einer bestimmten GD1a Konzentration war die Anbindungsrate abgesättigt. Die Analyse der Virusmobilität (2D Diffusion) von gebundenen Viren wurde verwendet, um die Verteilung der Verweildauer von den Valenzeffekten zu bereinigen. Die Hypothese war, dass gebundene Viren mit einer höheren Bindungsvaleanz langsamere und IAVs mit niedrigeren Bindungsvaleenzen schnellere Diffusionskoeffizienten aufweisen. Mit der Sortierung der IAV Bindungsvorgänge in ähnliche Diffusionskoeffizientenbereiche (= gleiche mittlere Bindungsvaleanz) konnte die Ablöseratenverteilung für jede mittlere Bindungsvaleanz abgeleitet werden. Die Ablöseratenverteilung zeigte eine erwartete Verminderung der Ablöserate mit steigender Valenz, aber deckte auch einen

unerwarteten Peak mit erhöhter Ablöserate bei einer bestimmten Valenz auf. Der Ablöseratenpeak konnte mit der Zugabe von Zanamivir, einen monovalenten Neuraminidase-Inhibitor, dosisabhängig verringert werden. Das zeigt an, dass das Zusammenspiel von Hämagglutinin (HA) und Neuraminidase (NA) verantwortlich für den Peak ist und durch den NA-Inhibitor das Gleichgewicht zu HA Wechselwirkungen verschoben wurde. Zusätzlich erhöhte sich die Anbindungsrate in Anwesenheit von NA-Inhibitoren. Diese leistungsfähige Methode wurde benutzt, um den Einfluss von Mucin-inspirierten Bindungsinhibitoren auf den Bindungsvorgang von IAVs in Projekt 3 zu charakterisieren.

Im zweiten Projekt wurde eine automatisierte lösemittelfreie Methode erarbeitet, um hyperverzweigtes Polyglycerol zu synthetisieren, welches als Gerüst für die Synthese von Mucin-inspirierten Virenbindungsinhibitoren dient. Die Polymerisation wurde mit einer langsamen Monomerzugabe durchgeführt und über Online-Überwachung des Drehmomentes des Ankerrührers gesteuert. Das Drehmoment kann als indirekter Indikator für das Molekulargewicht für das im Reaktor befindlichen hPG benutzt werden. Da sich das Molekulargewicht mit steigender Zugabe von Monomer erhöht, nimmt die Viskosität und die Masse in dem Reaktor zu. Wegen diesen zwei Faktoren ist eine erhöhte Rührkraft (Drehmoment) nötig, um die Drehfrequenz des Rührers konstant zu halten. Das Verhältnis der gemessenen Drehmomentwerte und der dazugehörigen Molekulargewichte wurden empirisch ermittelt. Mit dem Wissen des Verhältnisses konnte eine automatisierte, reproduzierbare Methode zur Synthese von hPG mit definiertem Molekulargewicht erstellt werden, das Grundlage für das dritte Projekt ist.

Das dritte Projekt fokussierte sich auf die Synthese und Charakterisierung von Mucin-inspirierten Virusbindungsinhibitoren mit unterschiedlichen Größen (im Bereich von 10 kDa bis 2600 kDa). Kleines hPG (10 kDa) wurde von der lösemittelfreien Polymerisierungsmethode aus Projekt zwei bereitgestellt.<sup>[167]</sup> Höhere Molekulargewichte wurden mit einer kürzlich von Kizhakkedathu et al. entwickelten Zweistufensynthese hergestellt. Jedes hPG wurde mit Sialinsäure (5 mol%) and Sulfatgruppen (5 mol%) in multivalenter Weise funktionalisiert. Das höchste Molekulargewicht erreicht die Größe von natürlichen Mucinen (MDa Bereich) und ergab nach der Funktionalisierung ein Mucin-inspirierten Virenbindungsinhibitor. Die untersuchten Bindungsinhibitoren im HAI Assay und die ermittelten IC<sub>50</sub> Werte des TIRF Assays zeigten eine gesteigerte Inhibition mit zunehmender Inhibitorengröße. Am effektivsten war der Mucin-inspirierte Virenbindungsinhibitor basierend auf dem 2600 kDa hPG Gerüst. Interessanterweise

deckten die TIRF-Messungen ein biphasisches Bindungsverhalten auf, bei dem ein unerwarteter Anstieg der Anbindungsrate bei geringen InhibitorKonzentrationen und die erwartete Abnahme bei höheren InhibitorKonzentrationen beobachtet wurde. Dieses Phänomen wurde mit Bindungsexperimenten von IAV an MDCK-II Zellen verifiziert. Das biphasische Verhalten legt nahe, dass der Inhibitor bevorzugt an NA der IAVs bei geringen InhibitorKonzentrationen bindet und resultiert in einer erhöhten viralen Anbindungsrate an den Rezeptoren in der Lipiddoppelschicht. Bei höheren Konzentrationen bindet der Inhibitor auch an HA und verursacht eine Abnahme der viralen Anbindungsrate. Der Effekt kann durch eine höhere Affinität von NA zu Sialinsäure verglichen mit HA zu Sialinsäure erklärt werden. Diese Beobachtung unterstützt die Hypothese, dass NA auch bei dem Bindungsprozess an die Zellmembrane mitwirkt.

## 7 References

- [1] Ventura, C. V.; Maia, M.; Bravo-Filho, V.; Góis, A. L.; Belfort, R., Zika virus in Brazil and macular atrophy in a child with microcephaly. *The Lancet* **2016**, *387* (10015), 228.
- [2] Neumann, G.; Noda, T.; Kawaoka, Y., Emergence and pandemic potential of swine-origin H1N1 influenza virus. *Nature* **2009**, *459* (7249), 931-939.
- [3] Hoffmann, M.; Kleine-Weber, H.; Schroeder, S.; Krüger, N.; Herrler, T.; Erichsen, S.; Schiergens, T. S.; Herrler, G.; Wu, N.-H.; Nitsche, A., SARS-CoV-2 Cell Entry Depends on ACE2 and TMPRSS2 and Is Blocked by a Clinically Proven Protease Inhibitor. *Cell* **2020**.
- [4] Lee, N.; McGeer, A., The starting line for COVID-19 vaccine development. *Lancet (London, England)* **2020**.
- [5] Krause, P.; Fleming, T. R.; Longini, I.; Henao-Restrepo, A. M.; Peto, R.; Dean, N.; Halloran, M.; Huang, Y.; Fleming, T.; Gilbert, P., COVID-19 vaccine trials should seek worthwhile efficacy. *The Lancet* **2020**, *396* (10253), 741-743.
- [6] Skowronski, D. M.; Janjua, N. Z.; De Serres, G.; Sabaiduc, S.; Eshaghi, A.; Dickinson, J. A.; Fonseca, K.; Winter, A.-L.; Gubbay, J. B.; Krajdén, M., Low 2012–13 influenza vaccine effectiveness associated with mutation in the egg-adapted H3N2 vaccine strain not antigenic drift in circulating viruses. *PloS one* **2014**, *9* (3), e92153.
- [7] Wu, Y.; Gao, F.; Qi, J.; Bi, Y.; Fu, L.; Mohan, S.; Chen, Y.; Li, X.; Pinto, B. M.; Vavricka, C. J., Resistance to mutant group 2 influenza virus neuraminidases of an oseltamivir-zanamivir hybrid inhibitor. *Journal of virology* **2016**, *90* (23), 10693-10700.
- [8] Irwin, K. K.; Renzette, N.; Kowalik, T. F.; Jensen, J. D., Antiviral drug resistance as an adaptive process. *Virus evolution* **2016**, *2* (1).
- [9] Yang, J.; Li, M.; Shen, X.; Liu, S., Influenza A virus entry inhibitors targeting the hemagglutinin. *Viruses* **2013**, *5* (1), 352-373.
- [10] Mammen, M.; Choi, S.-K.; Whitesides, G. M., Polyvalent interactions in biological systems: implications for design and use of multivalent ligands and inhibitors. *Angewandte Chemie International Edition* **1998**, *37* (20), 2754-2794.
- [11] Linden, S.; Sutton, P.; Karlsson, N.; Korolik, V.; McGuckin, M., Mucins in the mucosal barrier to infection. *Mucosal immunology* **2008**, *1* (3), 183-197.
- [12] Zanin, M.; Baviskar, P.; Webster, R.; Webby, R., The interaction between respiratory pathogens and mucus. *Cell host & microbe* **2016**, *19* (2), 159-168.
- [13] Yang, X.; Forier, K.; Steukers, L.; Van Vlierberghe, S.; Dubrue, P.; Braeckmans, K.; Glorieux, S.; Nauwynck, H. J., Immobilization of pseudorabies virus in porcine tracheal respiratory mucus revealed by single particle tracking. *PloS one* **2012**, *7* (12), e51054.
- [14] Lai, S. K.; Hida, K.; Shukair, S.; Wang, Y.-Y.; Figueiredo, A.; Cone, R.; Hope, T. J.; Hanes, J., Human immunodeficiency virus type 1 is trapped by acidic but not by neutralized human cervicovaginal mucus. *Journal of virology* **2009**, *83* (21), 11196-11200.
- [15] Lieleg, O.; Lieleg, C.; Bloom, J.; Buck, C. B.; Ribbeck, K., Mucin Biopolymers As Broad-Spectrum Antiviral Agents. *Biomacromolecules* **2012**, *13* (6), 1724-1732.
- [16] Zumbro, E.; Alexander-Katz, A., Influence of Binding Site Affinity Patterns on Binding of Multivalent Polymers. *ACS omega* **2020**.

- [17] Fasting, C.; Schalley, C. A.; Weber, M.; Seitz, O.; Hecht, S.; Kokschi, B.; Dervede, J.; Graf, C.; Knapp, E. W.; Haag, R., Multivalency as a chemical organization and action principle. *Angewandte Chemie International Edition* **2012**, *51* (42), 10472-10498.
- [18] Klinth, J. E.; Castelain, M.; Uhlin, B. E.; Axner, O., The influence of pH on the specific adhesion of P piliated Escherichia coli. *PLoS One* **2012**, *7* (6), e38548.
- [19] Levine, P. M.; Carberry, T. P.; Holub, J. M.; Kirshenbaum, K., Crafting precise multivalent architectures. *MedChemComm* **2013**, *4* (3), 493-509.
- [20] Glick, G. D.; Knowles, J. R., Molecular recognition of bivalent sialosides by influenza virus. *Journal of the American Chemical Society* **1991**, *113* (12), 4701-4703.
- [21] Glick, G. D.; Toogood, P.; Wiley, D. C.; Skehel, J. J.; Knowles, J., Ligand recognition by influenza virus. The binding of bivalent sialosides. *Journal of Biological Chemistry* **1991**, *266* (35), 23660-23669.
- [22] Achazi, K.; Haag, R.; Ballauff, M.; Dervede, J.; Kizhakkedathu, J. N.; Maysinger, D.; Multhaupt, G., Understanding the interaction of polyelectrolyte architectures with proteins and biosystems. *Angewandte Chemie* **2020**.
- [23] Xu, X.; Ballauff, M., Interaction of lysozyme with a dendritic polyelectrolyte: Quantitative analysis of the free energy of binding and comparison to molecular dynamics simulations. *The Journal of Physical Chemistry B* **2019**, *123* (39), 8222-8231.
- [24] Kitov, P. I.; Bundle, D. R., On the nature of the multivalency effect: a thermodynamic model. *Journal of the American Chemical Society* **2003**, *125* (52), 16271-16284.
- [25] Xiong, X.; Coombs, P. J.; Martin, S. R.; Liu, J.; Xiao, H.; McCauley, J. W.; Locher, K.; Walker, P. A.; Collins, P. J.; Kawaoka, Y., Receptor binding by a ferret-transmissible H5 avian influenza virus. *Nature* **2013**, *497* (7449), 392-396.
- [26] Samji, T., Influenza A: understanding the viral life cycle. *The Yale journal of biology and medicine* **2009**, *82* (4), 153.
- [27] Li, S.; Sieben, C.; Ludwig, K.; Höfer, C. T.; Chiantia, S.; Herrmann, A.; Eghiaian, F.; Schaap, I. A., pH-Controlled two-step uncoating of influenza virus. *Biophysical journal* **2014**, *106* (7), 1447-1456.
- [28] Rossman, J. S.; Lamb, R. A., Influenza virus assembly and budding. *Virology* **2011**, *411* (2), 229-236.
- [29] Iuliano, A. D.; Roguski, K. M.; Chang, H. H.; Muscatello, D. J.; Palekar, R.; Tempia, S.; Cohen, C.; Gran, J. M.; Schanzer, D.; Cowling, B. J., Estimates of global seasonal influenza-associated respiratory mortality: a modelling study. *The Lancet* **2018**, *391* (10127), 1285-1300.
- [30] Taubenberger, J. K.; Morens, D. M., Influenza: the once and future pandemic. *Public health reports* **2010**, *125* (3\_suppl), 15-26.
- [31] Hsieh, Y.-C.; Wu, T.-Z.; Liu, D.-P.; Shao, P.-L.; Chang, L.-Y.; Lu, C.-Y.; Lee, C.-Y.; Huang, F.-Y.; Huang, L.-M., Influenza pandemics: past, present and future. *Journal of the Formosan Medical Association* **2006**, *105* (1), 1-6.
- [32] McAuley, J.; Gilbertson, B.; Trifkovic, S.; Brown, L. E.; McKimm-Breschkin, J., Influenza virus neuraminidase structure and functions. *Frontiers in microbiology* **2019**, *10*, 39.
- [33] Stevens, J.; Blixt, O.; Paulson, J.; A Wilson, I., *Glycan microarray technologies: Tools to survey host specificity of influenza viruses*. 2006; Vol. 4, p 857-64.
- [34] Nayak, D. P.; Hui, E. K.-W.; Barman, S., Assembly and budding of influenza virus. *Virus research* **2004**, *106* (2), 147-165.



- [35] Moules, V.; Ferraris, O.; Terrier, O.; Giudice, E.; Yver, M.; Rolland, J.-P.; Bouscambert-Duchamp, M.; Bergeron, C.; Ottmann, M.; Fournier, E., In vitro characterization of naturally occurring influenza H3NA– viruses lacking the NA gene segment: Toward a new mechanism of viral resistance? *Virology* **2010**, *404* (2), 215-224.
- [36] Vahey, M. D.; Fletcher, D. A., Low-fidelity assembly of influenza A virus promotes escape from host cells. *Cell* **2019**, *176* (1-2), 281-294. e19.
- [37] Jie, Y.; Shuwen, L.; Lanying, D.; Shibo, J., A new role of neuraminidase (NA) in the influenza virus life cycle: implication for developing NA inhibitors with novel mechanism of action. *Reviews in Medical Virology* **2016**, *26* (4), 242-250.
- [38] Harris, A.; Cardone, G.; Winkler, D. C.; Heymann, J. B.; Brecher, M.; White, J. M.; Steven, A. C., Influenza virus pleiomorphy characterized by cryoelectron tomography. *Proceedings of the National Academy of Sciences* **2006**, *103* (50), 19123-19127.
- [39] Ciminski, K.; Pfaff, F.; Beer, M.; Schwemmler, M., Bats reveal the true power of influenza A virus adaptability. *PLoS Pathogens* **2020**, *16* (4), e1008384.
- [40] Ciminski, K.; Ran, W.; Gorka, M.; Lee, J.; Malmlov, A.; Schinköthe, J.; Eckley, M.; Murrieta, R. A.; Aboellail, T. A.; Campbell, C. L., Bat influenza viruses transmit among bats but are poorly adapted to non-bat species. *Nature microbiology* **2019**, *4* (12), 2298-2309.
- [41] Bedford, T.; Riley, S.; Barr, I. G.; Broor, S.; Chadha, M.; Cox, N. J.; Daniels, R. S.; Gunasekaran, C. P.; Hurt, A. C.; Kelso, A., Global circulation patterns of seasonal influenza viruses vary with antigenic drift. *Nature* **2015**, *523* (7559), 217-220.
- [42] Bedford, T.; Suchard, M. A.; Lemey, P.; Dudas, G.; Gregory, V.; Hay, A. J.; McCauley, J. W.; Russell, C. A.; Smith, D. J.; Rambaut, A., Integrating influenza antigenic dynamics with molecular evolution. *eLife* **2014**, *3*, e01914.
- [43] Chan, K.-H.; Sridhar, S.; Zhang, R. R.; Chu, H.; Fung, A. Y.-F.; Chan, G.; Chan, J. F.-W.; To, K. K.-W.; Hung, I. F.-N.; Cheng, V. C.-C., Factors affecting stability and infectivity of SARS-CoV-2. *Journal of Hospital Infection* **2020**.
- [44] Shinya, K.; Ebina, M.; Yamada, S.; Ono, M.; Kasai, N.; Kawaoka, Y., Influenza virus receptors in the human airway. *Nature* **2006**, *440* (7083), 435-436.
- [45] Hanson, J. E.; Sauter, N. K.; Skehel, J. J.; Wiley, D. C., Proton nuclear magnetic resonance studies of the binding of sialosides to intact influenza virus. *Virology* **1992**, *189* (2), 525-533.
- [46] Ralf, W.; Mikhail, M.; Hans-Dieter, K., Functional balance between haemagglutinin and neuraminidase in influenza virus infections. *Reviews in Medical Virology* **2002**, *12* (3), 159-166.
- [47] Cohen, M.; Zhang, X.-Q.; Senaati, H. P.; Chen, H.-W.; Varki, N. M.; Schooley, R. T.; Gagneux, P., Influenza A penetrates host mucus by cleaving sialic acids with neuraminidase. *Virology Journal* **2013**, *10* (1), 321.
- [48] Colman, P. M., Influenza virus neuraminidase: structure, antibodies, and inhibitors. *Protein Science* **1994**, *3* (10), 1687-1696.
- [49] Vahey, M. D.; Fletcher, D. A., Influenza A virus surface proteins are organized to help penetrate host mucus. *eLife* **2019**, *8*, e43764.
- [50] Richard, M.; Erny, A.; Care, B.; Traversier, A.; Barthelemy, M.; Hay, A.; Lin, Y. P.; Ferraris, O.; Lina, B., Rescue of a H3N2 influenza virus containing a deficient neuraminidase protein by a hemagglutinin with a low receptor-binding affinity. *PloS one* **2012**, *7* (5), e33880.
- [51] Campanero-Rhodes, M. A.; Smith, A.; Chai, W.; Sonnino, S.; Mauri, L.; Childs, R. A.; Zhang, Y.; Ewers, H.; Helenius, A.; Imberty, A., N-glycolyl GM1

- ganglioside as a receptor for simian virus 40. *Journal of virology* **2007**, *81* (23), 12846-12858.
- [52] Varghese, J. N.; Colman, P. M.; Van Donkelaar, A.; Blick, T. J.; Sahasrabudhe, A.; McKimm-Breschkin, J. L., Structural evidence for a second sialic acid binding site in avian influenza virus neuraminidases. *Proceedings of the National Academy of Sciences* **1997**, *94* (22), 11808-11812.
- [53] Amaro, R. E.; Jeong, P. U.; Huber, G.; Dommer, A.; Steven, A. C.; Bush, R. M.; Durrant, J. D.; Votapka, L. W., A computational assay that explores the hemagglutinin/neuraminidase functional balance reveals the neuraminidase secondary site as a novel anti-influenza target. *ACS central science* **2018**, *4* (11), 1570-1577.
- [54] Zhu, X.; McBride, R.; Nycholat, C. M.; Yu, W.; Paulson, J. C.; Wilson, I. A., Influenza virus neuraminidases with reduced enzymatic activity that avidly bind sialic acid receptors. *Journal of virology* **2012**, *86* (24), 13371-13383.
- [55] Wen, F.; Wan, X.-F., Influenza neuraminidase: Underrated role in receptor binding. *Trends in microbiology* **2019**, *27* (6), 477-479.
- [56] Shen, Z.; Lou, K.; Wang, W., New small-molecule drug design strategies for fighting resistant influenza A. *Acta Pharmaceutica Sinica B* **2015**, *5* (5), 419-430.
- [57] Cady, S. D.; Schmidt-Rohr, K.; Wang, J.; Soto, C. S.; DeGrado, W. F.; Hong, M., Structure of the amantadine binding site of influenza M2 proton channels in lipid bilayers. *Nature* **2010**, *463* (7281), 689-692.
- [58] Ison, M. G., Optimizing antiviral therapy for influenza: understanding the evidence. *Expert review of anti-infective therapy* **2015**, *13* (4), 417-425.
- [59] Li, T.; Chan, M. C.; Lee, N., Clinical implications of antiviral resistance in influenza. *Viruses* **2015**, *7* (9), 4929-4944.
- [60] Cheng, P. K.; To, A. P.; Leung, T. W.; Leung, P. C.; Lee, C. W.; Lim, W. W., Oseltamivir-and amantadine-resistant influenza virus A (H1N1). *Emerging infectious diseases* **2010**, *16* (1), 155.
- [61] Kiessling, L. L.; Gestwicki, J. E.; Strong, L. E., Synthetic multivalent ligands in the exploration of cell-surface interactions. *Current opinion in chemical biology* **2000**, *4* (6), 696-703.
- [62] Sigal, G. B.; Mammen, M.; Dahmann, G.; Whitesides, G. M., Polyacrylamides bearing pendant  $\alpha$ -sialoside groups strongly inhibit agglutination of erythrocytes by influenza virus: the strong inhibition reflects enhanced binding through cooperative polyvalent interactions. *Journal of the American Chemical Society* **1996**, *118* (16), 3789-3800.
- [63] Bhatia, S.; Hilsch, M.; Cuellar Camacho, J. L.; Ludwig, K.; Nie, C.; Parshad, B.; Wallert, M.; Block, S.; Lauster, D.; Böttcher, C., Adaptive flexible sialylated nanogels as highly potent influenza A virus inhibitors. *Angewandte Chemie International Edition* **2020**.
- [64] McCulloch, B.; Ho, V.; Hoarfrost, M.; Stanley, C.; Do, C.; Heller, W. T.; Segalman, R. A., Polymer chain shape of poly (3-alkylthiophenes) in solution using small-angle neutron scattering. *Macromolecules* **2013**, *46* (5), 1899-1907.
- [65] Jabbarzadeh, A.; Atkinson, J.; Tanner, R., Effect of molecular shape on rheological properties in molecular dynamics simulation of star, H, comb, and linear polymer melts. *Macromolecules* **2003**, *36* (13), 5020-5031.
- [66] Mark, J., Rubber elasticity. *Journal of Chemical Education* **1981**, *58* (11), 898-903.
- [67] Zacco, E.; Hütter, J.; Heier, J. L.; Mortier, J.; Seeberger, P. H.; Lepenies, B.; Kokschi, B., Tailored presentation of carbohydrates on a coiled coil-based scaffold

- for asialoglycoprotein receptor targeting. *ACS Chemical Biology* **2015**, *10* (9), 2065-2072.
- [68] Gerling-Driessen, U. I.; Mujkic-Ninnemann, N.; Ponader, D.; Schöne, D.; Hartmann, L.; Kokscho, B.; Gerling-Driessen, U.; Schöne, D.; Kokscho, B.; Ponader, D., Exploiting Oligo (amido amine) backbones for the multivalent presentation of coiled-coil peptides. *Biomacromolecules* **2015**, *16* (8), 2394-2402.
- [69] Verduzco, R.; Li, X.; Pesek, S. L.; Stein, G. E., Structure, function, self-assembly, and applications of bottlebrush copolymers. *Chemical Society Reviews* **2015**, *44* (8), 2405-2420.
- [70] Gao, H.; Matyjaszewski, K., Synthesis of molecular brushes by “grafting onto” method: combination of ATRP and click reactions. *Journal of the American Chemical Society* **2007**, *129* (20), 6633-6639.
- [71] Bolton, J.; Rzaev, J., Tandem RAFT-ATRP synthesis of polystyrene–poly (methyl methacrylate) bottlebrush block copolymers and their self-assembly into cylindrical nanostructures. *ACS Macro Letters* **2012**, *1* (1), 15-18.
- [72] Xia, Y.; Kornfield, J. A.; Grubbs, R. H., Efficient synthesis of narrowly dispersed brush polymers via living ring-opening metathesis polymerization of macromonomers. *Macromolecules* **2009**, *42* (11), 3761-3766.
- [73] Foster, J. C.; Radzinski, S. C.; Matson, J. B., Graft polymer synthesis by RAFT transfer-to. *Journal of Polymer Science Part A: Polymer Chemistry* **2017**, *55* (18), 2865-2876.
- [74] Rathgeber, S.; Pakula, T.; Wilk, A.; Matyjaszewski, K.; Beers, K. L., On the shape of bottle-brush macromolecules: Systematic variation of architectural parameters. *The Journal of chemical physics* **2005**, *122* (12), 124904.
- [75] Lee, C. C.; MacKay, J. A.; Fréchet, J. M.; Szoka, F. C., Designing dendrimers for biological applications. *Nature biotechnology* **2005**, *23* (12), 1517-1526.
- [76] Lundquist, J. J.; Toone, E. J., The cluster glycoside effect. *Chemical reviews* **2002**, *102* (2), 555-578.
- [77] Steffensen, M. B.; Simanek, E. E., Synthesis and manipulation of orthogonally protected dendrimers: building blocks for library synthesis. *Angewandte Chemie* **2004**, *116* (39), 5290-5292.
- [78] Jee, J.-A.; Spagnuolo, L. A.; Rudick, J. G., Convergent synthesis of dendrimers via the Passerini three-component reaction. *Organic letters* **2012**, *14* (13), 3292-3295.
- [79] Ornelas, C.; Pennell, R.; Liebes, L. F.; Weck, M., Construction of a well-defined multifunctional dendrimer for theranostics. *Organic letters* **2011**, *13* (5), 976-979.
- [80] Arseneault, M.; Wafer, C.; Morin, J.-F., Recent advances in click chemistry applied to dendrimer synthesis. *Molecules* **2015**, *20* (5), 9263-9294.
- [81] Sathiyaraj, S.; Vanjinathan, M.; Libni, G.; Subalakshmi, K.; Senthil Selvan, J.; Nasar, A. S., Synthesis, electrolyte properties and solar cell performance of hyperbranched poly (aryl-ether-urea) s. *Journal of Macromolecular Science, Part A* **2017**, *54* (12), 978-985.
- [82] Paulus, F.; Weiss, M. E.; Steinhilber, D.; Nikitin, A. N.; Schütte, C.; Haag, R., Anionic ring-opening polymerization simulations for hyperbranched polyglycerols with defined molecular weights. *Macromolecules* **2013**, *46* (21), 8458-8466.
- [83] Mathias, L. J.; Carothers, T. W., Hyperbranched poly (siloxysilanes). *Journal of the American Chemical Society* **1991**, *113* (10), 4043-4044.
- [84] Miravet, J. F.; Fréchet, J. M. J., New Hyperbranched Poly(siloxysilanes): Variation of the Branching Pattern and End-Functionalization. *Macromolecules* **1998**, *31* (11), 3461-3468.

- [85] Sunder, A.; Hanselmann, R.; Frey, H.; Mülhaupt, R., Controlled synthesis of hyperbranched polyglycerols by ring-opening multibranching polymerization. *Macromolecules* **1999**, *32* (13), 4240-4246.
- [86] Voit, B. I.; Lederer, A., Hyperbranched and Highly Branched Polymer Architectures - Synthetic Strategies and Major Characterization Aspects. *Chemical reviews* **2009**, *109* (11), 5924-5973.
- [87] Sunder, A.; Mülhaupt, R.; Haag, R.; Frey, H., Hyperbranched polyether polyols: a modular approach to complex polymer architectures. *Advanced Materials* **2000**, *12* (3), 235-239.
- [88] Dervede, J.; Rausch, A.; Weinhart, M.; Enders, S.; Tauber, R.; Licha, K.; Schirner, M.; Zügel, U.; von Bonin, A.; Haag, R., Dendritic polyglycerol sulfates as multivalent inhibitors of inflammation. *Proceedings of the National Academy of Sciences* **2010**, *107* (46), 19679-19684.
- [89] Bhatia, S.; Lauster, D.; Bardua, M.; Ludwig, K.; Angioletti-Uberti, S.; Popp, N.; Hoffmann, U.; Paulus, F.; Budt, M.; Stadtmüller, M.; Wolff, T.; Hamann, A.; Böttcher, C.; Herrmann, A.; Haag, R., Linear polysialoside outperforms dendritic analogs for inhibition of influenza virus infection in vitro and in vivo. *Biomaterials* **2017**, *138*, 22-34.
- [90] Herzberger, J.; Niederer, K.; Pohlit, H.; Seiwert, J.; Worm, M.; Wurm, F. R.; Frey, H., Polymerization of ethylene oxide, propylene oxide, and other alkylene oxides: synthesis, novel polymer architectures, and bioconjugation. *Chemical reviews* **2016**, *116* (4), 2170-2243.
- [91] Syrett, J. A.; Haddleton, D. M.; Whittaker, M. R.; Davis, T. P.; Boyer, C., Functional, star polymeric molecular carriers, built from biodegradable microgel/nanogel cores. *Chemical Communications* **2011**, *47* (5), 1449-1451.
- [92] Li, W.; Matyjaszewski, K., Uniform PEO star polymers synthesized in water via free radical polymerization or atom transfer radical polymerization. *Macromolecular rapid communications* **2011**, *32* (1), 74-81.
- [93] McKenzie, T. G.; Wong, E. H.; Fu, Q.; Lam, S. J.; Dunstan, D. E.; Qiao, G. G., Highly efficient and versatile formation of biocompatible star polymers in pure water and their stimuli-responsive self-assembly. *Macromolecules* **2014**, *47* (22), 7869-7877.
- [94] Jiang, G.; Xu, H., Synthesis and evaluation of a star amphiphilic block copolymer from poly ( $\epsilon$ -caprolactone) and poly (ethylene oxide) as load and release carriers for guest molecules. *Journal of applied polymer science* **2010**, *118* (3), 1372-1379.
- [95] Huin, C.; Eskandani, Z.; Badi, N.; Farcas, A.; Bennevault-Celton, V.; Guégan, P., Anionic ring-opening polymerization of ethylene oxide in DMF with cyclodextrin derivatives as new initiators. *Carbohydrate polymers* **2013**, *94* (1), 323-331.
- [96] Lam, S. J.; Sulistio, A.; Ladewig, K.; Wong, E. H.; Blencowe, A.; Qiao, G. G., Peptide-based star polymers as potential siRNA carriers. *Australian Journal of Chemistry* **2014**, *67* (4), 592-597.
- [97] MacDonald, R. C.; MacDonald, R. I.; Menco, B. Ph.M.; Takeshita, K.; Subbarao, N. K.; Hu, L., Small-volume extrusion apparatus for preparation of large, unilamellar vesicles *Biochimica et Biophysica Acta*. **1991**, *1061*, 297- 303.
- [98] Staudinger, H., Über polymerisation. *Berichte der deutschen chemischen Gesellschaft (A and B Series)* **1920**, *53* (6), 1073-1085.
- [99] Wang, W.; Schlüter, A. D., Synthetic 2D polymers: A critical perspective and a look into the future. *Macromolecular Rapid Communications* **2019**, *40* (1), 1800719.

- [100] Doycheva, M.; Berger-Nicoletti, E.; Wurm, F.; Frey, H., Rapid Synthesis and MALDI-ToF Characterization of Poly (ethylene oxide) Multiarm Star Polymers. *Macromolecular Chemistry and Physics* **2010**, *211* (1), 35-44.
- [101] Wilms, D.; Stiriba, S.-E.; Frey, H., Hyperbranched polyglycerols: from the controlled synthesis of biocompatible polyether polyols to multipurpose applications. *Accounts of chemical research* **2010**, *43* (1), 129-141.
- [102] Reuter, J. D.; Myc, A.; Hayes, M. M.; Gan, Z.; Roy, R.; Qin, D.; Yin, R.; Piehler, L. T.; Esfand, R.; Tomalia, D. A., Inhibition of viral adhesion and infection by sialic-acid-conjugated dendritic polymers. *Bioconjugate chemistry* **1999**, *10* (2), 271-278.
- [103] Authimoolam, S. P.; Dziubla, T. D., Biopolymeric Mucin and Synthetic Polymer Analogs: Their Structure, Function and Role in Biomedical Applications. *Polymers* **2016**, *8* (3), 71.
- [104] Fahy, J. V.; Dickey, B. F., Airway Mucus Function and Dysfunction. *New England Journal of Medicine* **2010**, *363* (23), 2233-2247.
- [105] Prydal, J.; Muir, M. K.; Dilly, P., Comparison of tear film thickness in three species determined by the glass fibre method and confocal microscopy. *Eye* **1993**, *7* (3), 472-475.
- [106] Rubin, B. K., Physiology of airway mucus clearance. *Respiratory care* **2002**, *47* (7), 761.
- [107] Jordan, N.; Newton, J.; PEARSON, J.; Allen, A., A novel method for the visualization of the in situ mucus layer in rat and man. *Clinical Science* **1998**, *95* (1), 97-106.
- [108] Atuma, C.; Strugala, V.; Allen, A.; Holm, L., The adherent gastrointestinal mucus gel layer: thickness and physical state in vivo. *American Journal of Physiology-Gastrointestinal and Liver Physiology* **2001**, *280* (5), G922-G929.
- [109] Cone, R. A., Barrier properties of mucus. *Advanced drug delivery reviews* **2009**, *61* (2), 75-85.
- [110] Powell, D. W., Ion and water transport in the intestine. In *Membrane Transport Processes in Organized Systems*, Springer: 1987; pp 175-212.
- [111] Salathe, M., Regulation of mammalian ciliary beating. *Annu. Rev. Physiol.* **2007**, *69*, 401-422.
- [112] Lai, S. K.; Wang, Y.-Y.; Wirtz, D.; Hanes, J., Micro-and macrorheology of mucus. *Advanced drug delivery reviews* **2009**, *61* (2), 86-100.
- [113] Bansil, R.; Turner, B. S., Mucin structure, aggregation, physiological functions and biomedical applications. *Current Opinion in Colloid & Interface Science* **2006**, *11* (2), 164-170.
- [114] Dekker, J.; Rossen, J. W. A.; Büller, H. A.; Einerhand, A. W. C., The MUC family: an obituary. *Trends in Biochemical Sciences* **2002**, *27* (3), 126-131.
- [115] Offner, G.; Troxler, R., Heterogeneity of high-molecular-weight human salivary mucins. *Advances in dental research* **2000**, *14* (1), 69-75.
- [116] Kramer, J. R.; Onoa, B.; Bustamante, C.; Bertozzi, C. R., Chemically tunable mucin chimeras assembled on living cells. *Proceedings of the National Academy of Sciences* **2015**, *112* (41), 12574-12579.
- [117] Sheehan, J. K.; Kirkham, S.; Howard, M.; Woodman, P.; Kutay, S.; Brazeau, C.; Buckley, J.; Thornton, D. J., Identification of molecular intermediates in the assembly pathway of the MUC5AC mucin. *Journal of Biological Chemistry* **2004**, *279* (15), 15698-15705.
- [118] Brayshaw, D. J.; Berry, M.; McMaster, T. J., Reducing a polymer to its subunits as an aid to molecular mapping. *Nanotechnology* **2004**, *15* (11), 1391.

- [119] Holmén, J. M.; Karlsson, N. G.; Abdullah, L. H.; Randell, S. H.; Sheehan, J. K.; Hansson, G. C.; Davis, C. W., Mucins and their O-Glycans from human bronchial epithelial cell cultures. *American Journal of Physiology-Lung Cellular and Molecular Physiology* **2004**, 287 (4), L824-L834.
- [120] Schattling, P.; Taipaleenmäki, E.; Zhang, Y.; Städler, B., A Polymer Chemistry Point of View on Mucoadhesion and Mucopenetration. *Macromolecular Bioscience* **2017**.
- [121] Olmsted, S. S.; Padgett, J. L.; Yudin, A. I.; Whaley, K. J.; Moench, T. R.; Cone, R. A., Diffusion of macromolecules and virus-like particles in human cervical mucus. *Biophysical journal* **2001**, 81 (4), 1930-1937.
- [122] Lieleg, O.; Ribbeck, K., Biological hydrogels as selective diffusion barriers. *Trends in cell biology* **2011**, 21 (9), 543-551.
- [123] Sauter, N. K.; Bednarski, M. D.; Wurzburg, B. A.; Hanson, J. E.; Whitesides, G. M.; Skehel, J. J.; Wiley, D. C., Hemagglutinins from two influenza virus variants bind to sialic acid derivatives with millimolar dissociation constants: a 500-MHz proton nuclear magnetic resonance study. *Biochemistry* **1989**, 28 (21), 8388-8396.
- [124] Mammen, M.; Dahmann, G.; Whitesides, G. M., Effective inhibitors of hemagglutination by influenza virus synthesized from polymers having active ester groups. Insight into mechanism of inhibition. *Journal of medicinal chemistry* **1995**, 38 (21), 4179-4190.
- [125] Kainthan, R. K.; Hester, S. R.; Levin, E.; Devine, D. V.; Brooks, D. E., In vitro biological evaluation of high molecular weight hyperbranched polyglycerols. *Biomaterials* **2007**, 28 (31), 4581-4590.
- [126] Kainthan, R. K.; Brooks, D. E., In vivo biological evaluation of high molecular weight hyperbranched polyglycerols. *Biomaterials* **2007**, 28 (32), 4779-4787.
- [127] Liu, H.-P.; Meng, X.; Yu, Q.; Tao, Y.-C.; Xu, F.; He, Y.; Yu, P.; Yang, Y., Synthesis of S-sialyl polymers as efficient polyvalent influenza inhibitors and capturers. *Journal of Carbohydrate Chemistry* **2018**, 37 (1), 18-29.
- [128] Tang, S.; Puryear, W. B.; Seifried, B. M.; Dong, X.; Runstadler, J. A.; Ribbeck, K.; Olsen, B. D., Antiviral Agents from Multivalent Presentation of Sialyl Oligosaccharides on Brush Polymers. *ACS Macro Letters* **2016**, 5 (3), 413-418.
- [129] Chen, X.; Lee, G. S.; Zettl, A.; Bertozzi, C. R., Biomimetic engineering of carbon nanotubes by using cell surface mucin mimics. *Angewandte Chemie International Edition* **2004**, 43 (45), 6111-6116.
- [130] Rabuka, D.; Parthasarathy, R.; Lee, G. S.; Chen, X.; Groves, J. T.; Bertozzi, C. R., Hierarchical assembly of model cell surfaces: synthesis of mucin mimetic polymers and their display on supported bilayers. *Journal of the American Chemical Society* **2007**, 129 (17), 5462-5471.
- [131] Cohen, M.; Senaati, H. P.; Fisher, C. J.; Huang, M. L.; Gagneux, P.; Godula, K., Synthetic Mucus Nanobarriers for Identification of Glycan-Dependent Primary Influenza A Infection Inhibitors. *ACS Central Science* **2016**, 2 (10), 710-714.
- [132] Truelove, S.; Zhu, H.; Lessler, J.; Riley, S.; Read, J. M.; Wang, S.; Kwok, K. O.; Guan, Y.; Jiang, C. Q.; Cummings, D. A., A comparison of hemagglutination inhibition and neutralization assays for characterizing immunity to seasonal influenza A. *Influenza and other respiratory viruses* **2016**, 10 (6), 518-524.
- [133] Hirst, G. K., The agglutination of red cells by allantoic fluid of chick embryos infected with influenza virus. *Science* **1941**, 94 (2427), 22-23.
- [134] McCLELLAND, L.; Hare, R., The adsorption of influenza virus by red cells and a new in vitro method of measuring antibodies for influenza virus. *Canadian Public Health Journal* **1941**, 32 (10), 530-538.

- [135] Spackman, E.; Sitaras, I., Hemagglutination Inhibition Assay. In *Animal Influenza Virus*, Springer: 2020; pp 11-28.
- [136] Trombetta, C.; Ulivieri, C.; Cox, R.; Remarque, E.; Centi, C.; Perini, D.; Piccini, G.; Rossi, S.; Marchi, S.; Montomoli, E., Impact of erythrocyte species on assays for influenza serology. *Journal of preventive medicine and hygiene* **2018**, *59* (1), E1.
- [137] Zacour, M.; Ward, B. J.; Brewer, A.; Tang, P.; Boivin, G.; Li, Y.; Warhuus, M.; McNeil, S. A.; LeBlanc, J. J.; Hachette, T. F., Standardization of hemagglutination inhibition assay for influenza serology allows for high reproducibility between laboratories. *Clinical and Vaccine Immunology* **2016**, *23* (3), 236-242.
- [138] Blixt, O.; Head, S.; Mondala, T.; Scanlan, C.; Huflejt, M. E.; Alvarez, R.; Bryan, M. C.; Fazio, F.; Calarese, D.; Stevens, J., Printed covalent glycan array for ligand profiling of diverse glycan binding proteins. *Proceedings of the National Academy of Sciences* **2004**, *101* (49), 17033-17038.
- [139] Liang, C.-H.; Wu, C.-Y., Glycan array: a powerful tool for glycomics studies. *Expert review of proteomics* **2009**, *6* (6), 631-645.
- [140] Peng, W.; de Vries, R. P.; Grant, O. C.; Thompson, A. J.; McBride, R.; Tsogtbaatar, B.; Lee, P. S.; Razi, N.; Wilson, I. A.; Woods, R. J., Recent H3N2 viruses have evolved specificity for extended, branched human-type receptors, conferring potential for increased avidity. *Cell host & microbe* **2017**, *21* (1), 23-34.
- [141] Huang, M. L.; Cohen, M.; Fisher, C. J.; Schooley, R. T.; Gagneux, P.; Godula, K., Determination of receptor specificities for whole influenza viruses using multivalent glycan arrays. *Chemical Communications* **2015**, *51* (25), 5326-5329.
- [142] Godula, K.; Rabuka, D.; Nam, K. T.; Bertozzi, C. R., Synthesis and Microcontact Printing of Dual End-Functionalized Mucin-like Glycopolymers for Microarray Applications. *Angewandte Chemie* **2009**, *121* (27), 5073-5076.
- [143] Petersen, R. L., Strategies using bio-layer interferometry biosensor technology for vaccine research and development. *Biosensors* **2017**, *7* (4), 49.
- [144] Apiyo, D. O., Biolayer Interferometry (Octet) for Label-free Biomolecular Interaction Sensing. In *Handbook of Surface Plasmon Resonance*, Royal Society of Chemistry: 2017; pp 356-397.
- [145] Fortébio <https://www.fortebio.com/applications/bli-technology> (accessed 23.10.2020)
- [146] Benton, D. J.; Martin, S. R.; Wharton, S. A.; McCauley, J. W., Biophysical measurement of the balance of influenza a hemagglutinin and neuraminidase activities. *Journal of Biological Chemistry* **2015**, *290* (10), 6516-6521.
- [147] Guo, H.; Rabouw, H.; Slomp, A.; Dai, M.; van der Vegt, F.; van Lent, J. W.; McBride, R.; Paulson, J. C.; de Groot, R. J.; van Kuppeveld, F. J., Kinetic analysis of the influenza A virus HA/NA balance reveals contribution of NA to virus-receptor binding and NA-dependent rolling on receptor-containing surfaces. *PLoS pathogens* **2018**, *14* (8), e1007233.
- [148] Dufrêne, Y. F.; Martínez-Martín, D.; Medalsy, I.; Alsteens, D.; Müller, D. J., Multiparametric imaging of biological systems by force-distance curve-based AFM. *Nature methods* **2013**, *10* (9), 847-854.
- [149] Rankl, C.; Kienberger, F.; Wildling, L.; Wruss, J.; Gruber, H. J.; Blaas, D.; Hinterdorfer, P., Multiple receptors involved in human rhinovirus attachment to live cells. *Proceedings of the National Academy of Sciences* **2008**, *105* (46), 17778-17783.

- [150] Sieben, C.; Kappel, C.; Zhu, R.; Wozniak, A.; Rankl, C.; Hinterdorfer, P.; Grubmüller, H.; Herrmann, A., Influenza virus binds its host cell using multiple dynamic interactions. *Proceedings of the National Academy of Sciences* **2012**, *109* (34), 13626-13631.
- [151] Alsteens, D.; Newton, R.; Schubert, R.; Martinez-Martin, D.; Delguste, M.; Roska, B.; Müller, D. J., Nanomechanical mapping of first binding steps of a virus to animal cells. *Nature nanotechnology* **2017**, *12* (2), 177.
- [152] Reiter-Scherer, V.; Cuellar-Camacho, J. L.; Bhatia, S.; Haag, R.; Herrmann, A.; Lauster, D.; Rabe, J. P., Force spectroscopy shows dynamic binding of influenza hemagglutinin and neuraminidase to sialic acid. *Biophysical journal* **2019**, *116* (6), 1037-1048.
- [153] Cuellar-Camacho, J. L.; Bhatia, S.; Reiter-Scherer, V.; Lauster, D.; Liese, S.; Rabe, J. r. P.; Herrmann, A.; Haag, R., Quantification of Multivalent Interactions between Sialic Acid and Influenza A Virus Spike Proteins by Single-Molecule Force Spectroscopy. *Journal of the American Chemical Society* **2020**, *142* (28), 12181-12192.
- [154] Ambrose, E., A surface contact microscope for the study of cell movements. *Nature* **1956**, *178* (4543), 1194-1194.
- [155] Jung, H.; Robison, A. D.; Cremer, P. S., Multivalent ligand–receptor binding on supported lipid bilayers. *Journal of Structural Biology* **2009**, *168* (1), 90-94.
- [156] Diaz, A. J.; Albertorio, F.; Daniel, S.; Cremer, P. S., Double Cushions Preserve Transmembrane Protein Mobility in Supported Bilayer Systems. *Langmuir* **2008**, *24* (13), 6820-6826.
- [157] Albertorio, F.; Diaz, A. J.; Yang, T.; Chapa, V. A.; Kataoka, S.; Castellana, E. T.; Cremer, P. S., Fluid and Air-Stable Lipopolymer Membranes for Biosensor Applications. *Langmuir* **2005**, *21* (16), 7476-7482.
- [158] Goronzy, I. N.; Rawle, R. J.; Boxer, S. G.; Kasson, P. M., Cholesterol enhances influenza binding avidity by controlling nanoscale receptor clustering. *Chemical Science* **2018**, *9* (8), 2340-2347.
- [159] Wahlsten, O.; Gunnarsson, A.; Simonsson Nyström, L.; Pace, H.; Geschwindner, S.; Hook, F., Equilibrium-fluctuation analysis for interaction studies between natural ligands and single g protein-coupled receptors in native lipid vesicles. *Langmuir* **2015**, *31* (39), 10774-10780.
- [160] Bally, M.; Gunnarsson, A.; Svensson, L.; Larson, G.; Zhdanov, V. P.; Höök, F., Interaction of Single Viruslike Particles with Vesicles Containing Glycosphingolipids. *Physical Review Letters* **2011**, *107* (18), 188103.
- [161] Lee, D. W.; Hsu, H.-L.; Bacon, K. B.; Daniel, S., Image Restoration and Analysis of Influenza Virions Binding to Membrane Receptors Reveal Adhesion-Strengthening Kinetics. *PLOS ONE* **2016**, *11* (10), e0163437.
- [162] Block, S.; Zhdanov, V. P.; Höök, F., Quantification of Multivalent Interactions by Tracking Single Biological Nanoparticle Mobility on a Lipid Membrane. *Nano Letters* **2016**, *16* (7), 4382-4390.
- [163] Vonnemann, J.; Liese, S.; Kuehne, C.; Ludwig, K.; Dervedde, J.; Böttcher, C.; Netz, R. R.; Haag, R., Size Dependence of Steric Shielding and Multivalency Effects for Globular Binding Inhibitors. *Journal of the American Chemical Society* **2015**, *137* (7), 2572-2579.
- [164] Calderón, M.; Quadir, M. A.; Sharma, S. K.; Haag, R., Dendritic polyglycerols for biomedical applications. *Advanced materials* **2010**, *22* (2), 190-218.
- [165] Müller, M.; Lauster, D.; Wildenauer, H. H. K.; Herrmann, A.; Block, S., Mobility-Based Quantification of Multivalent Virus-Receptor Interactions: New Insights Into Influenza A Virus Binding Mode. *Nano Letters* **2019**, *19* (3), 1875-1882.



- [166.] Wallert, M.; Nie, C.; Anilkumar, P.; Abbina, S.; Bhatia, S.; Ludwig, K.; Kizhakkedathu, J. N.; Haag, R.; Block, S., Mucin-Inspired, High Molecular Weight Virus Binding Inhibitors Show Biphasic Binding Behavior to Influenza A Viruses. *Small n/a* (n/a), 2004635.
- [167] Anilkumar, P.; Lawson, T. B.; Abbina, S.; Mäkelä, J. T.; Sabatelle, R. C.; Takeuchi, L. E.; Snyder, B. D.; Grinstaff, M. W.; Kizhakkedathu, J. N., Mega macromolecules as single molecule lubricants for hard and soft surfaces. *Nature Communications* **2020**, *11* (1), 1-9.

## 8 List of abbreviations

AFM	atomic force microscopy
ATRP	atom transfer radical polymerization
BLI	biolayer interferometry
DTT	dithiothreitol
FRAP	fluorescent recovery after photobleaching
HA	hemagglutinin
HAI	hemagglutination inhibition
hPG	hyperbranched polyglycerol
HSV	herpes simplex virus
IAV	influenza A virus
LPG	linear polyglycerol
MALDI -TOF	matrix-assisted laser desorption ionization time-of-flight
NA	neuraminidase
NCA	N-carboxyanhydride
NMP	N-Methyl-2-pyrrolidon
PAMAM	polyamidoamine
PEG	polyethylene glycol
PEI	polyethyleneimine
POPC	phosphatidylcholine
RAFT	reversible addition-fragmentation chain-transfer
RSV	respiratory syncytial virus
SLB	supported lipid bilayer
SWNTs	single-walled carbon nanotubes
THF	tetrahydrofuran
TIRF	total internal reflection fluorescence
VLPs	virus like particles
VSV	vesicular stomatitis virus

## 9 List of publications, manuscripts and conferences

### Publications and manuscripts

Matthias Wallert, Johann Plaschke, Mathias Dimde, Stephan Block, Rainer Haag, “Automated solvent-free polymerization of hyperbranched polyglycerol with tailored molecular weight by online torque detection,” *submitted*

Chuanxiong Nie, Marlena Stadtmüller, Badri Parshad, Matthias Wallert, Vahid Ahmadi, Yannic Kerkhoff, Sumati Bhatia, Stephan Block, Chong Cheng, Thorsten Wolff, Rainer Haag, “Heteromultivalent topology-matched nanostructures as potent and broad-spectrum influenza A virus inhibitors,” *Science Advances*, accepted 19.10.2020

Sumati Bhatia, Malte Hilsch, Jose Luis Cuellar-Camancho, Kai Ludwig, Chuanxiong Nie, Badri Parshad, Matthias Wallert, Stephan Block, Daniel Lauster, Christoph Böttcher, Andreas Herrmann, Rainer Haag, “Adaptive Flexible Sialylated Nanogels as Highly Potent Influenza A Virus Inhibitors,” *Angewandte Chemie International Edition* **2020**, 59, 1-8

Matthias Wallert, Chuanxiong Nie, Parambath Anilkumar, Srinivas Abbina, Sumati Bhatia, Kai Ludwig, Jayachandran N. Kizhakkedathu, Rainer Haag, Stephan Block, “Mucin-inspired, High Molecular Weight Virus Binding Inhibitors Show Biphasic Binding Behavior to Influenza A Viruses,” *Small* **2020**, <https://doi.org/10.1002/sml.202004635>

Matthias Müller, Daniel Lauster, Helen H. K. Wildenauer, Andreas Herrmann, Stephan Block, “Mobility-Based Quantification of Multivalent Virus-Receptor Interactions: New Insights Into Influenza A Virus Binding Mode,” *Nano Letters* **2019**, 19 (3), 1875-1882.

### Oral presentations

Matthias Müller, Parambath Anilkumar, Jayachandran N. Kizhakkedathu, Rainer Haag, Stephan Block, “Multivalent, mucin-inspired virus binding inhibitor characterized by total internal reflection fluorescence (TIRF) microscopy,” 1st International Symposium on Glycovirolgy – Schöntal 2018

## **Poster presentations**

Matthias Müller, Parambath Anilkumar, Jayachandran Kizhakkedathu, Rainer Haag, Stephan Block, “Mucin-inspired broad range virus binding inhibitor based on multivalent high molecular weight polyglycerol,” *14<sup>th</sup> International Workshop on Carcinoma-associated Mucins “Mucins in Health and Diseases”* – Cambridge, July 2017

Matthias Müller, Anilkumar Parambath, Jayachandran Kizhakkedathu, Rainer Haag, Stephan Block, “Multivalent, mucin-inspired virus binding inhibitor based on high molecular weight hyperbranched polyglycerol,” *4<sup>th</sup> International Symposium SFB 765 “Multivalent Interaction of Pathogens with Biological Surfaces”* - Berlin, October 2017

Matthias Müller, Daniel Lauster, Andreas Herrmann, Stephan Block, „Total internal reflection fluorescence (TIRF) microscopy for binding studies of viruses and their inhibition by binding inhibitors,” *Summer School Advanced Optical Microscopy* - Berlin, October 2018

Matthias Müller, Parambath Anilkumar, Jayachandran Kizhakkedathu, Rainer Haag, Stephan Block, “Mucin-inspired broad range virus binding inhibitor based on multivalent high molecular weight hyperbranched polyglycerol,” *13<sup>th</sup> international Symposium on Frontiers in Biomedical Polymers* - Puerto de la Cruz, March 2019

Matthias Wallert, Parambath Anilkumar, Jayachandran Kizhakkedathu, Rainer Haag, Stephan Block, “Mucin-inspired broad range virus binding inhibitor based on multivalent high molecular weight hyperbranched polyglycerol,” *16<sup>th</sup> Bayreuth Polymer Symposium* - Bayreuth, September 2019

Matthias Wallert, Mathias Dimde, Stephan Block, Rainer Haag, “Automatized solvent-free hyperbranched polyglycerol polymerization tailor-made over torque detection,” *15<sup>th</sup> European Detergent Conference (GDCh)* - Berlin, October 2019

## **10 Curriculum vitae**

For reasons of data protection, the curriculum vitae is not included in the online version.

## **Declaration of honesty**

Hereby I declare and confirm that this PhD thesis is entirely the result of my own work and that no other sources than those cited have been used. All annotations, which have been used from published or unpublished sources, are identified as such. The shown illustrations have been created by me, or have been marked with the corresponding references.

---

Matthias Wallert

January 2021